

# Variation of Multiplicity and Transverse Energy Flow with $W^2$ and $Q^2$ in Deep Inelastic Scattering at HERA

Thesis for the degree of Doctor of Philosophy in Physics  
by

Håkan Lohmander



Elementary Particle Physics  
Department of Physics, University of Lund  
Lund 1995

ISBN 91-628-1581-4  
LUNFD6/(NFFL-1703)1995

# Variation of Multiplicity and Transverse Energy Flow with $W^2$ and $Q^2$ in Deep Inelastic Scattering at HERA

By due permission of the faculty of mathematics and natural science at the University of  
Lund to be publicly discussed at the lecture hall B at the department of Physics,  
May 12 1995, at 10.15 a.m. for the degree of Doctor of Philosophy

by

Håkan Lohmander

Department of Physics, University of Lund, Sölvegatan 14, S-223 62 Lund, Sweden

This thesis is partly based on the following articles, included as Appendix F and G

- I* The H1 Forward Muon Spectrometer,  
Nucl. Instr. and Meth. A 340 (1994) 304-308
- II* Selecting forward tracks in the H1 detector,  
H1 Collaboration Internal Report, H1-03/94-347

## Abstract

Charged particle and transverse energy flow for deep inelastic  $ep$  scattering at HERA have been investigated in the hadronic center of mass system as a function of pseudorapidity  $\eta^*$  in different  $W^2$  and  $Q^2$  intervals. In addition, the mean charged particle multiplicity  $\langle n_{ch} \rangle$  and the mean transverse energy  $\langle E_T^* \rangle$  as a function of  $W^2$  and  $Q^2$  have been studied. The measurements were made in the kinematic region  $85 < W < 230 \text{ GeV}$  and  $10 < Q^2 < 7000 \text{ GeV}^2$

The  $\langle n_{ch} \rangle$  was found to increase with increasing  $W^2$  at fixed  $Q^2$  but did not show any significant dependence on  $Q^2$  at fixed  $W^2$ . The best description of the mean charged multiplicity is given by  $\langle n_{ch} \rangle = a + b \cdot \ln(W^2/\text{GeV}^2)$  with  $a = -1.38 \pm 0.07$  and  $b = 0.93 \pm 0.05$ .

The  $\langle E_T^* \rangle$  increased both with increasing  $W^2$  at fixed  $Q^2$  and with increasing  $Q^2$  at fixed  $W^2$ . The mean transverse energy is described by  $\langle E_T^* \rangle = a + b \cdot \ln(W^2/\text{GeV}^2) + c \cdot \ln(Q^2/\text{GeV}^2) \text{ GeV}$  with  $a = -5.93 \pm 0.07$ ,  $b = 1.28 \pm 0.06$  and  $c = 0.69 \pm 0.02$ .

Different QCD models have been compared with data. Only the Color Dipole Model, as implemented in the Monte Carlo program Ariadne, describes the data satisfactorily.

## Acknowledgements

An experiment as large as H1 can only be successful through the effort of a large number of people. Therefore I would like to thank all the members of the H1 collaboration and particular I would like to thank the following people.

My supervisor Leif Jönsson for his patient support and advice, and for giving me the chance to do this work. Michael Kuhlen for telling me all worth knowing about corrections and error calculations. Stephen Burke for sharing his knowledge of the forward tracker and for his suggestions on selecting forward tracks. Vincent Hedberg for helping me in the beginning of this work. Peter Lanius for his advises concerning track reconstruction and for all the nice discussions we have had. Frank Botterweck for spending so much time on figuring out the optimum way of selecting the central tracks.

I would also like to thank Bo Andersson for generously spending his time explaining the theory behind the different Monte Carlo models.

Also, special thanks to my fellow PhD students, Morten and Christian, for making life easier at H1 and for all the laughs we have had.

My girlfriend, Kerstin, for her support and encouragement and for just being the lovely person she is.

Last but not least, my family and particularly my father, Bengt, for spending so much time discussing this work with me and for having faith in me at times when I didn't have it my self.

*To my parents,  
Bengt and Kerstin*

# Contents

<b>1</b>	<b>Introduction</b>	<b>1</b>
1.1	Elementary Particles and Fundamental Interactions . . . . .	1
1.2	Background and Aims of the Study . . . . .	2
<b>2</b>	<b>Theory</b>	<b>5</b>
2.1	Kinematics . . . . .	5
2.2	Deep Inelastic Scattering . . . . .	7
2.2.1	The Quark Parton Model . . . . .	9
2.2.2	Matrix Elements . . . . .	9
2.2.3	QCD Parton Cascades . . . . .	9
2.2.3.1	Parton Showers in the Leading Logarithmic Approximation	10
2.2.3.2	The Color Dipole Model . . . . .	11
2.2.4	Fragmentation . . . . .	13
2.2.4.1	String Fragmentation . . . . .	14
2.2.4.2	Proton Remnant Fragmentation . . . . .	15
<b>3</b>	<b>Monte Carlo Generators</b>	<b>17</b>
3.1	Generators in General . . . . .	17
3.2	Lepto . . . . .	17
3.2.1	No QCD effects . . . . .	18
3.2.2	Parton Showers . . . . .	18
3.2.3	Matrix Elements with Parton Showers . . . . .	18
3.3	Ariadne . . . . .	20
<b>4</b>	<b>The HERA Collider and the H1 Detector</b>	<b>23</b>
4.1	The HERA ep Storage Ring . . . . .	23
4.2	The H1 Detector . . . . .	25
4.2.1	The Tracking System . . . . .	27
4.2.1.1	The H1 Main Magnet . . . . .	27
4.2.1.2	Central Tracking System . . . . .	27
4.2.1.3	The Forward Tracking System . . . . .	30
4.2.1.4	The Proportional Chambers . . . . .	31
4.2.2	The Calorimeter System . . . . .	32
4.2.2.1	The Liquid Argon Calorimeter . . . . .	32
4.2.2.2	The Plug Calorimeter . . . . .	33
4.2.2.3	The Backward Electromagnetic Calorimeter . . . . .	33
4.2.2.4	The Tail Catcher . . . . .	34

4.2.3	The Muon System . . . . .	35
4.2.4	The Scintillator Counters . . . . .	36
4.2.5	The Trigger System . . . . .	37
<b>5</b>	<b>The Data Analysis</b>	<b>39</b>
5.1	Detector Simulation and Event Reconstruction . . . . .	39
5.2	Reconstruction of the Event Variables . . . . .	40
5.3	Event Selection . . . . .	41
5.4	Background Events . . . . .	43
5.5	Selection of Tracks and Clusters . . . . .	45
5.6	Binning of the Events . . . . .	47
5.7	Corrections . . . . .	48
5.8	Systematic errors . . . . .	50
<b>6</b>	<b>Results</b>	<b>53</b>
6.1	Energy Flow . . . . .	53
6.1.1	The Transverse Energy Flow . . . . .	53
6.1.2	Mean Transverse Energy . . . . .	58
6.2	Charged Multiplicity . . . . .	62
6.2.1	Charged Particle Flow . . . . .	62
6.2.2	Mean Charged Particle Multiplicity . . . . .	67
<b>7</b>	<b>Conclusions</b>	<b>71</b>
	<b>Bibliography</b>	<b>74</b>
	<b>List of figures</b>	<b>75</b>
	<b>List of tables</b>	<b>77</b>
<b>A</b>	<b>List of data values</b>	<b>79</b>
<b>B</b>	<b>Generators</b>	<b>85</b>
<b>C</b>	<b>Formulae</b>	<b>87</b>
<b>D</b>	<b>Glossary</b>	<b>89</b>
<b>E</b>	<b>The H1 collaboration</b>	<b>91</b>
<b>F</b>	<b>The H1 Forward Muon Spectrometer</b>	<b>95</b>
<b>G</b>	<b>Selecting Forward Tracks in the H1-Detector</b>	<b>97</b>

# Chapter 1

## Introduction

### 1.1 Elementary Particles and Fundamental Interactions

According to our present understanding, the basic building blocks of nature are spin 1/2 point-like particles of two types, quarks and leptons. There are six different types (or flavors) of quarks and six different types of leptons. These are grouped into three families, see table 1.1.

The elementary particles interact via the fundamental forces. These are the electromagnetic and the so called strong and weak forces <sup>1</sup>. Interactions between particles are mediated by the exchange of vector bosons, which are the carriers of the forces.

The mediator of the electromagnetic force, described by the Quantum Electrodynamics (QED), is the photon, while the mediators of the weak interaction are the vector bosons  $W^+$ ,  $W^-$  and  $Z^0$ . The theory describing strong interactions is known as Quantum Chromo Dynamics (QCD), chromo because the charge in strong interaction is called color. The mediators of the strong force are the gluons which couple both to the quarks and, in contrast to photons, also to other gluons.

Fermions	Family						Interaction		
	1:st Type	Mass	2:nd Type	Mass	3:rd Type	Mass	strong	electro- magnetic	weak
Quarks	$u$	0.31	$c$	1.65	$t$	176	x	x	x
	$d$	0.31	$s$	0.48	$b$	4.5	x	x	x
Leptons	$e$	$5 \cdot 10^{-4}$	$\mu$	0.11	$\tau$	1.77		x	x
	$\nu_e$	$< 5 \cdot 10^{-9}$	$\mu_\nu$	$< 10^{-4}$	$\nu_\tau$	$< 2 \cdot 10^{-2}$			x

Table 1.1: *The elementary particles, their masses and the type of interaction that affects them. All masses are in the unit  $GeV/c^2$ .*

The partons (quarks and gluons) appear to be permanently confined within the hadrons, in the sense that free partons have never been observed. Instead they appear in groups

---

<sup>1</sup>The gravitational force is also a fundamental force, but on the scale of elementary particles interactions it can safely be neglected.

such as mesons, consisting of a quark and an antiquark ( $q\bar{q}$ ), or baryons, which consist of three quarks ( $qqq$  or  $\bar{q}\bar{q}\bar{q}$ ). Mesons and baryons are collectively called hadrons.

The strong force is mainly responsible for the effects investigated in this study.

## 1.2 Background and Aims of the Study

The dependence of the amount of hadrons produced (the hadron multiplicity) on  $W^2$ , the hadronic center of mass energy, has been measured both in electron-nucleon [1] and muon-proton [2] scattering experiments. In both types of experiments the mean charged hadron multiplicity,  $\langle n_{ch} \rangle$ , was observed to grow logarithmically with  $W^2$ . The logarithmic dependence on  $W^2$  is an experimental fact and has not been derived from theoretical calculations. The reason for this is that such a calculation would mean calculating all possible combinations of hadrons in the final state for all possible energies, which is not feasible. A particular Monte Carlo model where the amount of particles produced increases with increasing  $W^2$  is the Lund String Model [8]. In this model the allowed kinematic region for production of particles increases as  $\ln W^2$ .

The dependence of the average hadron multiplicity on  $Q^2$ , the square of the momentum transfer between the lepton and the proton, at fixed  $W^2$  has also been investigated [1], [2]. However, the results are not as conclusive as in the case of the  $W^2$  dependence.

A fixed target electron-proton experiment at the Cornell university [1] was first to investigate the average hadron multiplicity dependence on  $Q^2$ . The result showed that the mean charged hadron multiplicity was independent of  $Q^2$  but increased with  $W^2$ . In 1985 the EMC  $\mu p$  fixed target experiment [2] reported a weak but statistically significant growth of the average multiplicity of charged hadrons with  $Q^2$  and, like the Cornell group, they also observed that the average multiplicity rose with increasing  $W^2$ . Both [1] and [2] made a fit to their corrected data points with a function of the form

$$\langle n_{ch} \rangle = a + b \ln(W^2/W_0^2) + c \ln(Q^2/Q_0^2) \quad (1.1)$$

where  $W_0^2 = Q_0^2 = 1 \text{ GeV}^2$ . The results are shown in table 1.2.

The multiplicity dependence on  $Q^2$  and  $W^2$  has also been investigated in  $\nu p$  and  $\bar{\nu} p$  charged current experiments like FNAL [3] and WA21 [4]. In 1982 the neutrino experiment at FNAL reported that the average multiplicity increased with  $W^2$  and in 1989 WA21 reported an average multiplicity that increased both with  $W^2$  and  $Q^2$ . The results from [3] and [4] are also shown in table 1.2.

To conclude: All experiments report a mean multiplicity that increases as  $\ln W^2$  at fixed  $Q^2$ . Two experiments report a mean multiplicity that is independent of  $Q^2$ , and two that it increases with  $Q^2$ . Thus we have a somewhat unclear situation regarding the multiplicity dependence on  $Q^2$  at low energies ( $W < 20 \text{ GeV}$ ). Therefore, it is of interest to study the mean multiplicity at higher energies in order to see if there is a clear  $Q^2$  dependence at fixed  $W^2$  or not. This can be done at the electron-proton collider HERA situated at DESY. HERA is designed to collide 30 GeV electrons with 820 GeV protons, resulting in a maximum  $W$  of 314 GeV and  $Q^2$  up to about 90000 GeV<sup>2</sup>. The

---

<sup>2</sup>The investigation is performed at fixed  $W^2$  since  $Q^2$  and  $W^2$  are related through  $W^2 = m_p^2 + Q^2(\frac{1-x}{x})$  ( $x$  is the fraction of the proton's momentum carried by the struck quark and  $m_p^2$  the proton mass squared) and an explicit dependence on  $W^2$  is to be avoided. Conversely, to avoid a dependence on  $Q^2$  when measuring the  $W^2$  dependence,  $Q^2$  has to be kept fixed.

	Range covered		Fitted parameters		
	W [GeV]	Q <sup>2</sup> [GeV <sup>2</sup> ]	a	b	c
Cornell	1.7 – 3.7	1.4 – 8	-0.37 ± 0.07	1.55 ± 0.04	-
EMC	4 – 20	4 – 100	-0.30 ± 0.16	1.22 ± 0.03	0.22 ± 0.04 ± 0.06
FNAL	2 – 10	1 – 30	-0.44 ± 0.13	1.48 ± 0.06	-
WA21	2 – 14	1 – 50	0.46 ± 0.05	1.21 ± 0.02	0.10 ± 0.01

Table 1.2: Summary of the published results from different experiments. Each experiment fitted a function of the form  $\langle n_{ch} \rangle = a + b \ln(W^2/W_0^2) + c \ln(Q^2/Q_0^2)$ ,  $W_0^2 = Q_0^2 = 1 \text{ GeV}^2$ , to their corrected data point except the FNAL experiment which fitted the function  $\langle n_{ch} \rangle = a + b \ln(W^2/W_0^2)$ .

maximum reachable  $W^2$  at HERA is more than 100 times higher than at previous fixed target experiments. Figure 1.1 shows the kinematic region in  $x$  and  $Q^2$  covered by fixed target experiments and by HERA. As can be seen, with the HERA collider a new domain in energy is available.

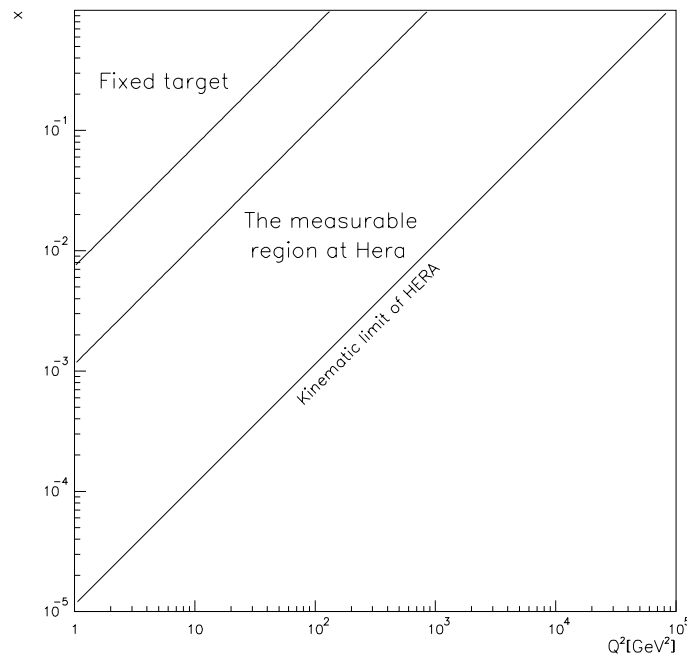


Figure 1.1: The kinematic region in  $x$  and  $Q^2$  covered by fixed target experiments and by HERA. The HERA collider gives access to higher  $Q^2$  and  $W$  values as well as lower  $x$  values.

The origin of a possible  $Q^2$  dependence is at the moment not completely clear, although it probably stems from QCD effects, i.e hard and soft gluon emission. Another suggestion is that the  $Q^2$  dependence could be a consequence of a  $Q^2$  dependence in the fragmentation functions<sup>3</sup>. In  $\nu p$  and  $\bar{\nu} p$  collisions the observed dependence is not reproduced by the

<sup>3</sup>The fragmentation functions describe how the partons are transformed into hadrons

Lund model including first order QCD corrections [4], which may suggest that soft gluon emission is also needed.

The QCD effects can be taken into account by including the exact first order matrix elements, to simulate the hard radiation, together with a leading log QCD (LLQCD) shower formalism to simulate the soft radiation, or by simulating all the QCD radiation using the LLQCD formalism. Both these approaches have been implemented in the Monte Carlo program Lepto [9]. In another Monte Carlo program, Ariadne [10], the Color Dipole Model [11] (CDM) formalism is used to describe the parton shower.

Ariadne and Lepto both use the same generator for the electro-weak process and the same model for the hadronization (Lund string fragmentation as implemented in Jetset [12]) but they differ in the modeling of the QCD cascades. The LLQCD and the CDM parton shower models give rise to different predictions of the mean charged particle multiplicity as a function of  $Q^2$  at fixed  $W$  intervals, as well as the charged particles flow, i.e. number of charged particles as a function of pseudorapidity. However, the behavior of the mean multiplicity as a function of  $W^2$  at fixed  $Q^2$  is rather similar.

Ariadne and Lepto also predict different behaviors of the mean transverse energy in the hadronic center of mass system,  $\langle E_t^* \rangle$ , as a function of  $Q^2$  at fixed  $W$ . The transverse energy is the energy perpendicular to the beam axis. The  $\langle E_t^* \rangle$  as a function of  $W^2$  at fixed  $Q^2$  is similar for both Ariadne and Lepto.

The differences in the cascade models are manifested in such a way that the mean charged particle multiplicity is less dependent on  $Q^2$  in the Ariadne scheme than in the Lepto scheme. The mean transverse energy increases with  $Q^2$  in both Lepto and Ariadne although they have different absolute values <sup>4</sup>.

It is therefore of interest to compare Ariadne and Lepto with the results obtained in the H1 experiment to decide which QCD cascade model best reproduces the data.

The mean charged particle multiplicity and the mean transverse energy are measured by two independent detector systems. The mean charged particle multiplicity is determined using the information from the tracking system and the mean transverse energy is measured using the calorimeter information.

To summarize: The aim of this study is to give empirical results for the mean charged multiplicity dependence on  $Q^2$  and  $W^2$  at higher values of  $Q^2$  and  $W^2$ , thus extending the previous investigated kinematical region. Empirical results will also be given on the mean transverse energy dependence on  $Q^2$  and  $W^2$ . Furthermore, both the charged particle flow and the transverse energy flow as a function of pseudorapidity  $\eta^*$ , in different  $Q^2$  and  $W$  intervals, are to be investigated and empirical results obtained. Finally the Monte Carlo programs Ariadne and Lepto, representing two different theoretical models, are to be compared with the data collected with the H1 detector.

---

<sup>4</sup>The comparison above between Ariadne and Lepto is valid if the parameters in Lepto which control the parton cascade are at their default values. The version and the parameter settings of the generators used in this study are listed in appendix B.

# Chapter 2

## Theory

In this chapter the basic formulae needed to describe deep inelastic scattering processes are presented, notations are specified and the theory relevant for the study is described.

### 2.1 Kinematics

In deep inelastic  $ep$  scattering (DIS) events the electron interacts with the proton via the exchange of a virtual photon ( $\gamma^*$ )<sup>1</sup> as shown in figure 2.1 (which is drawn in the laboratory system<sup>2</sup>). The incoming proton defines  $\theta = 0^\circ$  and the angle of the scattered electron  $\theta_e$  is measured with respect to the incoming electron.

The kinematic variables used to describe a DIS event are:  $Q^2$ ,  $W^2$  and the scaling variables  $y$  and  $x$ .  $Q^2$  is the square of the momentum transfer between the electron and the proton.  $y$  is the fraction of the incident electron energy transferred by the virtual photon (actually this interpretation of  $y$  is exact only for fixed target experiments where the proton is at rest). In the quark parton model,  $x$  is the fraction of the proton's momentum carried by the struck quark.  $W^2$  is the total invariant mass squared of the hadronic system. This is the energy available to form particles.

In an experiment the event variables can be calculated either by measuring the energy and the angle of the scattered electron or by measuring the energy and momentum of the final-state hadrons.

There is a redundancy among the event variables, meaning that only two of them are independent, i.e. from any two variables the others can be calculated. For example two such independent variables are  $Q^2$  and  $W^2$ . This is in contrast to  $e^+e^-$  annihilation where  $Q^2 = W^2 = s$ ,  $s$  is the total invariant mass squared.

Below are the definitions of the kinematic variables  $Q^2$ ,  $y$ ,  $x$ ,  $W^2$ . In the case of  $Q^2$  and  $y$ , the expression for their calculation using the incoming and the scattered electron

---

<sup>1</sup>In rare cases the exchanged boson is a  $Z^0$  or  $W^\pm$ . In this study only neutral current events (i.e. the exchanged boson is  $\gamma$  or  $Z^0$ ) will be considered. As the probability of a  $Z^0$  interaction is very small at the momentum transfer squared  $Q^2$  considered in this study, from now on all discussions will be performed as if the electron interacts with the proton via a virtual photon.

<sup>2</sup>Throughout this paper the *laboratory* system is a right-handed Cartesian coordinate system with its origin in the interaction point ( $x = 0$ ,  $y = 0$ ,  $z = 0$ ). The  $z$ -axis points along the beam line in the flight direction of the proton which defines the forward direction ( $+z$ ). The  $y$ -axis points upward. Sometimes the polar coordinates are used instead. The  $x - y$  plane is then referred to as the  $r - \phi$  plan, and  $\theta$  denotes the polar angle with respect to the  $z$ -axis. Thus the  $x$ -axis and the  $y$ -axis correspond to an angle  $\phi = 0^\circ$  and  $\phi = 90^\circ$  respectively.

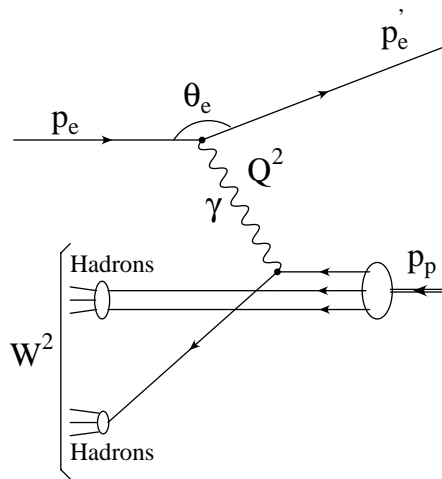


Figure 2.1: A schematic view of the deep inelastic scattering process drawn in the laboratory system. The electron, entering from the left, interacts via a virtual photon with a quark inside the proton. The quark is knocked out of the proton, which shatters. The forces acting between the proton remnant and the knocked out quark result in the production of hadrons.  $p_e$ ,  $p'_e$  and  $p_p$  are the four-vectors of the incoming electron, the scattered electron and the incoming proton respectively.  $\theta_e$  is the scattering angle of the electron.

is also given. The notations are the same as in figure 2.1. The approximations made are to neglect the masses of the electron and the proton which is a good approximation at the high energies HERA operates at. In appendix C the equations are derived in more detail.

$$Q^2 \equiv -q^2 = -(p_e - p'_e)^2 \approx 4E_e E'_e \cos^2(\theta_e/2) \quad (2.1)$$

$$y \equiv \frac{p_p \cdot q}{p_p \cdot p_e} \approx \frac{E_e - E'_e \sin^2(\theta_e/2)}{E_e} \quad (2.2)$$

$$x \equiv \frac{Q^2}{2p_p \cdot q} \approx \frac{Q^2}{4yE_e E_p} \quad (2.3)$$

$$W^2 \equiv (p_p + q)^2 \approx Q^2 \left( \frac{1-x}{x} \right) \quad (2.4)$$

$Q^2$ ,  $x$  and  $y$  are related through the equation  $Q^2 \approx xys$ , where  $s \equiv (p_e + p_p)^2$ .

The kinematic variables can also be calculated from the hadronic system using the Jaquet-Blondel (*JB*) method [5] according to:

$$y_{JB} = \frac{\sum_i (E_i - p_{xi})}{2E_e} \quad (2.5)$$

$$Q_{JB}^2 = \frac{(\sum_i p_{xi})^2 + (\sum_i p_{yi})^2}{1 - y_{JB}} \quad (2.6)$$

where the sum runs over all observed final state particles.

The double angle (*da*) method [6] uses the information from both the scattered electron and the hadronic system. The expression for  $y$  in this scheme is:

$$y_{da} = \frac{\sin\theta(1 - \cos\gamma)}{\sin\gamma + \sin\theta - \sin(\theta + \gamma)} \quad (2.7)$$

where  $\gamma$  is obtained from the relation:

$$\cos\gamma = \frac{Q_{JB}^2(1 - y_{JB}) - 4E_e^2 y_{JB}^2}{Q_{JB}^2(1 - y_{JB}) + 4E_e^2 y_{JB}^2} \quad (2.8)$$

The accuracy of the reconstruction of the kinematic variables by the various methods depends on where in the kinematic  $(x, Q^2)$  plane the event occurs.

Theoretical calculations are preferably performed (in order to simplify them) in the hadronic center of mass system<sup>3</sup> (*cms*) which is the rest frame of the interacting photon and the proton, see figure 2.2. In order to be able to compare the results of the theoretical calculations with the experimental results, the physics studies have also to be performed in the hadronic *cms*. Variables calculated in the hadronic *cms* are marked with an extra star, in order to distinguish them from variables calculated in the Lab frame. For example,  $\eta^*$  is the pseudorapidity in the hadronic *cms*. Note that the  $\gamma^*$  denotes the exchanged virtual photon and not a photon in the hadronic *cms*.

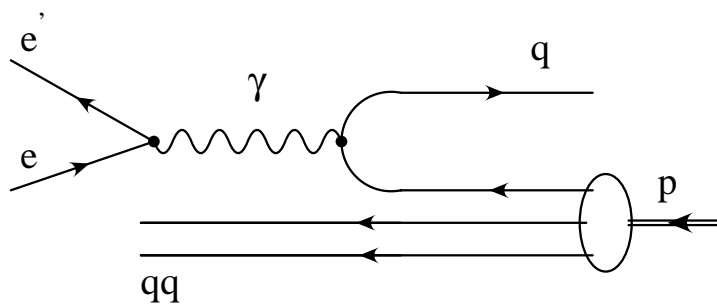


Figure 2.2: The scattering process according to the quark parton model shown in the hadronic *cms*. The incoming valence quark scatters backward on the photon. The proton remnants continue in the forward direction.

## 2.2 Deep Inelastic Scattering

This section starts with a brief description of deep inelastic scattering processes as they are usually viewed. Different models, based on perturbative QCD, describing the partonic final state will also be briefly discussed together with models for the hadronization process.

According to theory, the deep inelastic scattering processes are divided into different subprocesses or steps (see figure 2.3) which are treated as being essentially independent

<sup>3</sup>In consistency with the definition of the lab system, the forward direction (positive  $z$ -direction) in the *hadronic center of mass system* is defined as the direction of the incoming proton. The backward direction is the direction of the exchanged photon. The hadronic *cms* is sometimes called the  $\gamma p$  system as it is the rest frame of the proton and the virtual photon.

of each other. The hard subprocess step, in which the virtual photon interacts with a parton in the proton, is the step which describes the basic process. The struck parton may radiate new partons both "before" and/or "after" the hard subprocess<sup>4</sup>. When the partonic radiation step is finished the so called partonic final state has been reached. The partons are then transformed into hadrons via the hadronization process. Most of these produced hadrons are unstable and subsequently decay into stable observable ones<sup>5</sup>. This is the last step in the event generation sequence, i.e. when the so called hadronic final state has been produced.

The above description of the different steps is valid assuming that during the short time interval in which the parton and the virtual photon interact, interactions between the partons in the proton can be neglected. Further the bremsstrahlung process is expected to happen in a very short time compared to the subsequent hadronization process and therefore this latter process is expected to have no effect on the photon-parton interaction.

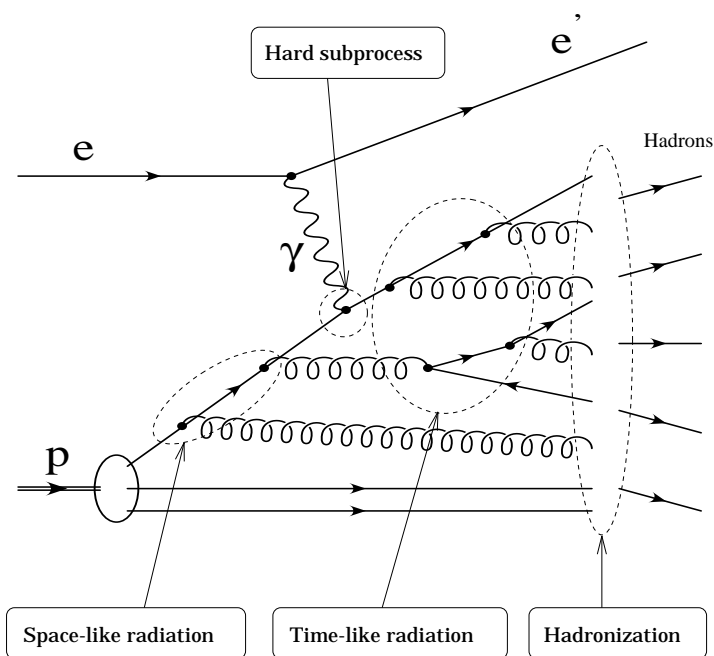


Figure 2.3: The different subprocesses in a DIS event. The 'input' to the hadronization process is the so called partonic final state while the 'output' is the hadronic final state.

The cross section (or probability) for a process is proportional to the so called structure functions, i.e.  $\sigma \sim F_2(x, Q^2)$ . The structure functions can be expressed by the underlying parton density distributions which describe the probability of finding a quark, antiquark or a gluon carrying a momentum fraction  $x$  of the proton when it is probed by a photon carrying the momentum  $Q^2$ . Parameterizations of the parton distributions are obtained using existing DIS data.

<sup>4</sup>The notations "before" and "after" are not well-defined as time-sequences in the a Gauge-invariant field theory

<sup>5</sup>Stable here means that the hadrons have a sufficient lifetime to reach the detector and be observed.

### 2.2.1 The Quark Parton Model

The quark parton model (QPM) is the simplest model of the partonic final state in DIS. In this model the DIS process is described by a mechanism where a quark, carrying a momentum fraction  $x$  of the proton, scatters on the virtual photon. This is shown in the hadronic  $cms$  in figure 2.2. Furthermore, the QPM does not contain radiation of gluons and quarks (QCD radiation), which means that the scattered quark (and therefore the direction of the hadron jet<sup>6</sup>) will be collinear with that of the virtual photon, i.e. it will have no transverse momentum  $P_T$  relative to the virtual photon. Although QPM is a simple model that does not describe data at high energies, it can still be useful in order to estimate the effects of QCD radiation.

### 2.2.2 Matrix Elements

In deep inelastic scattering processes, radiation of quarks and gluons may give large corrections to the overall topology of an event. When the available energy increases, such QCD emissions become increasingly important and have a larger impact on the event topology. In order to take parton emission into account there are two traditional approaches available, the matrix elements method and the QCD parton cascade method.

With matrix elements it is in principle possible to give an exact description of any partonic final state configuration to any order in  $\alpha_s$ . However, in practice matrix element calculations become increasingly complex as the number of partons involved increases, and it is only recently that matrix elements in DIS have been successfully calculated to second order in  $\alpha_s$ .

The Monte Carlo programs used in this analysis include only zeroth and first order matrix elements. The zeroth (or leading) order  $\alpha_s$  process<sup>7</sup> is the basic DIS process where a quark scatters on the virtual photon ( $\gamma^*q \rightarrow q$ ). The two first order  $\alpha_s$  processes are the QCD-Compton process ( $\gamma^*q \rightarrow qg$ ), where a hard gluon (i.e. an energetic gluon) is radiated, and the photon-gluon-fusion process ( $\gamma^*g \rightarrow q\bar{q}$ ) where the virtual photon couples either to the quark or to the antiquark stemming from a gluon in the proton. The QCD-Compton and the photon-gluon-fusion processes are illustrated in figure 2.4.

The matrix elements method is well suited to describe emission of energetic partons at large angles, but does not make sense (i.e. it becomes mathematically undefined) when the gluon energy or the opening angle between the partons approaches zero. In Monte Carlo simulation it is necessary to impose a cutoff to avoid the singular regions of the matrix elements. This can be done by requiring a minimum invariant mass  $m_{ij}$  between any pair of partons in the final state, including the parton spectator system<sup>8</sup>.

### 2.2.3 QCD Parton Cascades

One way of taking parton emission into account is to use an approximation of higher order  $\alpha_s$ -processes, corresponding to an iteration of the lowest order emission. These processes

---

<sup>6</sup>A jet is a collimated flow of particles.

<sup>7</sup>The coupling constant at the vertex is  $\alpha$ . There is no  $\alpha_s$  coupling in this event. Hence the term zeroth order process.

<sup>8</sup>The spectator parton system is the system formed by the remaining quarks in the proton that did not interact with the boson.

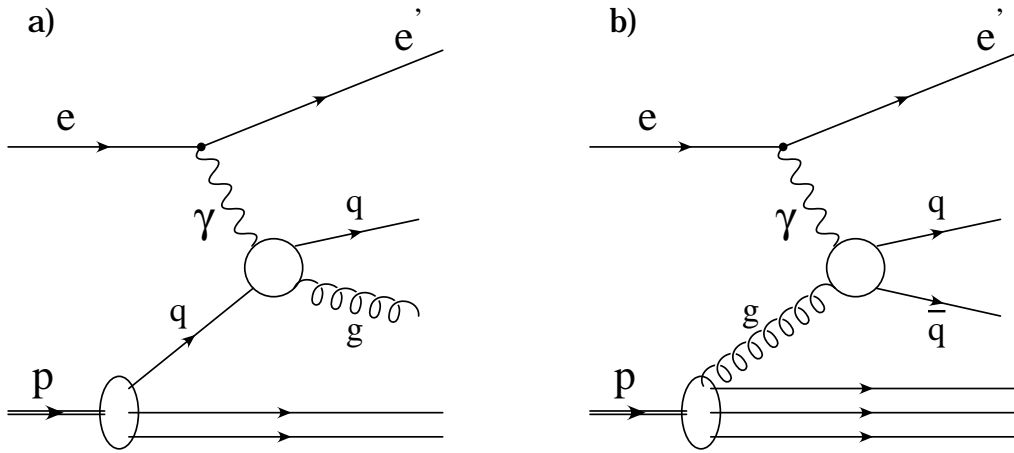


Figure 2.4: The first order  $\alpha_s$  processes, the QCD-Compton (a) and photon-gluon-fusion (b) processes.

are called parton cascades. The two ways, discussed here, of modeling QCD multiple parton emission are the Parton Shower (PS) approach in the leading log approximation and the Color Dipole Model (CDM). These models are described in the following subsections.

### 2.2.3.1 Parton Showers in the Leading Logarithmic Approximation

A parton shower is composed of many subsequent branchings,  $a \rightarrow bc$ , that form a tree-like structure. The different types of branches are  $q \rightarrow qg$ ,  $g \rightarrow gg$  and  $g \rightarrow q\bar{q}$ .

The struck quark may radiate partons both "before" and "after" the photon interaction vertex. Radiation "before" the vertex is called initial-state parton showers while radiation "after" the vertex is called final-state parton showers.

In perturbative parton showers (or cascades), a parton close to the mass-shell in the incoming proton can initiate a parton shower. In such a cascade the incoming parton becomes increasingly off-shell with a space-like virtuality ( $m^2 = E^2 - \vec{P}^2 \leq 0$ ) with each gluon radiated. The emitted gluons will either be on-shell or have a time-like virtuality ( $m^2 = E^2 - \vec{P}^2 \geq 0$ ). This part of the radiation is the initial-state radiation. The resulting space-like quark is then struck by the boson and turned into an outgoing quark which is either on the mass-shell or has a time-like virtuality. In the latter case a final-state, or time-like, parton cascade will be initiated. The quark will radiate gluons, thereby decreasing its virtuality, until it is essentially on its mass-shell. The emitted gluons may be on-shell or have a time-like virtuality, in which case they also will radiate partons. Any parton from the initial-state shower having a time-like virtuality, will also radiate partons. The space- and time-like showers are schematically shown in figure 2.3, and in practice this is the way the processes are described by Monte Carlo routines.

A parton continues to radiate new partons until its virtuality is below some cut-off value, in which case the radiation is terminated. The cut-off value is usually of the order of the hadron mass, i.e. about  $1 \text{ GeV}^2$ .

The amount of radiation in the initial- and the final-state cascade depends on the virtuality of the quark just before and after the boson vertex, respectively. The phase-space limit of this maximum virtuality is given by  $W^2$ . (Higher virtuality results in more partons being emitted.)

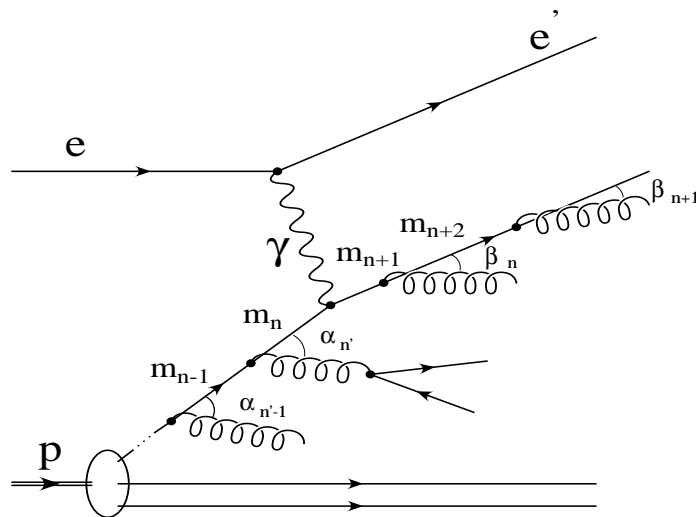


Figure 2.5: *Initial- and final-state parton shower depicted in the case where a quark interacts with the virtual photon. The initial-state (space-like) radiation occurs before and the final-state (time-like) radiation after the photon-quark vertex. The emission is ordered in invariant mass, i.e.  $m_{n-1}^2 < m_n^2 > m_{n+1}^2 > m_{n+2}^2$ .*

The parton emission is ordered in virtuality (increasing in the initial- and decreasing in the final-state) by the requirement that the four-momenta are conserved at each vertex, see figure 2.5. As a result, the emission is also on average ordered in emission angles.

The parton showers scheme, discussed in this section, gives a good description of the emission of soft partons (i.e. partons with low energies) and partons close to the direction of the emitting parton. However, this is not the case for hard partons or partons emitted at large angles. The ME on the other hand, describes these types of emissions in a correct way. This implies that in a Monte Carlo program where parton showers are matched to the matrix elements, both hard and soft radiation should be adequately described<sup>9</sup>.

### 2.2.3.2 The Color Dipole Model

The color dipole model (CDM) is based on the observation that the emission of a gluon from a  $q\bar{q}$  state can be viewed as radiation from a color dipole between the quark and the antiquark. The radiated gluon itself carries color charge, which means that the radiated gluon will act as a kink on the color string between the quark and the antiquark. In the case of emission of a second gluon, this kink may be viewed as dividing the  $qg\bar{q}$  state into two color dipoles, one between the  $q$  and the  $g$  and one between the  $g$  and the  $\bar{q}$ , which radiate approximately independent of each other. Each further radiated gluon gives rise to a new color dipole which can radiate gluons. In this way a chain of radiating color dipoles, stretching from the quark to the antiquark ( $qg\dots g\bar{q}$ ) is formed.

In contrast to the PS model, the CDM does not divide the parton emission of a DIS process into initial- and final-state radiation. Instead all radiation is assumed to

<sup>9</sup>The ME is used to generate the hard subprocess (zeroth or first order) and, by using parton showers, extra softer emissions are added.

be described by the color dipole formed between the scattered point-like quark and the proton remnant which is an extended object.

The available kinematic region (or phase-space) for emission of a gluon with a transverse momentum ( $P_T$ ) and a (pseudo-)rapidity ( $y$ ) with respect to the original axis in the dipole  $cms$ , for a dipole with the  $cms$  energy  $W$ , is:

$$P_T \cosh y < \frac{W}{2} \quad (2.9)$$

This expression is approximately equal to

$$|y| \leq \ln \left( \frac{W}{P_T} \right) \quad (2.10)$$

which is described by the interior of a triangle in the  $(y, \ln P_T^2)$  plane (see figure 2.6).

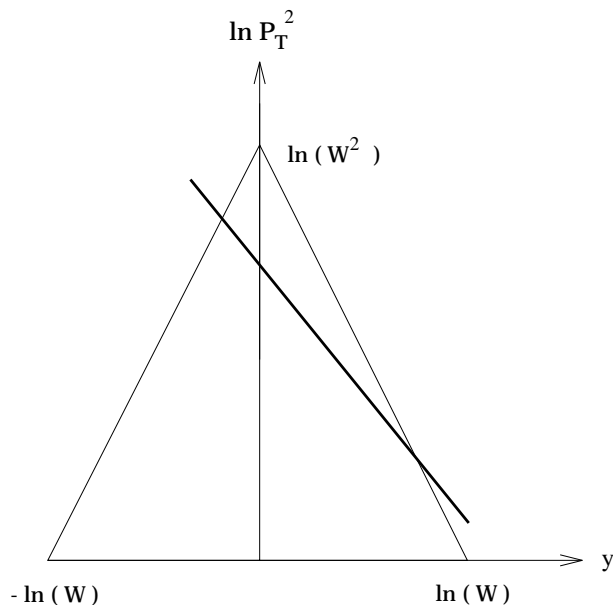


Figure 2.6: *The phase-space limits for dipole emission in the hadronic cms. Positive rapidity ( $y$ ) corresponds to the direction of the proton remnant while negative  $y$  corresponds to the direction of the struck quark. The thick line shows the reduction due to the extension of the proton remnant.*

However, since the proton remnant is an extended source, the following has to be considered. Emissions corresponding to small wavelengths,  $\lambda$  from an extended source are suppressed and for a source with a certain transverse size  $L$  only a fraction proportional to  $\lambda/L$  is effectively participating in the emission. In the CDM this is taken into account by allowing only a fraction  $\mu/P_T$  of the proton momenta to take part in the radiation and hence a radiated gluon may at most carry away this fraction of the remnant energy momentum.  $\mu$  is a parameter related to the the inverse size of the proton remnant.

This means that the available phase-space for radiation is reduced, as shown in figure 2.6, leading to a suppression of emission particularly in the positive  $y$  region. An

important consequence of this is that the maximum allowed  $P_T^2$  of a emitted gluon is given by

$$P_T^2 \leq \left(\frac{W}{2}\right)^{\frac{4}{3}} \mu^{\frac{2}{3}} \quad (2.11)$$

and we see that the phase-space for gluon radiation depends only on  $W^2$ . However, this is not quite the case, as explained later, if matrix elements are included to describe the boson-gluon fusion.

Since the CDM only looks at emission from the dipole between the struck quark and the proton remnant, it will not describe the boson-gluon fusion (BGF) process, where both the quark and the antiquark would create a color dipole with the proton remnant in a correct way.

In order to describe the boson-gluon fusion, the BGF matrix element can be used to generate the basic BGF configuration (i.e. one dipole between the quark and the diquark and one between the antiquark and the other quark from the proton remnant) and color dipole radiation can then be used to generate the additional gluon emission. This is expected to be a good approximation as long as the  $P_T$  of an emitted gluon is much smaller than the relative transverse momentum between the  $q$  and  $\bar{q}$  ( $P_{Tq\bar{q}}$ ). However, the virtuality of the  $q\bar{q}$  pair, taken to be their relative transverse momentum squared  $P_{Tq\bar{q}}^2$ , must be larger than the virtuality of the photon probe  $Q^2$  in order for the event to be treated as a BGF process and two color dipoles to be formed. Otherwise it is treated as a sea quark interaction, i.e. the gluon split into the quark antiquark pair is already included in the evolution of the structure functions.

There are two possible types of sea quark interactions depending on the type of sea quark (a  $q_s$  or a  $\bar{q}_s$ ) picked up by the photon. If it is an antisea quark ( $\bar{q}_s$ ) the proton remnant ( $q_v q_v q_v q_s$ ) is split into a baryon ( $q_v q_v q_v$ ) and a quark ( $q_s$ ) and a color dipole is formed between the antisea quark ( $\bar{q}_s$ ) and the quark ( $q_s$ ). If instead the photon interacts with a sea quark ( $q_s$ ), the proton remnant ( $q_v q_v q_v \bar{q}_s$ ) breaks up into a diquark ( $q_v q_v$ ) and a meson ( $q_v \bar{q}_s$ ) and a dipole is formed between the quark ( $q_s$ ) and the diquark ( $q_v q_v$ ). In either case the subsequent QCD emission is performed in the usual CDM way.

A consequence of using the BGF matrix element is that the phase-space will not depend on  $W^2$  only but to a minor extend also on  $Q^2$ <sup>10</sup>, indicating that multiplicity and the transverse energy flow should mainly depend on  $W^2$  but also to some extent on  $Q^2$ .

## 2.2.4 Fragmentation

The models summarized in the previous sections are all based on perturbative QCD which describe short-distance interactions between quarks, antiquarks and gluons. The process when colored partons are transformed into colorless hadrons, called fragmentation or hadronization, is a long-distance process. This can not be described with perturbative QCD, because QCD becomes strongly interactive at long distances and perturbation theory breaks down. Therefore, in order to describe the fragmentation process, a complementary picture is needed. Since the fragmentation process is not yet fully understood from a theoretical point of view, the models describing the fragmentation process are of

---

<sup>10</sup>Since the structure functions used in the matrix element calculations are functions of  $Q^2$  a dependence on this parameter is introduced.

the phenomenological kind. Although there are a couple of different fragmentation models available, only the Lund String Model <sup>11</sup> [12] together with a model for the proton remnant fragmentation will be described here, as these are the ones used by the Monte Carlo programs Lepto [9] and Ariadne [10].

### 2.2.4.1 String Fragmentation

The partonic final state is the starting point of the fragmentation. In the Lund String Model [12] scheme a color flux tube, a string, is stretched between two colored objects, for example a quark and an antiquark. (If a gluon is present, it is treated as kinks on the string, carrying momentum and energy. As a consequence, the gluon has two string pieces attached.) A flux tube is assumed to be uniform along its length and the potential energy stored in it rises linearly with the length of flux tube. As the colored objects move apart their kinetic energy decreases and the potential energy in the string increases until the string contains sufficient potential energy for a  $q\bar{q}$  pair to be created. The string breaks up and two new string systems are formed. If the invariant mass in either of the strings is large enough the string breaks once more and a new  $q\bar{q}$  pair is produced. This continues until only on-mass shell hadrons remain. The fragmentation process is schematically shown in figure 2.7.

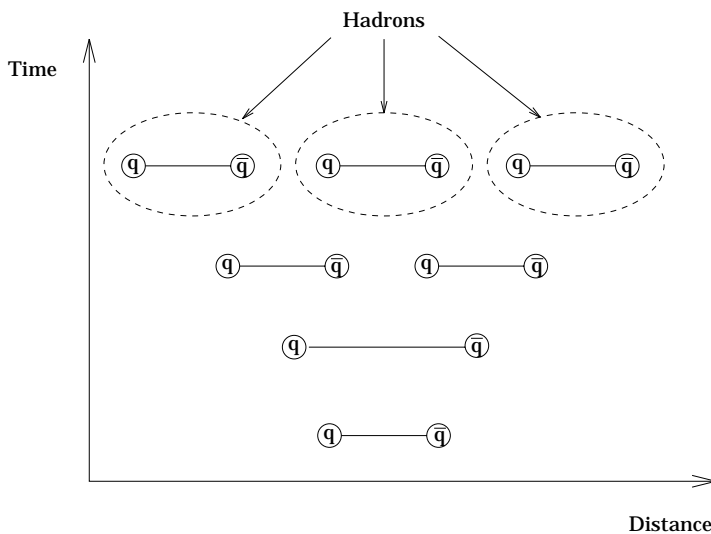


Figure 2.7: A schematic view of the fragmentation process. As the quark and antiquark move apart the energy in the string increases. When the energy in the string is sufficiently great, the string breaks up into a quark and an antiquark and two new string systems are created. This continues till all the energy in the initial string system is used for particle creation.

Each hadron corresponds to a small piece of string with one quark in one end and an antiquark in the other. Each time a string breaks, the newly created quark and antiquark acquire some transverse energy. The total transverse energy of a hadron is made up of the transverse energy of the quark and antiquark.

<sup>11</sup>Other models are cluster fragmentation and independent fragmentation

In this scheme the production of heavy quarks is suppressed because of their large masses. The relative production rates of the quarks are,  $u : d : s : c \approx 1 : 1 : 0.3 : 10^{-11}$ . Hence, charm and heavier quarks are not expected to be produced in string fragmentation, but only in parton showers.

String fragmentation is infrared stable with respect to soft and collinear gluon emission, i.e. the result on the hadron level will not depend on the presence of soft and/or collinear gluons. Two gluons which have a sufficiently small relative mass (e.g. smaller than the hadronic mass scale) will end up in the same hadron anyway.

#### 2.2.4.2 Proton Remnant Fragmentation

In DIS events the momentum transfer ( $Q^2$ ) is always large enough to break up the proton into a parton and a proton remnant. There are four possible configurations of the proton remnant, depending on which type of parton the virtual photon interacts with.

If the struck quark is a valence quark ( $q_v$ ) the proton remnant will simply be a diquark composed of the two remaining valence quarks. A color triplet string is stretched between the color triplet struck quark and the color antitriplet diquark.

If a sea quark ( $q_s$ ) is scattered, the remnant consists of three valence quarks and the antiquark associated with the struck sea quark ( $q_v q_v q_v \bar{q}_s$ ). The remnant can either form a meson and a diquark or just a diquark, depending on the flavor of the struck sea quark. In either cases a string is formed between the diquark and the struck sea quark.

In the case of an antiquark ( $\bar{q}_s$ ) being hit, the remnant consists of four quarks ( $q_v q_v q_v q_s$ ). Three quarks ( $q_v q_v q_s$ ) are combined to form a baryon and the remaining valence quark forms a string system with the scattered antiquark.

If a boson-gluon fusion occurs a gluon is removed from the proton leaving the remnant ( $q_v q_v q_v$ ) in a color octet state. The remnant is split into a quark and a diquark, each forming a separate string with the antiquark and quark, respectively. This will in general lead to a higher multiplicity, since two strings are formed.

If the event is an order  $\alpha_s$  gluon radiation process (QCD-Compton) the string is stretched from the scattered quark via the gluon to the proton remnant.

The strings systems formed in the different cases above hadronize as described in the previous section.



# Chapter 3

## Monte Carlo Generators

The first section in this chapter will deal with Monte Carlo generators in general and how they work. This is followed by two sections describing the Monte Carlo generators Lepto [9] and Ariadne [10] with respect to their use in simulating  $ep$  scattering events at HERA.

### 3.1 Generators in General

The most characteristic feature of high-energy collisions between particles is the production of a multi-particle final-state. A typical DIS event at HERA consists of about 10–20 charged particles and as many neutral ones. It is more or less impossible to make exact probabilistic calculations of the possible final-states of a HERA DIS event. Instead the use of the Monte Carlo (MC) generators presents a way out.

With the MC generators it is possible to generate or produce 'events' with the same behavior and fluctuations as existing data. In the generation of an event, all relevant variables are picked at random (thereof the name Monte Carlo) according to probability distributions. These distributions can either have been measured in experiments or derived from theoretical calculations.

In preparing a physical analysis the MC generators are used for a couple of reasons. Firstly, they give the physicist a feeling of which type of events can be expected and at which rates. Secondly, properties of the events can be studied, helping to develop an analysis strategy that can be used on real data. Thirdly, detector acceptances and efficiencies can be studied to estimate corrections which have to be applied to the raw data in order to extract the underlying physics.

The generation of an DIS  $ep$  event is done in the following way: The type of hard subprocess is chosen according to its probability of occurring (for example the QCD-Compton process). Gluon radiation is added by the use of parton cascades. The partons, together with the beam proton remnant, are turned into hadrons through the fragmentation process.

### 3.2 Lepto

The MC program Lepto 6.01 simulates and generates complete deep inelastic lepton-nucleon scattering events based on the standard electroweak theory for hard parton level

interactions. First order QCD matrix elements, i.e. QCD-Compton and boson-gluon fusion, are implemented and higher order QCD radiation is treated, using parton showers in the leading logarithm approximation. The hadronization is performed using the Lund String Model [8] as implemented in the MC program Jetset 7.3 [12].

There are a number of different ways of simulating the QCD radiation available in Lepto, but only the options used in this study will be discussed here. These options, controlled by the parameter LST(8), are parton showers alone (PS), parton showers matched to the matrix elements (MEPS) and no QCD effects.

### 3.2.1 No QCD effects

With this option Lepto does not generate any gluon emission. Without gluon emission the generated particles should not obtain any transverse momentum in the hadronic *cms* except for what is provided by the intrinsic transverse momentum of the partons in the proton and contributions due to the fragmentation process. In the following, when comparing MC with data, the 'no QCD effects' option will be called the QPM option, although the effects from the intrinsic transverse momentum and the fragmentation are usually ignored in QPM.

### 3.2.2 Parton Showers

The parton shower in Lepto is based on the leading logarithm approximation. Coherence effects are taken into account in the final-state parton shower by angular ordering of the emitted partons, while in the initial-state shower the partons are only ordered in virtuality.

The way of choosing the maximum allowed virtuality  $v_{max}$  is of significant importance [13], since it determines the amount of partons emitted in the shower as well as their hardness. For example, the multiplicity and mean transverse energy will strongly depend on  $W^2$  or  $Q^2$  if the maximum virtuality evolves with any of these variables.

If Lepto is used with the parton shower option, it is possible to choose the maximum virtuality in different ways. (Note that this is not the case if option MEPS is used.) The default is  $Q^2(1-x)_{max}(1, \ln \frac{1}{x})$  which is derived from theoretical considerations. Other possible choices are  $W^2$ ,  $Q^2$  or  $W\sqrt{Q^2}$ . However, previous data have already excluded the default scale as well as choices of the extreme scales,  $W^2$  and  $Q^2$  [14] [15]. Therefore in this study, the scale of the maximum virtuality in the parton shower is chosen to be  $W\sqrt{Q^2}$  and will be denoted 'PSWQ' when comparing data with MC. This choice of the maximum virtuality scale is supported by recent results from HERA.

In Lepto the boson-parton vertex is the starting point for the evolution of the parton showers. The final-state cascade is evaluated 'forward' in time, while the initial-state cascade is evaluated 'backward'. This means that in the initial-state shower the invariant mass decreases as the radiation is followed from the boson vertex 'down' to the on-shell partons in the incoming proton.

### 3.2.3 Matrix Elements with Parton Showers

With this option, parton showers are added to the matrix elements, which means that the hard subprocess is generated using the matrix elements and the soft parton radiation is

added using parton showers. As was mentioned in section 2.2.3.1 this should in principle give a good description of both hard and soft radiation.

To avoid divergences in the matrix elements, Lepto requires the invariant mass,  $m_{ij}^2$ , between any pair of partons (i,j) in the final-state to be larger than  $m_{ij}^2{}_{cut} = y_{cut} W^2$ . The value of the free parameter  $y_{cut}$  can be specified by the parameter PARL(8) in Lepto. When adding parton showers to matrix elements it is important that the maximum virtuality  $v_{max}$  of the parton shower is determined in such a way that double counting of the hard emission is avoided, i.e. a parton in the parton cascade should not be emitted with a larger virtuality than the hard emission generated with the matrix elements.

With MEPS,  $v_{max}$  is determined in three different ways, depending on the type of hard subprocess generated by the matrix elements. These are as follows:

If a zeroth order process is generated by the matrix element, the invariant mass  $m_{ij}^2{}_{cut}$ , used in the matrix elements is used as  $v_{max}$  in the final-state parton shower.

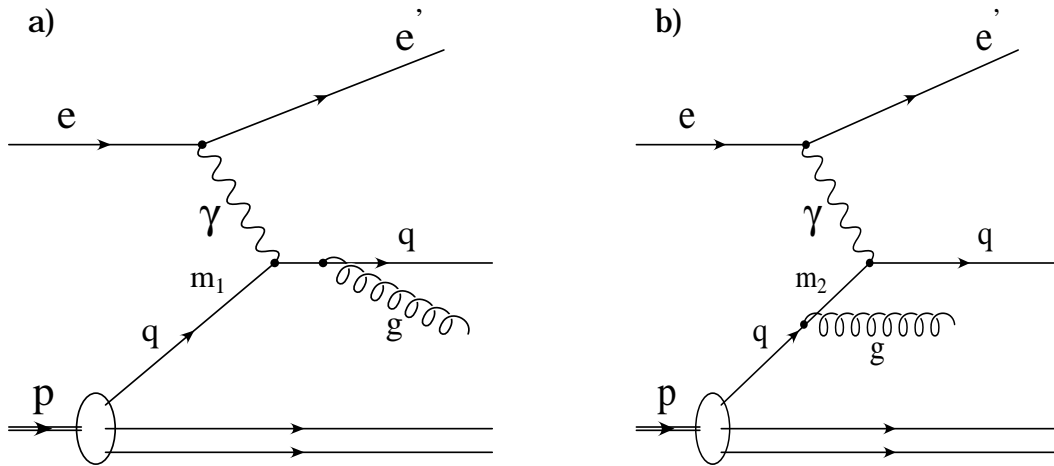


Figure 3.1: *The Feynman diagrams for the QCD-Compton process. The virtuality at a point just before the boson vertex is calculated in each diagram. The maximum of  $m_1$  and  $m_2$  is used as  $v_{max}$  in the initial-state radiation.*

In the case of a QCD-Compton event being generated,  $v_{max}$  for the final-state parton shower is the virtuality of the quark just after it has interacted with the boson. This virtuality is calculated from the two outgoing partons generated by the matrix element. The maximum virtuality  $v_{max}$  for the initial-state shower is the virtuality of the incoming quark just before it interacts with the boson. Since there are two diagrams describing the QCD-Compton process (see figure 3.1), the virtuality just before the boson vertex can be calculated in two ways <sup>1</sup>. In diagram 3.1.a, when a gluon is radiated after the boson vertex, the invariant mass  $m_1$  is calculated from the boson and the two partons. In diagram 3.1.b, when the gluon is radiated before the boson vertex, only the boson and the scattered quark are used for the calculation of the invariant mass  $m_2$ . The maximum absolute value of  $m_1$  and  $m_2$  is then used as the maximum virtuality  $v_{max}$  for the initial-state radiation.

If a BGF event is generated by the matrix element,  $v_{max}$  for the final-state parton shower is calculated in the same way as in the QCD-Compton case above, i.e. from the

<sup>1</sup>As measurements can only be made on the final-state it is impossible to decide whether the gluon was radiated before or after the boson vertex. Therefore both diagrams have to be considered.

two partons generated by the ME. The maximum virtuality for the initial-state shower is determined in the following way. Again  $v_{max}$  for the initial-state shower is the virtuality of the quark just before it interacts with the boson and, as in the QCD-Compton case, there are two diagrams contributing (see figure 3.2). Therefore the invariant masses  $m_1^2$  and  $m_2^2$  have to be calculated for both diagrams. The largest absolute value is then used as  $v_{max}$ .

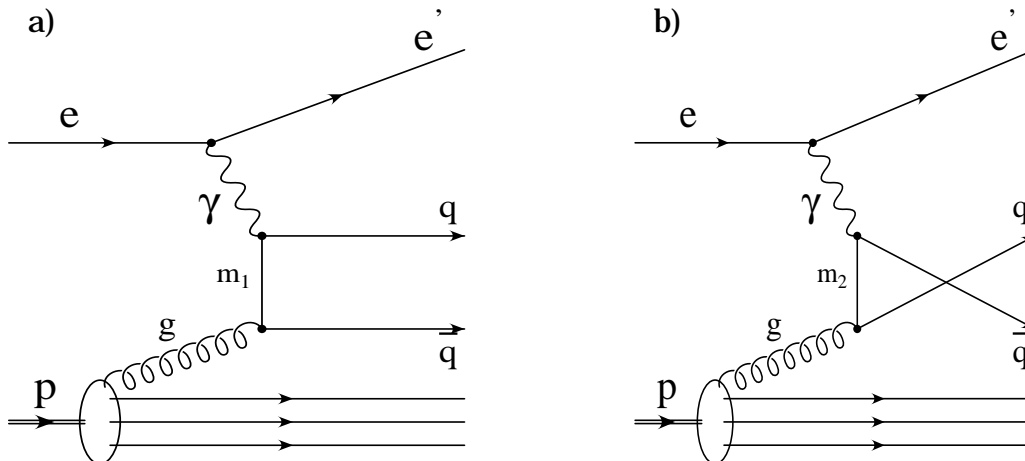


Figure 3.2: *The Feynman diagrams for the photon-gluon fusion process. The invariant masses  $m_1$  and  $m_2$  are calculated and the largest of the two is used as the for  $v_{max}$  the initial-state radiation.*

From the above it can be concluded that there are some drawbacks of the ME+PS option. The probability of generating a specific process ( $\gamma^*q \rightarrow q$ ,  $\gamma^*q \rightarrow qg$  or  $\gamma^*q \rightarrow q\bar{q}$ ) with the ME depends not only on the kinematic variables  $x$  and  $Q^2$ , but also on the cut-off  $y_{cut}$ . For a given  $W^2$  the probability of generating a zeroth order process increases with increasing  $y_{cut}$ , which means that the relative occurrence of the different types of processes in a generated sample will change, i.e. it will contain fewer first order processes. This affects the way the multiplicity and the transverse energy flow varies with  $W^2$  and  $Q^2$ .

### 3.3 Ariadne

Ariadne 4.04 is not a complete event generator but simulates only the QCD radiation process according to the Color Dipole Model. Ariadne therefore uses the Lepto program for the generation of the hard process. The hadronization is performed with Jetsset 7.3. The difference between generating an event with Lepto or Ariadne is the parton cascade, see figure 3.3, and the way in which a QCD-Compton process generated by the ME is treated.

The hard process generated by Lepto is the input to Ariadne. Depending on the type of hard process generated by the ME in Lepto, Ariadne will act in different ways. If the hard subprocess process is a  $\gamma^*q \rightarrow q$ , a dipole is formed between the quark and the proton remnant, and dipole radiation is performed. In the case of a  $\gamma^*q \rightarrow qg$  process, the gluon is removed, as the gluon radiation is assumed to be well described by dipole

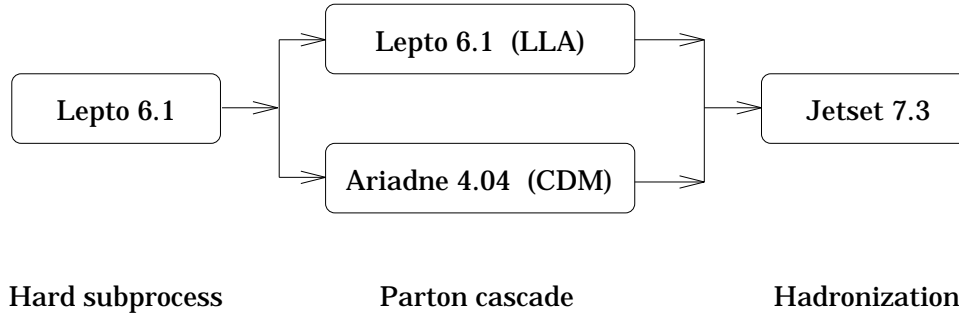


Figure 3.3: *The different steps in the generation of an event. The hard subprocess and the hadronization are the same for both Ariadne and Lepto. By comparing the distributions generated by Ariadne and Lepto with each other and with the one obtained from the data, it is possible to estimate the different effects of the two parton cascade models.*

radiation, and the event is treated as if it had been an ordinary  $\gamma^*q \rightarrow q$ . If a  $\gamma^*q \rightarrow q\bar{q}$  process is generated and the transverse momentum squared between the quark and the antiquark,  $P_{Tq\bar{q}}^2$ , is greater than the momentum transfer  $Q^2$  (multiplied by some factor set by the parameter  $\text{PARA}(20)$ ) the event is treated as an BGF type process. Two color dipoles are formed ( $q - p_{\text{remnant}}^{\text{diquark}}$  and  $\bar{q} - p_{\text{remnant}}^{\text{quark}}$ ) and parton emission is performed using the the CDM with an extra requirement that the  $P_T$  of the emitted partons should be less than  $P_{Tq\bar{q}}^2$ , controlled through parameter  $\text{PARA}(6)$ . If on the other hand  $P_{Tq\bar{q}}^2 < Q^2$ , the process is treated as a sea quark interaction, see section 2.2.3.2.



# Chapter 4

## The HERA Collider and the H1 Detector

A brief discussion of the HERA collider is presented together with a short description of the different components of the H1 detector relevant to this study, i.e. the tracker system and the calorimeter. A more detailed description of the H1 detector can be found in [16].

### 4.1 The HERA ep Storage Ring

The collider beam facility HERA [17] is the first electron-proton collider ever constructed. It consists of two circular independent accelerators designed to store 820  $GeV$  protons and 30  $GeV$  electrons respectively. The two counter rotating beams are designed to collide head on (resulting in a center of mass energy  $\sqrt{s} = 314 GeV$ ) at four interaction points spaced uniformly around the 6.3  $km$  circumference. At present only two of interaction points are used for experiments. The main HERA parameters are given in table 4.1 and the layout of the accelerator complex is shown in figure 4.1.

	Design		1993		unit
	$p$ -ring	$e$ -ring	$p$ -ring	$e$ -ring	
Energy	820	30	820	26.7	$GeV$
Luminosity	$1.5 \times 10^{31}$		$1.3 \times 10^{30}$		$cm^{-2}s^{-1}$
Integrated luminosity per year	$10^5$		600		$nb^{-1}$
Interaction points	4		2		
Number of bunches	210	210	90	90	
Bunch separation	96	96	96	96	$ns$
Injection energy	40	14	40	12	$GeV$
Filling time	20	15			$min$

Table 4.1: *The designed values of the HERA storage ring and the values actually achieved during the data taking period in 1993.*

The preaccelerator system which delivers the electrons and the protons to HERA is shown in figure 4.2. Electrons from a 450  $MeV$  linear accelerator (LINAC II) are injected into a small storage ring (PIA), accumulated into a single bunch of 60  $mA$  and injected into the DESY II ring. Here the electrons are accelerated to 7  $GeV$  and transferred to

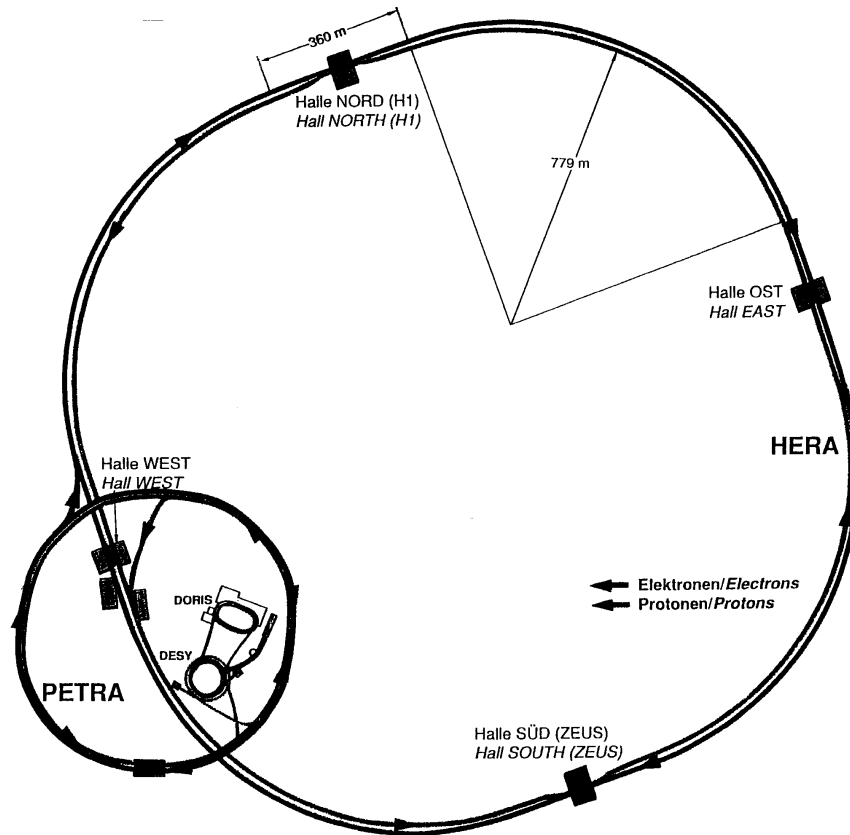


Figure 4.1: The accelerator complex at DESY. The HERA storage ring is filled with electrons, rotating clockwise, and protons, rotating counter clockwise, from the PETRA ring.

the PETRA II ring. In total 70 bunches, each with  $4 \cdot 10^{10}$  electrons, are accumulated in the PETRA II ring, accelerated to 13 GeV and injected into HERA. This is repeated until HERA has been filled with 210 bunches.

The acceleration system for the electrons in the HERA ring consists of 83 conventional and 16 superconducting radio frequency (r.f.) cavities. The energy losses due to synchrotron radiation put a limit to the maximum energy which can be achieved. With conventional cavities it is possible to accelerate the electrons to about 27 GeV and to increase this to the designed 30 GeV, superconducting cavities are needed. The steering and focusing of the beam is made by conventional magnets.

The proton preacceleration is done in a different way. Negatively charged hydrogen ions are accelerated to 50 MeV in the linear accelerator LINAC III. As the hydrogen ions are injected into DESY III the electrons are stripped off. After the protons have been accelerated to 7.5 GeV they are transferred to PETRA II and 70 bunches, each with  $7 \cdot 10^{11}$  protons, are accumulated here. The protons are accelerated to 40 GeV and injected into the HERA main ring. This is repeated until HERA has been filled with 210 bunches.

To keep the 820 GeV protons in a circular orbit in the HERA ring, the dipole bending magnets are required to produce a magnetic field of 4.7 T. This is achieved by using

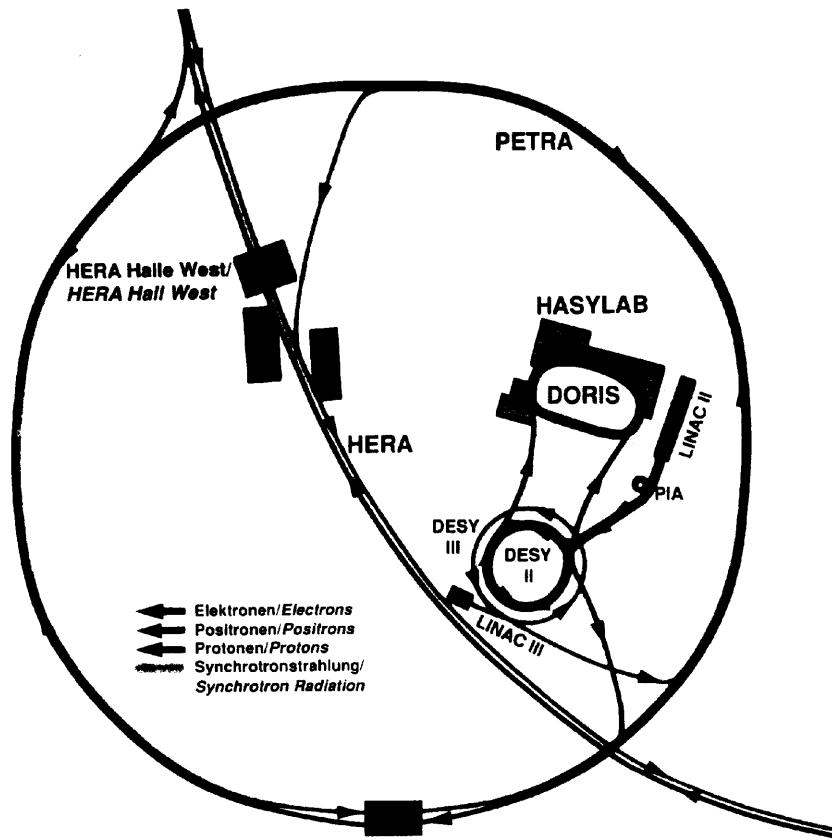


Figure 4.2: The preaccelerator system at DESY. The system consists of the linear accelerators LINAC II and LINAC III and the storage rings DESY II, DESY III and PETRA II.

superconducting magnets made of a niobium-titan alloy which becomes superconducting at liquid Helium temperature (4.5 K). A current of 5027 A is required to pass through the magnets in order to create the required magnetic field.

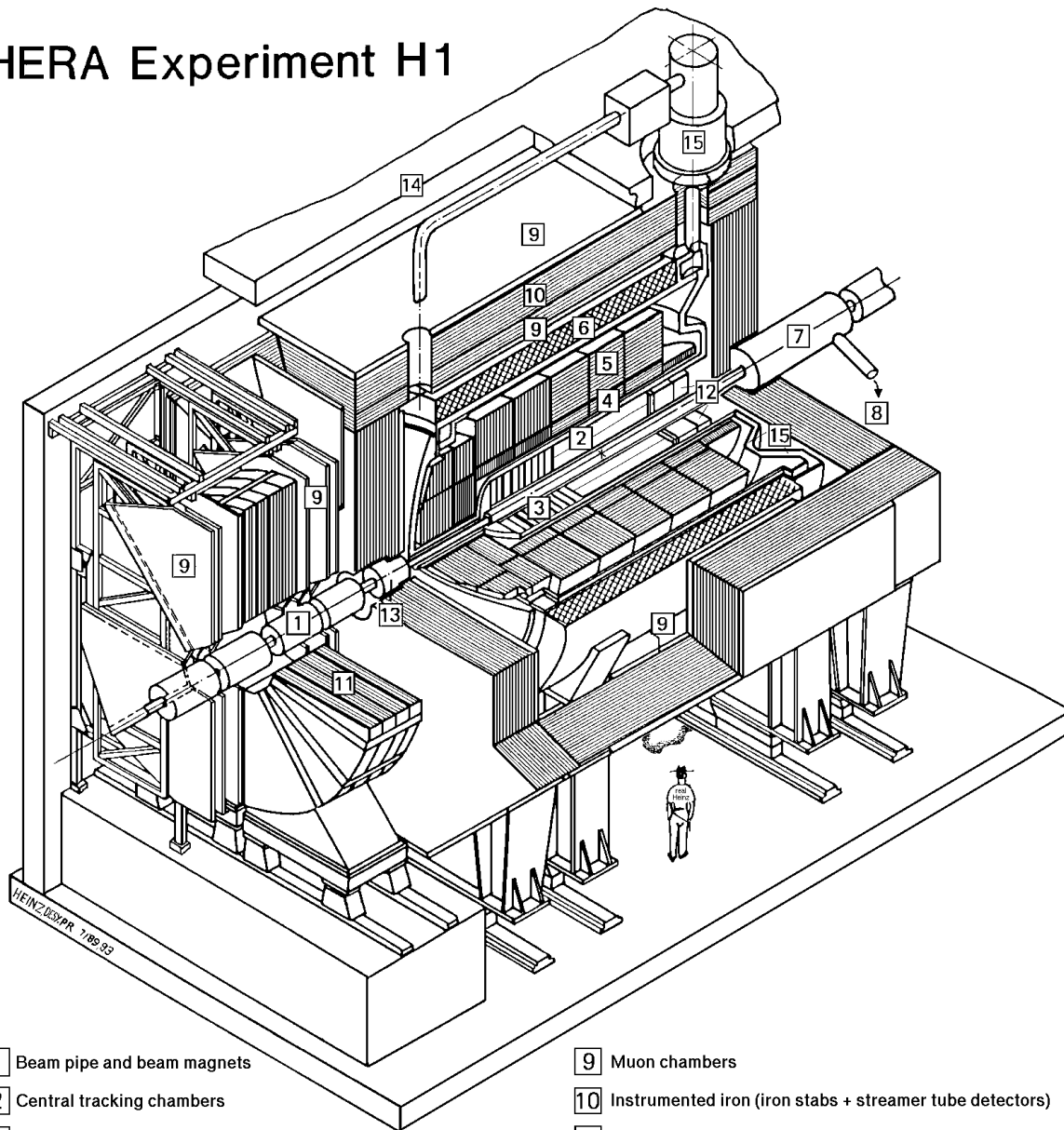
422 superconducting dipole magnets are used to bend the proton beam and 224 superconducting quadrupole magnets to focus it. The acceleration of the protons to the designed energy of 820 GeV is done using a system of conventional r.f. cavities.

## 4.2 The H1 Detector

The H1 detector is one of two detectors built around the interaction regions of the electron-proton storage ring HERA. The 12 m long, 10 m high, 10 m wide and 2800 ton heavy H1 detector is schematically shown in Figure 4.3. The protons enter from the right and the electrons from the left. The imbalance in energy of the two colliding beams results in a considerable boost of the center of mass along the proton direction. This explains the asymmetric design of the H1 detector and the considerably more massive and higher instrumentation in the proton direction.

Referring to the notation of figure 4.3 the detector consists of the following elements

## HERA Experiment H1



- |   |   |    |  |
|---|---|----|--|
| 1 | Beam pipe and beam magnets                | 9  | Muon chambers  |
| 2 | Central tracking chambers                 | 10 | Instrumented iron (iron stabs + streamer tube detectors) |
| 3 | Forward tracking and Transition radiators | 11 | Muon toroid magnet                                       |
| 4 | Electromagnetic calorimeter (lead)        | 12 | Warm electromagnetic calorimeter                         |
| 5 | Hadronic calorimeter (stainless steel)    | 13 | Plug calorimeter (Cu, Si)                                |
| 6 | Superconducting coil (1.2T)               | 14 | Concrete shielding                                       |
| 7 | Compensating magnet                       | 15 | Liquid Argon cryostat                                    |
| 8 | Helium cryogenics                         |    |  |
- } Liquid Argon

Figure 4.3: *The H1 detector.*

starting from the interaction region and moving outwards; a central (2) and a forward (3) tracking system, a liquid argon calorimeter divided into an electromagnetic (4) and a hadronic (5) part, a superconducting magnetic coil (6), the iron return yoke (10), muon chambers outside and inside the the iron return yoke (9), a Si-Cu plug calorimeter (13) in

the forward direction, a forward muon spectrometer (9 and 11), a Pb-scintillator calorimeter (12) and a tail catcher together with two planes of time-of-flight (TOF) scintillator counters in the backward direction and an electron and photon tagger (not shown in figure 4.3) located 33 *m* and 103 *m* respectively from the interaction point in the backward direction. The main purpose of the electron and photon tagger is to monitor and measure the luminosity through the bremsstrahlung process ( $ep \rightarrow ep\gamma$ ). In the following sections, the various components of the H1 detector are discussed in more detail.

## 4.2.1 The Tracking System

The tracking system, covering the polar angular region  $5^\circ - 160^\circ$ , consists of the central and forward tracking systems which are located inside the volume of the superconducting solenoid. The tracking system is depicted in figure 4.4.

### 4.2.1.1 The H1 Main Magnet

The purpose of the H1 main magnet is to produce a magnetic field in the volume of the forward and central tracking systems. This field will bend the trajectories of charged particles, thereby making it possible to determine the charge and the momentum of these particles.

The magnet consists of a superconducting solenoid and an iron return yoke and provides an almost uniform field in the tracking region of 1.15 *T* parallel to the HERA beam. The magnet operates at a temperature of 4.5 *K* with a current of 5500 *A* and is housed in a cryogenic envelope with an overall length of 5.7 *m*, inner and outer diameter of 5.18 *m* and 6.09 *m* respectively and a total weight of 74.5 tons.

The iron return yoke around the superconducting solenoid consists of a laminated structure of iron plates and serves as a flux return for the magnetic field. In addition the iron is instrumented in order to measure the hadronic energy leaking out of the main calorimeter and to identify and measure muons. This is described in section 4.2.2.4.

To compensate for the influence of the main H1 magnet on the electron orbit a superconducting compensation coil is needed. This coil is centered at a point located 4.4 *m* in a negative *z*-direction from the interaction point.

### 4.2.1.2 Central Tracking System

The 2.5 *m* long central tracking system covers roughly the polar angular region  $20^\circ \leq \theta \leq 160^\circ$ . It has been designed to reconstruct jets with high particle densities, requiring a double-track resolution of about 2.5 *mm* and to measure momentum and angles of isolated charged particles to a precision of  $\sigma_p/p^2 \sim 3 \cdot 10^{-3} \text{ GeV}^{-1}$  and  $\sigma_\theta \sim 1 \text{ mr}$ .

Starting from the interaction vertex, a particle traverses the Inner MultiWire Proportional Chamber (MWPC) (CIP), the Inner Z-Chamber (CIZ), the Inner Jet Chamber (CJC1), the Outer MWPC (COP), the Outer Z-Chamber (COZ), the Outer Jet Chamber (CJC2). The different components of the central tracking system are discussed in more detail in the next three sections.

**4.2.1.2.1 Central Jet Chambers** The main task of the CJC is to measure very accurately the track coordinates of charged tracks in the  $x - y$  plane. In addition a

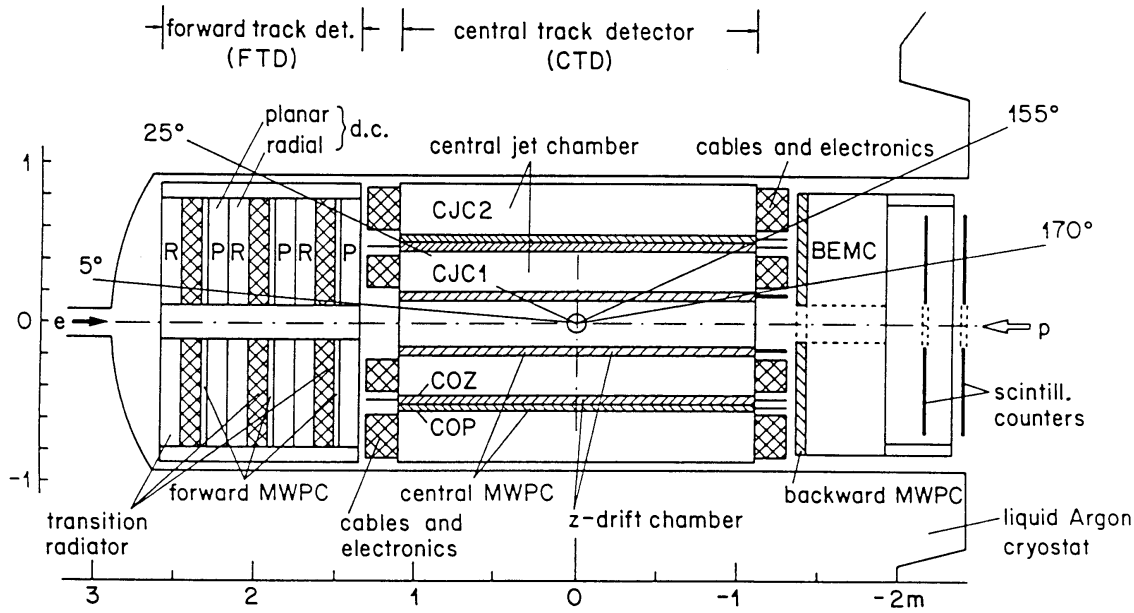


Figure 4.4: *Layout of the tracking system in the H1 detector.*

moderate measurement of the  $z$ -coordinate (along the wire) is provided by so called charge division. The  $z$ -coordinate is used to simplify the linking of charged tracks in the jet chamber with hits in the  $z$ -chamber, which give much higher accuracy of the  $z$ -coordinate. Charge division relies on the fact that the charge collected at either end of an anode ('sense') wire is proportional to the length of the wire from the point at which the charge was induced by the traversing particle. The jet chambers also measure  $dE/dx$  used for particle identification, where  $dE/dx$  is the amount of energy a particle loses through ionization per unit length of material it traverses. Over a certain momentum range the specific energy loss is characteristic for each type of particle, thereby allowing  $dE/dx$  to be used for particle identification.

The active length of the cylindrical jet chambers is  $\sim 2.2$  m. The outer Jet Chamber (CJC2) contains 1920 sense wires and 8460 field wires. The inner and outer radii of the CJC2 are 530.0 mm and 844.0 mm respectively. The Inner Jet Chamber (CJC1), situated inside the CJC2, has an inner radius of 203.5 mm and an outer of 451.5 mm. The CJC1 contains 720 sense wires and 3270 field wires. The wire pattern in the jet chambers is a plane of anode (sense) wires parallel to the beam line and two adjacent cathode wire planes shaping the drift field (see figure 4.5). A jet chamber cell extends azimuthally from the sense wire plane to both adjacent cathode wire planes, and radially over the full radial span of CJC1 or CJC2. The cells are tilted  $\sim 30^\circ$  with respect to the radial direction such that in the presence of the magnetic field the ionization electrons drift approximately perpendicularly to high momentum tracks coming from the center.

An additional advantage of having the cells tilted is that charged particles will pass through several cells, creating track segments in each cell. This is important, because in a drift cell it is not possible to determine the absolute position of individual hits building a track segment, but only the distance from the sense wire plane to the hits. As the

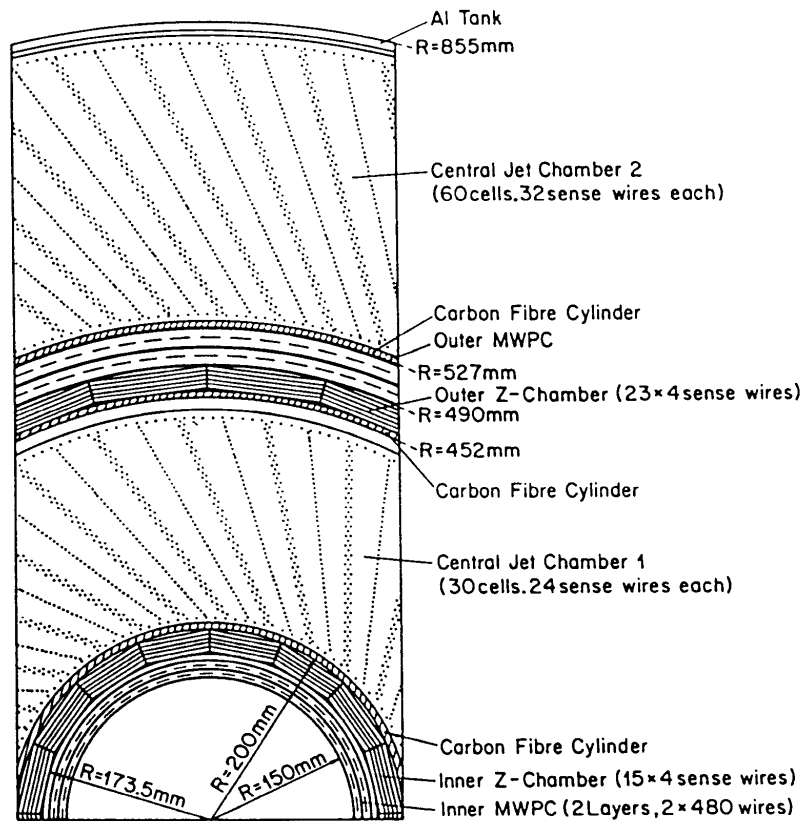


Figure 4.5: Cross section of the drift cells in the central tracking system.

sense wire plane is positioned in the center of the cell, the hits (and the track segment) can be on either side of the sense wire plane. Each particle will therefore give rise to two track segments, a 'real' track segment and a mirror track segment (see figure 4.6). This ambiguity is resolved only when track segments in different cells are connected (the mirror tracks will not match). Thus it is essential for a particle to traverse more than one drift cell.

The cells operate at a pressure of about 1050 mbar with a gas mixture of Argon/Carbon dioxide/Methane. The spatial resolution is  $\sigma_z = 2.2 \text{ cm}$ ,  $\sigma_{r-\phi} = 170 \mu\text{m}$  and  $\sigma_{dE/dx} = 10\%$ . About 56 space points are measured on a track traversing the full radial size of the jet chamber ( $\sim 650 \text{ mm}$ ).

**4.2.1.2.2 Central z- Chambers** The purpose of the two z-drift chambers, the central inner and outer z-chambers (CIZ, COZ), is to measure accurately the z-coordinate of charged tracks. In addition to this, they constitute together with the proportional chambers, part of the first level trigger.

The inner z-chamber consists mechanically of 16 azimuthal sectors and 15 cells in the z-direction. The 1.8 m long 16-edge polygonal chamber has an inner and outer diameter of 347 mm and 400 mm respectively. The outer z-chamber is similar to the inner z-chamber but has an active length of 2.2 m and consists of 24 azimuthal sectors and 24 cells in the z-direction. The chamber has an inner and outer diameter of 920 mm and 970 mm respectively.

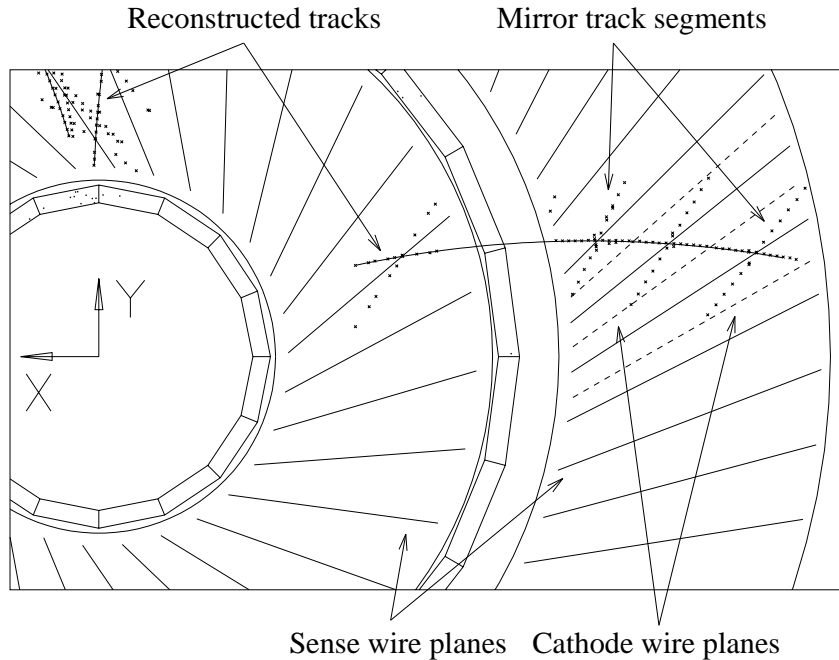


Figure 4.6: Cross section of one part of the central tracking system showing 'true' track segments, linked by the reconstruction program to form a track, and mirror track segments which are 'true' track segments mirrored in the sense wire planes.

The CIZ is presently run with a Argon/Methane gas mixture which gives a single track resolution of  $\sigma_z \sim 0.26 \text{ mm}$  and a double track resolution of  $4.6 \text{ mm}$ . The COZ has a single track resolution of  $\sigma_z \sim 0.20 \text{ mm}$  and a double track resolution of  $3.5 \text{ mm}$  using a gas mixture of Argon/Ethan.

#### 4.2.1.3 The Forward Tracking System

Due to the strong boost of the  $cms$  in the proton direction, most of the particles will be produced with small polar angles  $\theta$ . Since the efficiency of measuring charged particles in the central tracking system (CTS) decreases below  $30^\circ$ , the forward tracking system (FTS) is designed to cover this angular region. The FTS measures accurately momenta and angle ( $\sigma_p/p^2 \sim 3 \cdot 10^{-3} \text{ GeV}^{-1}$  and  $\sigma_{\theta \phi} \sim 1 \text{ mrad}$ ) of charged particles with a  $\theta$  angle greater than  $5^\circ$  (a cut imposed by the beam pipe) but less than  $30^\circ$ , giving some overlap with the CTS. The single space point resolution  $\sigma_{xy}$  is about  $0.15 - 0.80 \text{ mm}$  while the double track resolution is about  $2 \text{ mm}$ . The FTS also provides identification of electrons (transition radiation) and information used in the trigger.

The FTS (see figure 4.4) consists of three identical supermodules inside one gas tank. Moving from the interaction point in a positive  $z$ -direction, each of the three supermodules consists of three planar drift chambers, a multiwire proportional chamber for trigger purposes, a transition radiator and a radial wire drift chamber.

#### 4.2.1.3.1 Planar Chambers

The planar drift chambers are designed to make a precise measurement of the  $x, y$ -coordinates and the momentum of tracks in the forward direction. The three planar chambers situated in a supermodule are oriented perpendicular to the  $z$ -axis. In the direction of increasing  $z$ , the first chamber has the wires oriented

vertically ( $\phi = 90^\circ$ ), the second chamber has the wires along  $\phi = 150^\circ$  and the third chamber has the wires along  $\phi = 30^\circ$ . The result of this is that particles falling within the double hit resolution of one chamber will be resolved by subsequent rotated chambers. Each chamber consists of 32 drift chamber cells each containing 4 sense wires. The cells are mounted to form a disc with a central hole for the beam pipe.

The planar drift chambers operate at atmospheric pressure with a gas mixture of Argon/Propane, bubbled through Ethanol which gives a single point spatial resolution of  $150 - 170 \mu m$ .

**4.2.1.3.2 Transition Radiators** Transition radiation occurs when a particle moves across the interface of two media with different dielectric constants. The intensity of the radiation is proportional to  $E/m$ , where  $E$  and  $m$  are the particle energy and mass respectively.

The transition radiators (TR) are used in combination with the radial drift chamber to discriminate between  $e$  and  $\pi$  in the forward direction. The electron has a mass that is about 270 times less than the pion, and will therefore at a given energy generate more radiation than the pion. For a 90% electron acceptance, the probability that a pion will fake an electron is less than 10%. This is true for particles with energies up to 80 GeV, passing all three modules of the FTS.

The radiator material used is Polypropylene. Layers of Polypropylene fibers provides a sufficient number of dielectric interfaces to produce useful transition radiation in the X-ray region. The interface between the transition radiators and the radial chambers has been optimized to allow the X-rays to be transmitted to the adjoining radial drift chamber.

**4.2.1.3.3 Radial Chambers** The objective of the radial drift chambers is to accurately measure the azimuthal angle  $\phi$  and, through charge division, the radial coordinate  $r$  of forward tracks. In addition, the radial drift chambers are used together with the transition radiators for  $e/\pi$  discrimination. X-rays produced by ultra relativistic charged particles traversing the transition radiators continue into the radial chambers. The X-rays will contribute to an enhanced track ionization, resulting in an increase of the charge collected on one or more sense wires, starting with the wire closest to the TR. This way it is possible to discriminate electrons from pions.

In each of the three FTS modules there is one radial drift chamber. This drift chamber consists of 48 separate drift cells ( $7.5^\circ$  wide) each containing 12 sense wires radially oriented.

A  $\phi$  resolution of  $150 - 200 \mu m$  is achieved with a gas mixture of Argon/Ethane.

#### 4.2.1.4 The Proportional Chambers

There are three multiwire proportional chambers (MWPC) in the forward direction, two in the central and one in the backward direction, see figure 4.4. The purpose of these chambers is to:

1. deliver a fast timing signal with a time resolution better than the separation of two successive HERA bunch crossings.

2. allow moderately accurate reconstruction of space points for charged particle tracks, used at the first level trigger.
3. add an accurate track element in the backward direction, where the drift chambers fail.

The three MWPC in the forward direction (FMWPC) are divided among the three super modules in such a way that each module contains one MWPC. Each of the forward MWPC consists of two wire planes interleaved with three cathode planes.

The two MWPC in the central region are situated so that one chamber, the central inner proportional chamber (CIP), is placed on the inside of the CJC1, close to the beam and the other, the central outer proportional chamber (COP), on the outside of the CJC1.

In the backward direction the reconstruction of the scattered electron at low momentum transfer is important for the determination of the event kinematics. This calls for an accurate space point which, together with the reconstructed vertex, provides the direction of the scattered electron. The purpose of the backward proportional chamber (BPC) is to provide this space point.

The BPC covers the front surface of the backward electromagnetic calorimeter and hence also serves to discriminate electrons and photons. The BPC consists of four sense wire planes oriented horizontally, vertically and  $\pm 45^\circ$  respectively. The BPC covers the polar angle  $155.5^\circ \leq \theta \leq 174.5^\circ$ .

The CIP, COP and BPC uses a gas mixture of Argon/Ethane/Freon12 while the FMWPC uses Argon/Propane.

## 4.2.2 The Calorimeter System

The purpose of the calorimeter system is to measure the energy of charged and neutral particles by absorbing them inside the calorimetric volume. It consists of the large liquid argon calorimeter (LAr) backed up by a forward Si-Cu plug calorimeter (PLUG) and a backward Pb-scintillator electromagnetic calorimeter (BEMC), see figure 4.7. The instrumented iron, situated outside the coil, serves as a complement to the hadronic part of the LAr calorimeter in the forward and central regions and to the BEMC in the backward region. The angular region covered by the PLUG is  $0.6^\circ \leq \theta \leq 3^\circ$ , by the LAr  $3^\circ \leq \theta \leq 153^\circ$  and by the BEMC  $151^\circ \leq \theta \leq 177^\circ$ .

In the following sections the LAr, the PLUG, the BEMC and the the instrumented iron will be described in more detail.

### 4.2.2.1 The Liquid Argon Calorimeter

The liquid Argon calorimeter (LAr) consists of an electromagnetic part, which measures mainly the energy of photons and electrons, and a hadronic part, which measures the energy of hadrons.

The liquid argon calorimeter is located inside the large coil to minimize both the amount of dead material in front of the electromagnetic calorimeter and the overall size and weight of the calorimeter. It consists of 8 wheel segments, two forward and six barrel segments. Each of these wheels (except the backward barrel which has only an electromagnetic part) has 8 electromagnetic and 8 hadronic stacks. A stack is a sandwich arrangement of absorber plates, gaps filled with the active medium liquid argon and

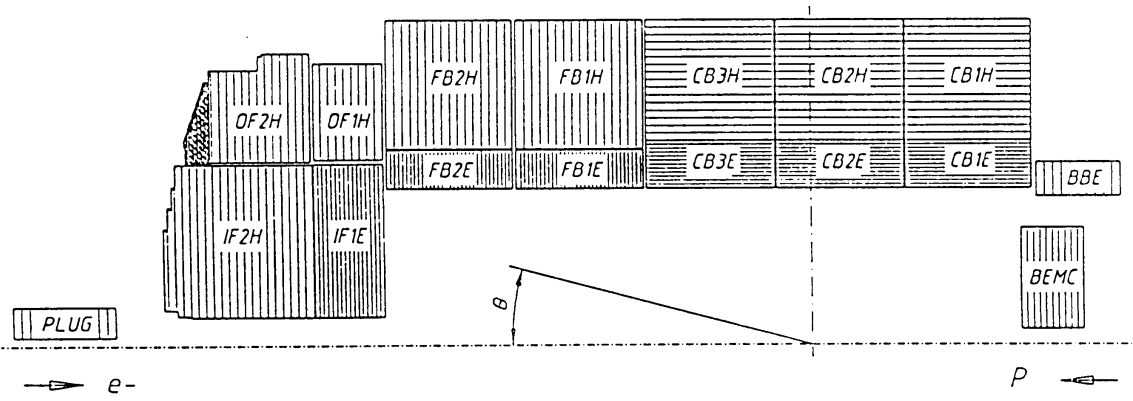


Figure 4.7: Longitudinal view of the calorimeter system.

planes of pad boards used for the signal readout. The absorbing material is stainless steel in the hadronic and lead in the electromagnetic stacks. The total thickness of the electromagnetic part is between 20 and 30 radiation lengths ( $X_0$ ) while the thickness of the hadronic part is between 2 and 8 absorption lengths ( $\lambda_{abs}$ ) depending on the polar angle.

The LAr has an energy resolution  $\sigma_E/E \approx 12\%/\sqrt{E} \oplus 1\%$  for electrons and  $\approx 50\%/\sqrt{E} \oplus 2\%$  for charged pions. The energy scale in the LAr is known to  $\pm 8\%$  for the electromagnetic part and to  $\pm 5\%$  for the hadronic part.

#### 4.2.2.2 The Plug Calorimeter

The Plug Calorimeter (PLUG) is designed to close the gap of acceptance between the forward part of the LAr and the beam pipe. The main task of the PLUG is to minimize the missing part of the total transverse momentum of events due to hadrons emitted close to the beam pipe. The PLUG is a sampling calorimeter consisting of nine copper absorber plates interleaved with eight sensitive layers of silicon detectors.

The PLUG has an energy resolution of about  $150\%/\sqrt{E}$  and a total length (69 cm) corresponding to 44.6 radiation lengths or 4.25 hadronic absorption lengths.

#### 4.2.2.3 The Backward Electromagnetic Calorimeter

The main purpose of the 3 ton backward electromagnetic calorimeter (BEMC), centered at a point located about 2 m from the interaction point, is to measure the energy and direction of electrons scattered with small angles from deep inelastic scattering processes (events with  $5 \leq Q^2 \leq 110 \text{ GeV}^2$ ). In addition the BEMC has to provide energy measurements of hadrons emerging from photoproduction or medium-to-low- $x$ , high- $y$  events.

The calorimeter consists of 88 elements (stacks) as depicted in figure 4.8. They are aligned parallel to the beam and mounted in an aluminum barrel with a diameter of 1.62 m. The stacks are multi-layer lead-scintillator sandwich structures with 50 active sampling layers made of plastic scintillator of 4 mm thickness. The active layers are interleaved with 49 layers of 2.5 mm lead. The entire structure has a thickness of  $22.5 X_0$  or  $0.97 \lambda_{abs}$ .

The energy resolution of the BEMC is about  $10\%/\sqrt{E} \oplus 3\%$  for electrons. For hadrons an energy resolution of approximately  $80\%/\sqrt{E}$  is achieved by combining the energy measurement in the BEMC and in the instrumented iron. The energy scale is known to about 2%.

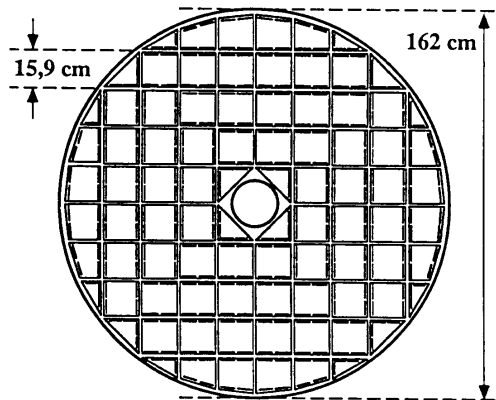


Figure 4.8: Cross section of the backward electromagnetic calorimeter (BEMC).

#### 4.2.2.4 The Tail Catcher

The instrumented iron, also called the tail catcher, covers the polar angle  $6^\circ \leq \theta \leq 172^\circ$ . As was mentioned before, the purpose of the tail catcher is to measure any hadronic energy leaking out of the LAr calorimeter<sup>1</sup> and to identify and measure muons. To accomplish this the iron has a laminated structure where 9 gaps are equipped with limited streamer tubes (LST). The basic elements of the chambers are extruded profiles of the plastic material Luranyl. Each profile consists of eight rectangular streamer tube cells (with a size of  $10 \times 10 \text{ mm}^2$ ) each containing one sense wire at ground potential. Two profiles are contained in one gas tight box and several such boxes form a complete streamer tube layer. On top of this streamer tube layer, either strips or pads are added, depending on the position of the layer in the iron. The strips, oriented perpendicular to the sense wire direction, are used for track measurements and the pads for the measurement of the hadronic energy.

Starting from the interaction point there is first a so called muon-box, installed in front of the iron. It consists of three layers (two strip and one pad). The first three slits in the instrumented iron contain pad layers. The fourth slit is twice as wide as the others and houses two chamber layers (one strip and one pad). The remaining five slits are equipped with pad layers. Behind the iron there is another muon-box containing two strip layers and one pad layer. In total there are 16 (5 strip and 11 pad) streamer tube chamber layers in depth. The gas mixture used in the LST is Argon/Carbon dioxide/Isobutan.

The total thickness of the tail catcher corresponds to 4.5 absorption lengths. The energy resolution is  $\sigma_E/E \sim 100\%/\sqrt{E}$ . In order to make the best possible correct energy measurement the information from the tail catcher has to be combined with information

<sup>1</sup>In 95% of the events the energy leaking into the tail catcher is less than 20% [18].

of the LAr calorimeter. To accomplish this, corrections have to be made for dead material e.g. the cryostat wall and coil between the LAr and the tail catcher.

Tracks in the instrumented iron are reconstructed using all the information available i.e. 16 wire, 5 strip and 11 pad layers. The resolution for the wire and strip hits is 3-4 *mm* and 10-15 *mm* respectively. The pads define crude space points with a precision of about 10 *cm*. The angular resolution  $\sigma_\theta$  is 15 *mr* while the momentum resolution  $\sigma_p/p$  is 0.35%.

### 4.2.3 The Muon System

The muon system consists of the detectors in the instrumented iron, described in the previous section, and the forward muon spectrometer.

The forward muon detector is designed to measure high energetic muons in the polar angular range  $3^\circ \leq \theta \leq 17^\circ$ . The detector consists of six drift chamber planes mounted on either side of the toroidal magnet. Four planes measure the polar angle ( $\theta$ ) and two planes measure the azimuthal angle ( $\phi$ ) (see figure 4.9). To be able to resolve the left-right ambiguity each drift chamber plane consists of two layers of drift cells staggered by half a cell width.

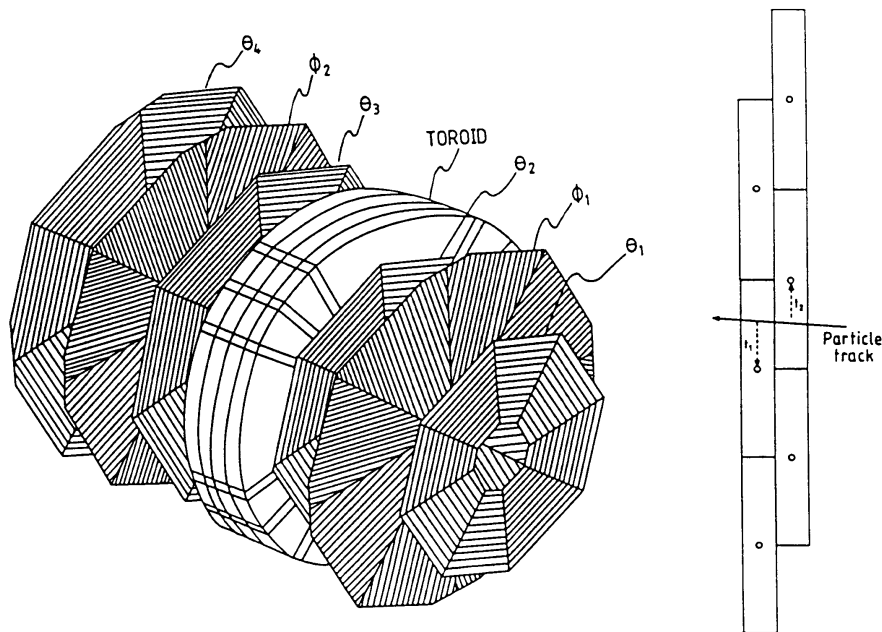


Figure 4.9: A schematic view of the forward muon detector.

The purpose of the toroidal magnet is to produce a magnetic field in which the trajectory of the muons passing the forward muon detector will be bent. This allows the momentum and charge of the penetrating muon to be determined. The inner radius of the magnet is 0.65 *m* and the outer 2.90 *m* and the weight is 250 ton. The magnet is water cooled and operates at 150 *A*, resulting in a magnetic field of about 1.5 *T*.

The drift chamber planes are all divided into octants of individual drift cells mounted on Al-frames. The drift cells have a rectangular cross section of  $2 \times 12 \text{ cm}^2$  and a length between 40 and 240 cm, depending on their position in the drift chamber plane. In total 1520 drift cells are used.

Only muons within the momentum range  $5 - 200 \text{ GeV}/c$  can be measured in the forward muon detector. The upper limit is set by the magnetic field strength in the toroid together with the spatial resolution of the drift chamber. The lower limit is given by the amount of material the muons have to penetrate before they can reach the forward muon system and the influence of the multiple Coulomb scattering in the magnet iron on the momentum resolution.

The momentum resolution  $\sigma_p/p$  varies between 0.24 % for 5 GeV tracks and 0.36 % for 200 GeV tracks. The spatial resolution is  $\sim 250 \mu\text{m}$  with a gas mixture of Argon/Carbon dioxide/Methan.

#### 4.2.4 The Scintillator Counters

There are two scintillator systems located in the backward region of the H1 detector, the time of flight system (ToF) and the so called veto wall, see figure 4.10.

The purpose of the ToF system is to veto proton beam induced background. This background consisting of showers of energetic particles, produced when protons interact either with residual gas (beam gas event) in the beam pipe or with the beam pipe itself (beam wall event).

The veto wall is designed to reject background from high energetic muons originating upstream of the detector, so called beam-halo muons, as these muons can be misinterpreted as high  $Q^2$  interactions.

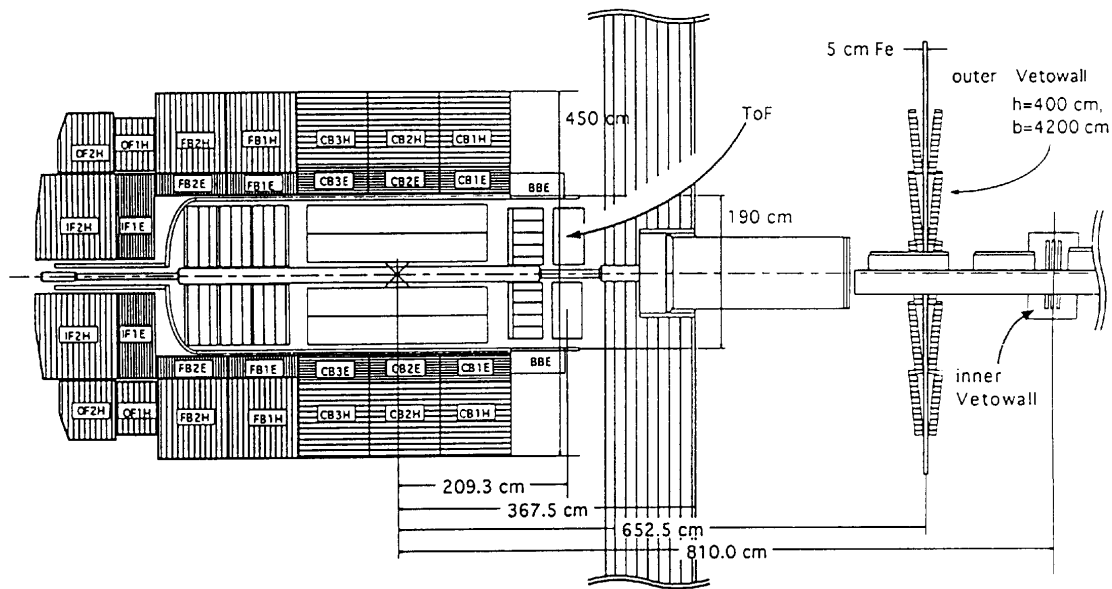


Figure 4.10: The scintillator system and its position relative to the nominal interaction point in the H1 detector.

The time of flight system located upstream from the interaction point at  $z = -2.1$  m consists of two planes of 3 cm plastic scintillator mounted perpendicular to the beam pipe. The plane nearest the interaction point is located at  $z = -1.95$  m and consists of 16 quadratic counters ( $317 \times 317$  mm<sup>2</sup>). The second plane located at  $z = -2.25$  m has eight rectangular counters ( $317 \times 624$  mm<sup>2</sup>). Each wall of ToF is made of one layer of lead and one layer of scintillators. The lead is 6.5 mm ( $1.1 X_0$ ) thick to absorb synchrotron radiation, both to protect the scintillators from radiation damage and to limit the number of triggers from this source. During beam injection there is an increased radiation flux close to the beam pipe and to avoid radiation damage to the scintillator counters, the central part of the counters can be moved up to 20 cm away from the beam pipe.

The ToF system is very efficient in suppressing background events. A 99% decrease in the overall trigger rate is achieved, and subsequently a reduction in the dead-time.

The veto wall consists of two double scintillator walls (outer and inner veto wall) positioned at  $z = -6.5$  m and  $z = -8.1$  m from the interaction point. The outer veto wall consists of 26 large scintillator plates arranged in two layers. The outer veto wall covers approximately a circular area round the beam pipe having an outer and inner radius of 2.5 m and 84 cm respectively. The gap between the outer veto wall and the beam pipe is covered by the inner veto wall down to a radius of 11 cm.

### 4.2.5 The Trigger System

The purpose of the trigger is to select interesting  $ep$  collision events and to reject background events. The collision rate at HERA is 10.4 MHz. With the designed luminosity of  $1.5 \times 10^{31}$  cm<sup>-2</sup>s<sup>-1</sup> the rate of physics event is of the order of 100 Hz<sup>2</sup> while the background event rate is of the order of 100 kHz<sup>3</sup>.

For most physics study the machine induced background is beam gas and beam wall events as well as particle showers induced by synchrotron radiation from the electron beam. However, since this study is performed using high and low  $Q^2$  neutral current DIS events there will be 'physics background'<sup>4</sup> as well. The trigger will remove most of the machine induced background while the event selection performed after the trigger will remove 'physics background'.

The machine induced background comes mainly from upstream from the detector in the proton direction while the  $ep$  events originates from the nominal interaction region. A fast estimation of the vertex is made, based on information from the MWPC and the central drift chambers CJC1 and CJC2. The ToF and VETO is used to determine whether a particle originates from a point upstream or from the interaction point by comparing the arrival time with the HERA clock.

The trigger consists of four levels of increasing complexity. The first level (L1), which is a hardware trigger, reduces the interaction rate by a factor of 50-100, which means that at full HERA luminosity the output rate from the L1 is 1 kHz. The L1 trigger takes its decision within 2.2 μs. The L1 trigger will reject a considerable amount of the background from beam wall, beam gas events and synchrotron radiation. The level 2 (L2) hardware trigger and the level 3 (L3) software trigger work in parallel and use the same information

---

<sup>2</sup>Almost all of this rate comes from photoproduction and only a small fraction from neutral current DIS events.

<sup>3</sup>30 % of the rate is estimated to come from beam gas events and 70 % from beam wall events [19].

<sup>4</sup>Physics background of this study is for example photoproduction and diffractive events.

as in the L1. The difference compared to the L1 is that more time is available for the decision whether an event should be kept or not. The output rate of the L2 and L3 trigger is 200 and 50  $Hz$  respectively with decision times of  $20\mu s$  and  $800\mu s$  respectively. (During the 1993 running period, H1 operated without trigger level 2 and 3.) The level 4 (L4) trigger is a software trigger which reduces the final rate of data logging to about 5  $Hz$ . The L4 analysis is based on charged tracks, clusters and the vertex. At this level the number of beam gas and beam wall events are reduced further through requirements based on the vertex reconstruction.

After the L4 trigger the events are categorized in different event classes making it possible to select a certain event type for the analysis. However, the event sample of a particular class is still not completely pure but will contain some 'physics background', as well as some beam gas and beam wall events. Thus it is necessary to set additional requirements for the events in the off-line analysis in order to purify the sample further. This is described in the next chapter.

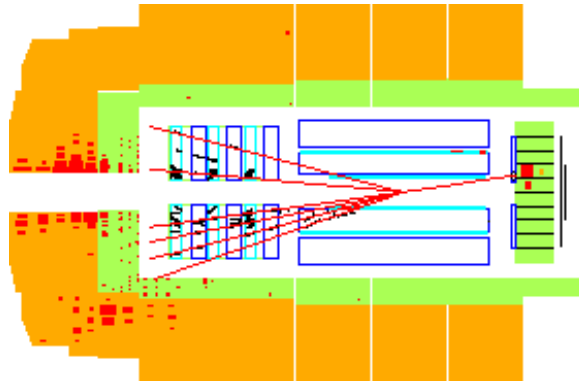


Figure 4.11: *Example of a typical low  $Q^2$  DIS event where the scattered electron is detected in the BEMC.*

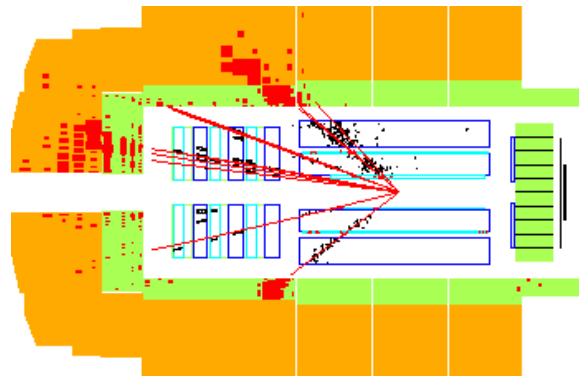


Figure 4.12: *Example of a typical high  $Q^2$  DIS event where the scattered electron is detected in the LAr.*

# Chapter 5

## The Data Analysis

We begin this chapter by discussing the detector simulation and event reconstruction programs and their use. In the sections following this, the criteria for the event, track and cluster selections are discussed. Binning of the event, the correction procedure applied to the data and the systematic errors are also described.

### 5.1 Detector Simulation and Event Reconstruction

A Monte Carlo program that simulates the properties of the detector is necessary for two reasons. First, to prepare the different steps in the analysis, such as for example program development for the data analysis. Second, to be able to study the acceptance and the efficiency of the detector in order to correct measured distributions for these effects <sup>1</sup>. The program H1SIM [20] is used to simulate the performance of the H1 detector.

The simulation of data starts with the production of a Monte Carlo event using an event generator, for example Ariadne. Such an event will be called a Monte Carlo event at the generator level. The event is fed into the detector simulation program which tracks each Monte Carlo generated particle through the detector. The MC particles interact with the dead material and the different subdetectors, e.g. tracker chambers and calorimeters. Multiple scattering, energy losses and particle decay are taken into account according to probability distributions. After the simulation step the event looks like a real event coming from the H1 experiment, with everything known about the event, from the generation to the end of the detector simulation. A Monte Carlo event that has been detector simulated will from now on be called a simulated event.

Simulated events, like data events, are not immediately usable in an analysis, but must first be processed to obtain physical quantities like four-vectors. The program used for the processing is the H1 reconstruction program H1REC [21]. The reconstruction program builds tracks from the hit information in the tracker chambers, calculates the positions of vertices, forms clusters from calorimeter cells and creates four-vectors representing the reconstructed objects. A simulated event that has been reconstructed will from now on be called a reconstructed Monte Carlo event and a reconstructed event from the H1 detector will be called a reconstructed data event.

---

<sup>1</sup>It is necessary to correct the measured distributions for detector effects if they are to be compared with theoretical predictions or results obtained in other experiments with different acceptances and different efficiencies.

The above discussion is summarized in a schematic view in figure 5.1.

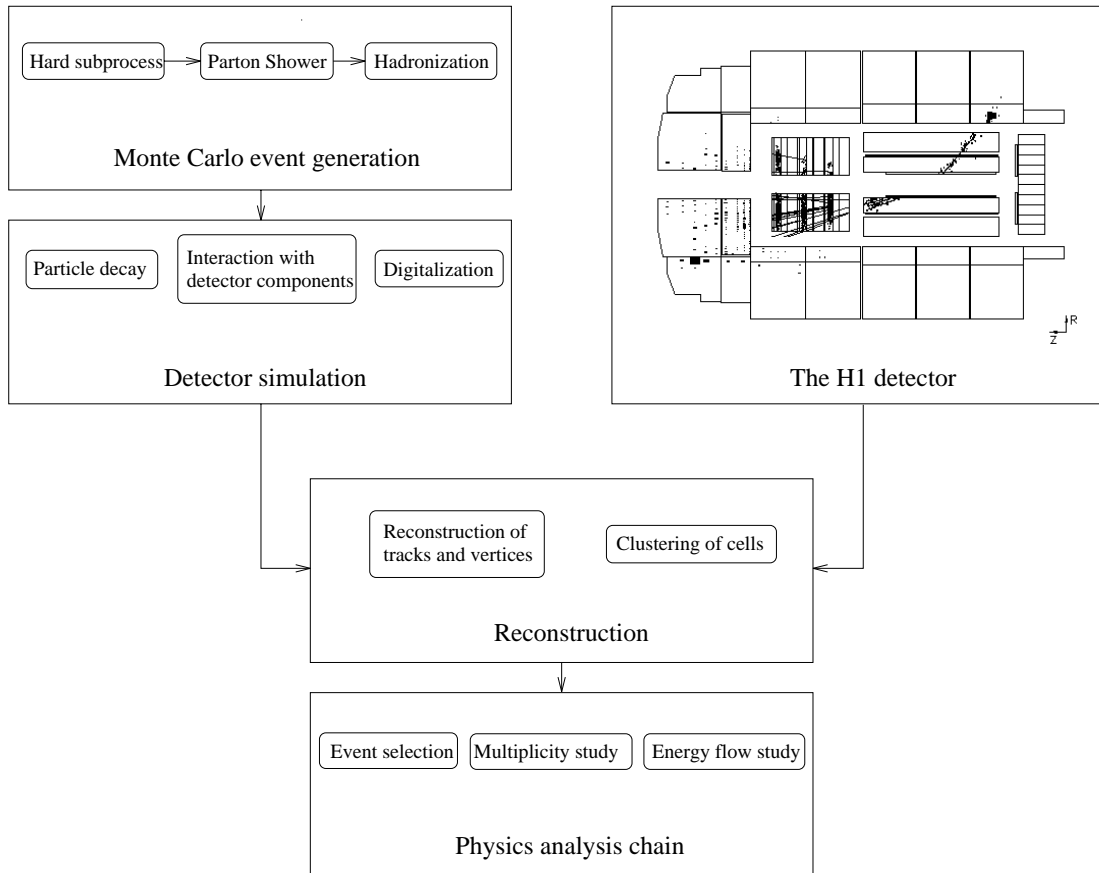


Figure 5.1: *Schematic view of the different steps in the analysis. A generated Monte Carlo event that has been detector simulated corresponds to an event collected in the H1 detector. The events (both data and Monte Carlo) are reconstructed and the analysis is performed.*

## 5.2 Reconstruction of the Event Variables

As was pointed out in section 2.1, from any two of the kinematic variables  $x, y, Q^2, W^2$  the other two can be analytically calculated. In this analysis  $y$  and  $Q^2$  are reconstructed from the detector information and  $x$  and  $W^2$  are calculated using the equations 2.3 and 2.4 respectively.  $Q^2$  is reconstructed using the information from the scattered electron ( $Q_{el}^2$ ). This gives an accurate reconstruction of  $Q^2$  with an average relative error of 0.003 and a sigma of 0.04.

The Bjorken  $y$  is reconstructed in two ways. Either by using only the scattered electron ( $y_{el}$ ) or by applying the double angle  $y_{da}$  method<sup>2</sup> to the calorimeter cells.  $W$  is calculated from  $Q_{el}^2$  and  $y_{el}$ .

<sup>2</sup>Either the double angle (DA) or the Jaquet-Blondel (JB) method can be used to reconstruction  $y$  from the calorimeter cells. However, studies show [22] that the DA method reconstructs Bjorken  $y$  more accurately than the JB method does, and is therefore used in this study.

Since the events in this analysis, are binned in  $W$ , as will be described later in section 5.6, it is very important to minimize the migration between different  $W$  bins <sup>3</sup>, i.e. an accurate reconstruction of  $W$  is needed. This implies that both  $Q^2$  and  $y$  must be measured accurately. For the  $Q^2$  determination, this is already achieved simply by using the scattered electron, see fig. 5.2.a. A sufficient accuracy of  $y$  is achieved by requiring that both  $y_{el}$  and  $y_{da}$  are greater than 0.08. These requirements gives a mean relative error of the  $y_{el}$  reconstruction of 0.004 and a sigma of 0.1 (see fig. 5.2.b. The resulting mean relative error in the  $W$  reconstruction is 0.005 and sigma 0.05 (see fig. 5.2.c).

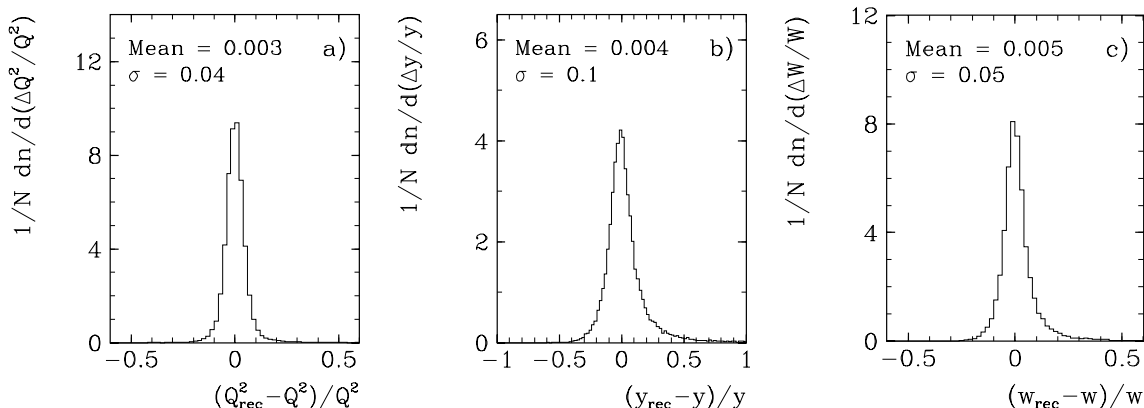


Figure 5.2: *The relative error in the reconstruction of  $Q^2$  (a), Bjorken- $y$  (b) and  $W$  (c). The distributions are obtained after applying the event selection criteria which are described in the following section.*

In figure 5.3 the distributions of the event variables  $Q^2$  and  $W$  in the data are compared to those generated by the Monte Carlo program including a full simulation of the H1 detector. The distributions are obtained after applying the low  $Q^2$  event selection criteria described in the following section. The  $Q^2$  and  $W$  distributions for the high  $Q^2$  data sample are also reproduced by the Monte Carlo

### 5.3 Event Selection

The analyzed data sample consists of neutral current DIS events, collected in the H1 detector during 1993. The energies of the electron and proton beams were 26.7 and 820  $GeV$  respectively. The data sample is split into a 'low  $Q^2$  sample' ( $Q^2 < 110 GeV^2$ ) where the scattered electron is measured in the BEMC, and a 'high  $Q^2$  sample' ( $Q^2 > 110 GeV^2$ ) where the scattered electron is measured in the LAr calorimeter.

For events in the low  $Q^2$  sample, the scattered electron is found by searching for the electromagnetic cluster in the BEMC with the highest energy. The events in this sample satisfy the following requirements:

- The four-momentum transfer squared  $Q^2$  must be between 10  $GeV^2$  and 110  $GeV^2$ .

<sup>3</sup>To achieve this it is not only required that the mean of the relative error in the  $W$  reconstruction is small but also that the sigma, or the relative error, has to be as close to zero as possible.

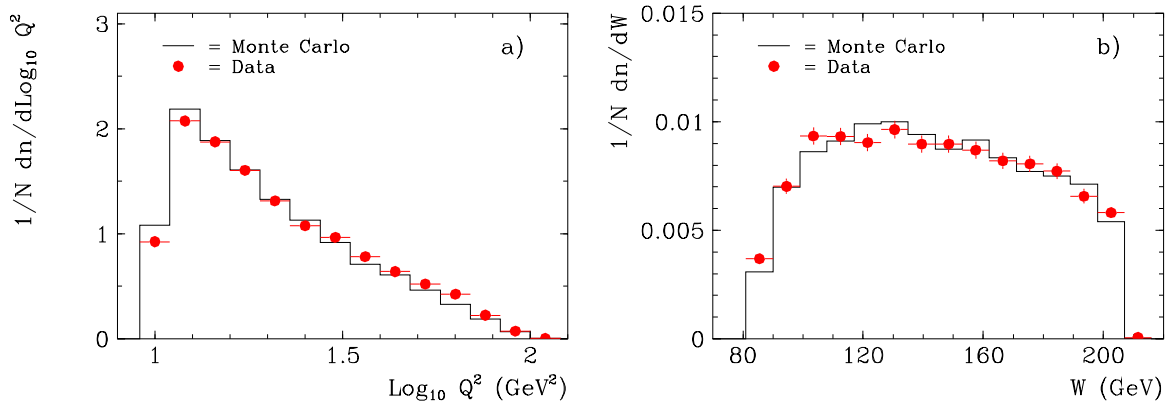


Figure 5.3: *The distribution of the event variables  $Q^2$  (a) and  $W$  (b) for data and Monte Carlo. The distributions are obtained after performing the event selection and show that the event variables in the data are well reproduced by the Monte Carlo.*

- The energy of the scattered electron  $E'_e$ , identified as the most energetic BEMC cluster, must be greater than  $14 \text{ GeV}$ . This corresponds to a  $y \lesssim 0.5$  and will remove essentially all background [23] from photoproduction. In addition the cluster must be associated with a hit in the BPC no more than  $5 \text{ cm}$  from the center of gravity of the BEMC cluster. To ensure a precise energy measurement, the cluster center of gravity must not be too close to the beam pipe: more precisely, either  $|x_{cluster}|$  or  $|y_{cluster}|$  has to be greater than  $14 \text{ cm}$
- The radius of the electron cluster must be smaller than  $5 \text{ cm}$ . Since a hadronic shower is in general broader than an electromagnetic one, this will again further suppress background from photoproduction, as described in section 5.4.
- The BPC hit must be closer than  $60 \text{ cm}$  to the beam pipe and the  $\theta$  angle of the BPC hit smaller than  $172.5^\circ$ . This corresponds to a scattering angle ( $\theta_{scel}$ ) of the electron between  $172.5^\circ$  and  $157^\circ$  when the collision occurs at the nominal  $ep$  interaction point.

As mentioned before, the high  $Q^2$  sample consists of events with the scattered electron detected in the LAr calorimeter. The electromagnetic cluster with the largest transverse energy is accepted as the scattered electron if it fulfills the following additional criteria:

- $Q^2$  must be greater than  $110 \text{ GeV}^2$ .
- The scattering angle of the electron cluster is required to be between  $10^\circ$  and  $150^\circ$  in order for the cluster to be fully contained in the LAr calorimeter and to avoid the transition region between the LAr and BEMC.
- The electron must be isolated, i.e. the energy deposited in the electromagnetic section must be less than  $1.2 \text{ GeV}$  within a cylinder of radius between  $15$  and  $30 \text{ cm}$  around the electron direction, and in the hadronic section it must be less than  $0.5 \text{ GeV}$  within  $30 \text{ cm}$  around the electron direction.
- The center of gravity of the electron cluster must be at least  $2 \text{ cm}$  away from acceptance holes in the  $\phi$  coverage of the LAr calorimeter.

- The Bjorken  $y$  of the scattered electron must be less than 0.6. This rejects photo-production events.

The following additional requirements are common to both samples.

- The position of the primary vertex must be between  $-25$  and  $35$  *cm* of the nominal *ep* interaction point.
- There has to be at least one track fulfilling the track selection criteria described in section 5.5.
- To exclude rapidity gap events, the sum of the calorimetric energy  $E_F$  in the forward region ( $4.4^\circ < \theta < 15^\circ$ ) has to be greater than  $0.5$  *GeV* [24], i.e there must be some activity in the forward region of the detector.
- To avoid proton beam induced background events entering the detector from outside, there should be no veto from the veto wall.
- No coherent noise in the Liquid Argon calorimeter.
- The invariant mass squared of the hadronic system  $W^2$  must be greater than  $7225$  *GeV*<sup>2</sup> (or  $W > 85$  *GeV*), corresponding to  $y \gtrsim 0.08$ .
- To use only events with a 'good'  $y$  reconstruction, both  $y_{el}$  and  $y_{da}$  are required to be greater than 0.08

The rapidity gap events are presumed to stem from diffractive-like processes [25]. Since these processes are not included in the standard QCD models used in this analysis, the rapidity gap events have been removed from the sample.

The final low  $Q^2$  sample contains 5644 DIS events with an average  $Q^2$  of  $24$  *GeV*<sup>2</sup> and within an  $x$ -range from  $2.6 \cdot 10^{-4}$  to  $10^{-2}$ . The final high  $Q^2$  sample contains 476 DIS events with an average  $Q^2$  of  $483$  *GeV*<sup>2</sup> and distributed over an  $x$ -range of  $2.6 \cdot 10^{-3}$  to  $2.9 \cdot 10^{-1}$ . The kinematic region covered after applying the event selection procedure described above, is shown in figure 5.4.

In the following, data events passing the above selection cuts will be referred to as selected data events while reconstructed Monte Carlo events will be referred to as selected Monte Carlo events. When referring to all selected data events it will be called the final data sample.

## 5.4 Background Events

The most important limitation in extending the measurement towards high  $y$  ( $y > 0.5$  in the low and  $y > 0.6$  in the high  $Q^2$  sample <sup>4</sup>) comes from the background of photoproduction processes. These are *ep* collisions at  $Q^2 \approx 0$ , which outnumber the DIS collision rate by several orders of magnitude. In these collisions the electron is scattered at small angles and is not observed in the BEMC or the LAr. However, hadrons produced in these collisions may give rise to a signal in the BEMC or the LAr, which could be misidentified

---

<sup>4</sup>This corresponds to  $W > 210$  and  $230$  *GeV* respectively.

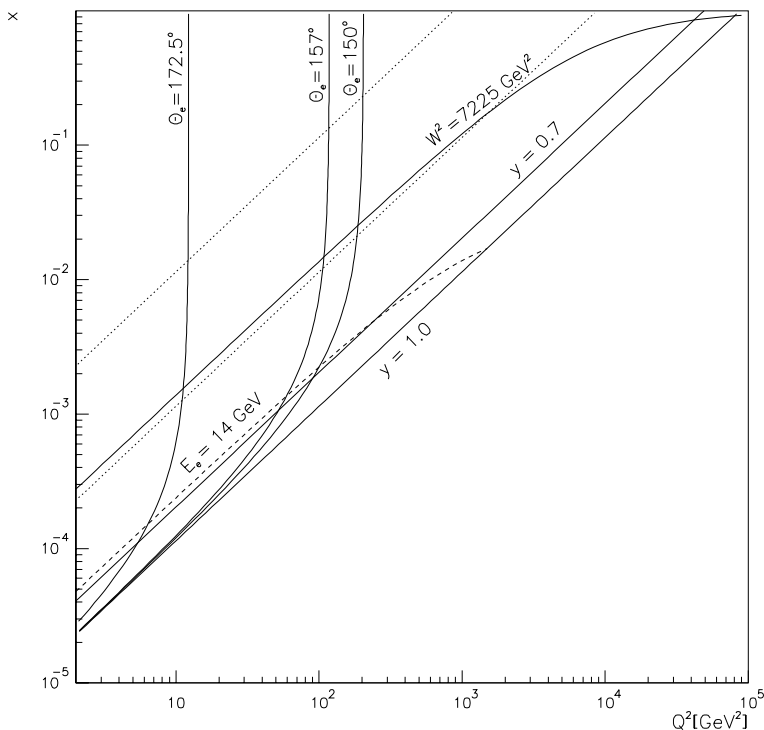


Figure 5.4: *The kinematic region covered after applying the event selection procedure. The region between  $150^\circ < \theta_{scel} < 157^\circ$  where the scattered electron is not measured, divides the kinematic plane into a high and a low  $Q^2$  region.*

as that of a DIS electron. In order to remove the photoproduction events from the low  $Q^2$  event sample, the scattered electron cluster in the BEMC is required to have a radius that is less than  $5\text{ cm}$  and an energy that is greater than  $14\text{ GeV}$ . This corresponds to  $y \lesssim 0.5$ . Such a hard cut in  $y$  is not necessary for the high  $Q^2$  event sample. A cut of  $y < 0.6$  is sufficient. Monte Carlo studies show that the background from photoproduction in the final data sample is negligible.

Sometimes the incoming electron has radiated photons, thereby reducing its energy, before it interacts with the proton. These events are called QED radiative events. The kinematic variables in these types of events are systematically reconstructed in the wrong way, which means that events may end up in the wrong  $(Q^2, W)$  bin. In addition the boost to the hadronic  $cms$  will be wrong. The QED radiative events occur mainly at high  $y$  values. The event selection described above removes most of them. The effect of the remaining QED radiative events in the final data sample has been investigated by using the Monte Carlo generator Django [26] which simulates these types of events. In figure 5.5 the transverse energy flow in the hadronic  $cms$  is shown in the range  $10 < Q^2 < 110\text{ GeV}^2$  and  $W > 85\text{ GeV}$  for MC events with and without QCD-corrections which passed the event selection criteria. From this plot it can be seen that the effects of the QED radiative events on the transverse energy flow analysis is at most 5% but generally less. This is also the case for the multiplicity analysis. The effect is roughly the same in all  $(Q^2, W)$  bins. The measured distributions have not been corrected for QED radiative effects, instead the effects have been taken into account in the calculation of the systematic error.

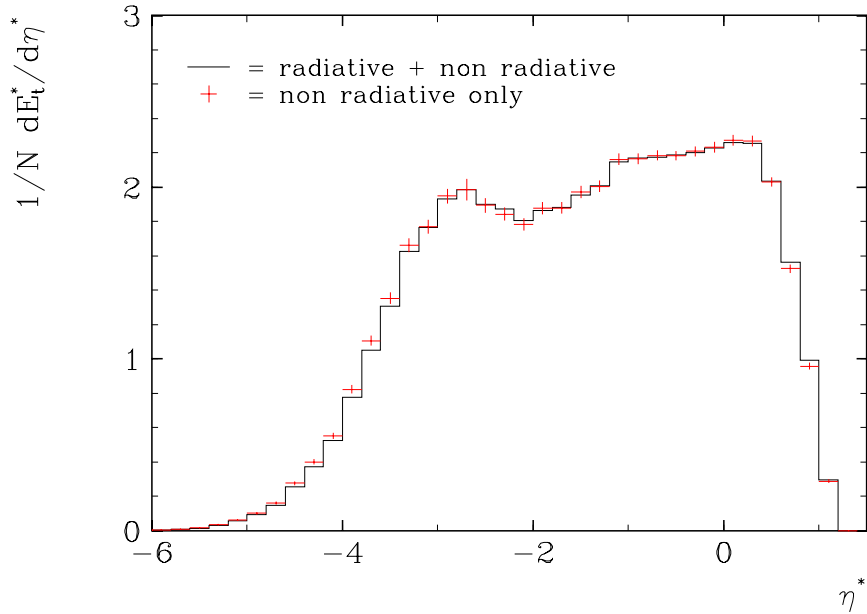


Figure 5.5: *The effects of radiative events on the transverse energy flow in the hadronic cms after applying angular cuts corresponding to the detector acceptance. The effect is greatest around  $-3.5$  in  $\eta^*$  ( $\sim 5\%$ ) but generally much lower.*

Although events with visible rapidity gaps are removed, there may still be diffractive events surviving the event selection. To estimate the amount of such events in the final data sample, the generator Rapgap [27] was used. This generator produces diffractive events, some of which survive the selection criteria used for the analysis. This study showed that about 8% of the events in the final data sample are of diffractive type. The effect of diffractive events is not taken into account in the correction of the data but is included into the systematic error.

As mentioned previously, the machine background from the beam wall and beam gas events is removed to a great extent by the on-line trigger. Off-line event classification and background rejection filters reduce the background further and, after applying the event selection described above, the background is negligible.

## 5.5 Selection of Tracks and Clusters

The hadronic energy is measured using the calorimeter clusters in the polar range  $4.4^\circ$  to  $174^\circ$ . Clusters are formed by adding up the energy in the calorimeter cells (which are corrected for dead material, i.e. non-sensitive material). The clustering procedure starts with an initiating cell with an energy at least 4 sigma above the noise level and continues with all neighboring cells deviating more than 2.3 sigma from the online threshold, as described in ref [28]. A full account of the energy measurement in H1 can be found in [16] showing, that the analysis results do not depend on details in the reconstruction method.

In this study only tracks originating from the primary vertex are of interest. In order to avoid tracks from secondary vertices and tracks that, for different reasons, are

wrongly reconstructed, some sort of selection procedure must be performed. This is done by imposing different requirements on the tracks. The tracks are built out of the hits generated by a charged particle traversing the tracking system. The track reconstruction starts by finding track elements defined by the hits in each drift cell, continues with merging the track elements in nearby cells to track segments and ends with linking the track segments in the different chambers to form the final tracks. A complete description of the track reconstruction in the H1 detector can be found in [16].

Tracks detected in the FTS will be referred to as forward tracks and tracks detected in the CTS will be referred to as central tracks. Since the FTS or CTS are different detectors, forward and central tracks have to fulfill different selection criteria. Tracks giving rise to track segments in both the FTS and the CTS will be treated as forward tracks

In the charged particle analysis, the forward and central tracks coming from the primary vertex which meet the following criteria are used <sup>5</sup>:

Forward tracks:

- The track has to have a polar angle between  $10^\circ$  and  $22^\circ$ . These limits are determined by the track reconstruction efficiency.
- The momentum of the track has to be greater than  $0.6 \text{ GeV}$  but less than  $30 \text{ GeV}$ . The upper cut removes tracks with large uncertainties in the reconstructed momentum.
- The distance ( $R_0$ ) in the  $xy$  plane between the track and the vertex, must be less than  $5 \text{ cm}$ .
- The  $\chi^2$  of the vertex fit of the track has to be less than 20. This requirement, together with the above  $R_0$  cut, will suppress tracks originating from secondary vertices.
- The  $\chi^2$  of the track fit to the hits in the detector *divided* by the number of degrees of freedom, must be less than 10. This will remove tracks with enough bad hits to make their parameters unreliable.

Central tracks:

- The tracks must have polar angles between  $22^\circ$  and  $158^\circ$ . These limits are given by the track reconstruction efficiency.
- The transverse momentum,  $P_T$  of the track has to be greater than  $0.15 \text{ GeV}$  but less than  $10 \text{ GeV}$ . The upper cut removes tracks with large uncertainties in the reconstructed momentum.
- The track must consist of at least four hits in the CJC.

Azimuthal inefficiencies in the chambers are taken into account in the simulation.

---

<sup>5</sup>The track selection of the forward tracks is described in detail in appendix G.

## 5.6 Binning of the Events

As was mentioned before, the dependence of the multiplicity and the transverse energy flow on  $Q^2$  at fixed  $W$  and on  $W^2$  at fixed  $Q^2$  is to be measured in this study. In order to minimize the influence of any  $W$  dependence in the  $Q^2$  measurement and any  $Q^2$  dependence in the  $W$  measurement via equation 2.4, the total  $W$  range has been divided into three intervals and the  $Q^2$  range into four intervals. These intervals were chosen in such a way that each of them should contain roughly the same amount of accepted data events. Table 5.1 gives the number of events in each  $(Q^2, W)$  interval for the final data sample.

$Q^2$ [ $GeV^2$ ] $\rightarrow$	10 – 15	15 – 26	26 – 110	> 110
$\downarrow$ $W$ [ $GeV$ ]				
85 – 123	518	637	640	76
123 – 162	757	598	626	132
> 162	679	647	542	268

Table 5.1: Number of events in each  $(Q^2, W)$  bin for the final data sample. In total 6120 events collected in the H1 detector were used in the analysis.

In order to estimate the migration between the different bins for a data sample that has passed the event selection criteria (described in section 5.3), a Monte Carlo study was performed, using events that had been detector simulated, reconstructed and in addition had fulfilled the event selection criteria. The migration is determined by calculating the fraction of the events reconstructed in one particular  $Q^2, W$  interval which were actually generated in an adjacent interval. The results are shown in tables 5.2 and 5.3.

$Q^2_{generated}$ [ $GeV^2$ ] $\rightarrow$	< 10	10 – 15	15 – 26	26 – 110	> 110
$\downarrow$ $Q^2_{reconstructed}$ [ $GeV^2$ ]					
10 – 15	0.06	0.90	0.04		
15 – 26		0.04	0.94	0.02	
26 – 110			0.03	0.95	0.02
> 110				0.01	0.99

Table 5.2: Fraction of the events reconstructed in the  $i$ :th  $Q^2$  interval which were generated in the  $j$ :th interval. It can be seen for example that 5% of the events reconstructed in the  $Q^2$  interval 26 – 110  $GeV^2$  were generated in adjacent intervals, i.e. there is a 5% contamination in the 26 – 110 interval.

From table 5.2 it can be seen that the migration between different  $Q^2$  bins is small. For example 94% of the events reconstructed in the  $Q^2$  interval 15-26  $GeV^2$  were generated in that particular interval and only 6% in the adjacent ones.

The migration between different  $W$  bins is, however, larger. This is expected from the longer tails in the distribution of the relative error in the  $W$  reconstruction (see figure 5.2). For example 15% of the events reconstructed in the  $W$  interval 85–123  $GeV$  were actually generated in the adjacent  $W$  intervals. To conclude, the migration is small enough for the migration effects to be corrected for in the correction procedure.

$W_{generated} [GeV] \rightarrow$	< 85	85 – 123	123 – 162	> 162
$\downarrow W_{reconstructed} [GeV]$				
85 – 123	0.07	0.85	0.08	
123 – 162		0.14	0.80	0.06
> 162			0.08	0.92

Table 5.3: *Fraction of the events reconstructed in the  $i$ :th  $W$  interval which were generated in the  $j$ :th interval.*

Since the  $Q^2$  and  $W$  are related through equation 2.4 and the dependence of the multiplicity and the transverse energy flow on  $Q^2$  and  $W$  is to be measured separately, the  $\langle Q^2 \rangle$  should not change too much with  $W$  and vice versa. In table 5.4 the average  $Q^2$  and  $W$  in each  $(Q^2, W)$  bin in the final data sample is shown. The change in the average  $W$  with  $Q^2$  is small. This indicates that there is only a small influence from  $Q^2$  on  $\langle W \rangle$ . The average  $Q^2$  is also quite independent of  $W$  except for the highest  $Q^2$  bin. From the above it can be concluded that the dependence of the multiplicity and the transverse energy flow on  $Q^2$  for fixed  $W$  is not affected, whereas there may be some effects on the dependence on  $W$  for fixed  $Q^2$  in the last  $Q^2$  bin. However, as will be shown later, the dependence of the  $\langle n_{ch} \rangle$  and the  $\langle E_t^* \rangle$  on  $W$  is more pronounced than on  $Q^2$  and therefore the dominant effect must come from the  $W$  dependence.

$W [GeV] \rightarrow$	85 – 123		123 – 162		> 162	
$\downarrow Q^2 [GeV^2]$	$\langle Q^2 \rangle$	$\langle W \rangle$	$\langle Q^2 \rangle$	$\langle W \rangle$	$\langle Q^2 \rangle$	$\langle W \rangle$
10 – 15	12.64	107.73	12.21	143.07	12.22	182.66
15 – 26	19.60	105.78	19.46	142.01	19.50	183.01
26 – 110	46.31	105.22	43.32	142.84	39.88	183.94
> 110	551.66	108.25	516.10	144.30	447.44	197.45

Table 5.4: *The average value of the kinematic variables  $Q^2$  and  $W$  in each  $(Q^2, W)$  bin for the final data sample.*

## 5.7 Corrections

To be able to compare data with Monte Carlo predictions at the parton level, the data has to be corrected for detector effects. The corrections are made by applying bin-by-bin correction factors. Each distribution is produced three times: from the data ( $d_{measured}^{data}$ ), from Monte Carlo events at the generator level ( $d_{generated}^{mc}$ ) and from reconstructed Monte Carlo events ( $d_{reconstructed}^{mc}$ ). The correction function, which should be applied to the data, is defined as the ratio of  $d_{generated}^{mc}$  and  $d_{reconstructed}^{mc}$ . The corrected distribution ( $d_{corrected}^{data}$ ) is thus given by

$$d_{corrected}^{data} = d_{measured}^{data} \cdot \frac{d_{generated}^{mc}}{d_{reconstructed}^{mc}} \quad (5.1)$$

The distributions at the parton level are determined for events satisfying the physics selection criteria. For low  $Q^2$  events ( $Q^2 < 110 \text{ GeV}^2$ ) these criteria are  $E'_e > 14 \text{ GeV}^2$ ,  $157^\circ < \theta_{scel} < 172.5^\circ$ , for high  $Q^2$  events ( $Q^2 > 110 \text{ GeV}^2$ ),  $y < 0.6$ ,  $10^\circ < \theta_{scel} < 150^\circ$ , and for both high and low  $Q^2$  events,  $W > 85 \text{ GeV}$ ,  $E_F(4.4^\circ < \theta < 15^\circ) > 0.5 \text{ GeV}$ . Charged particles used in the multiplicity analysis, have to be within the tracker acceptance ( $10^\circ \leq \theta \leq 158^\circ$ ) and particles used in the transverse energy flow analysis, have to be fully contained within the calorimeter ( $4.4^\circ \leq \theta \leq 174^\circ$ ). Corrections for particles outside these acceptances are not applied.

With the above procedure, the corrected data can be compared with Monte Carlo DIS events satisfying the physics selection criteria described above. The correction has been determined using the Ariadne program, since the uncorrected data distributions are best described by this generator.

The following discussion of corrections and uncertainties in the transverse energy flow is exemplified by the correction functions given in figure 5.6. Similar considerations are valid for all the transverse energy flow distributions.

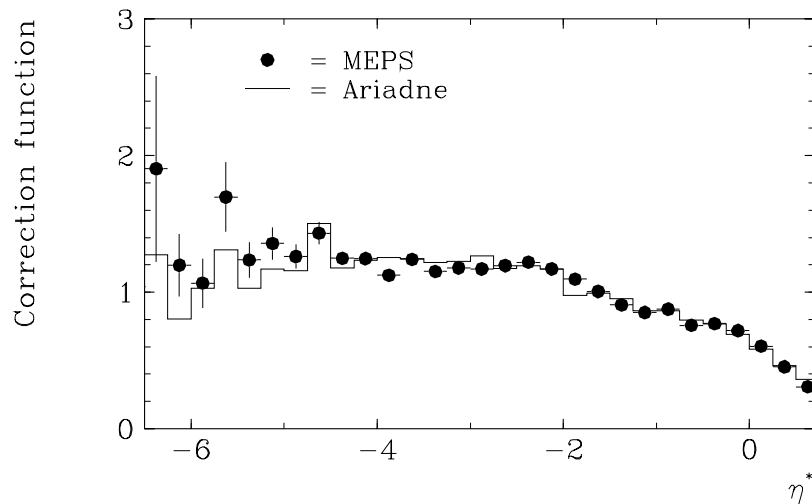


Figure 5.6: The correction function ( $d_{generated}^{mc}/d_{reconstructed}^{mc}$ ) for the transverse energy flow in the hadronic center of mass system for the  $Q^2, W$  range 15-26  $\text{GeV}^2$ , 85-123  $\text{GeV}$ .

The full line in figure 5.6 is obtained using Ariadne while the dots are the result of using the MEPS model. As we can see, the corrections which have to be applied to the energy flow measurement come out very similar from both generators and differ by less than 10%. This is what one expected, since the result of the detector simulation should not depend on the Monte Carlo program used to generate the event. The correction function varies by 10% around the value 1.0 in the central region and increases to  $\approx 1.3$  in the backward region while it drops to  $\approx 0.4$  in the forward region. The decrease of the correction function in the forward region is due to secondary interactions in dead material in front of the calorimeter as well as calorimetric shower spread of particles traversing the calorimeter at angles smaller than  $4.4^\circ$ . The increase of the function in the backward region reflects the limited hadronic responses of the detectors involved. The large statistical uncertainties for the  $\eta^* < -5$  are due to the few particles produced in this region.

An example of correction functions for the charged particle flow is shown in figure 5.7. The distribution is rather flat with two different levels for the central and forward tracks. The central region has a value of  $\approx 1.2$  and the forward region a value of  $\approx 1.4$ . This discrepancy in the correction values reflects the difference in efficiency in the central and forward tracker. The correction values are mainly due to well understood chamber inefficiencies. The bump at  $\eta^* = -1.0$  is due to low efficiency in the transition region between the forward and central tracking systems ( $\approx 20^\circ - 30^\circ$ ). For  $\eta^* < -5$  the statistical uncertainties becomes large by the same reason as described in the case of the energy flow. The difference between MEPS and Ariadne is less than 9%.

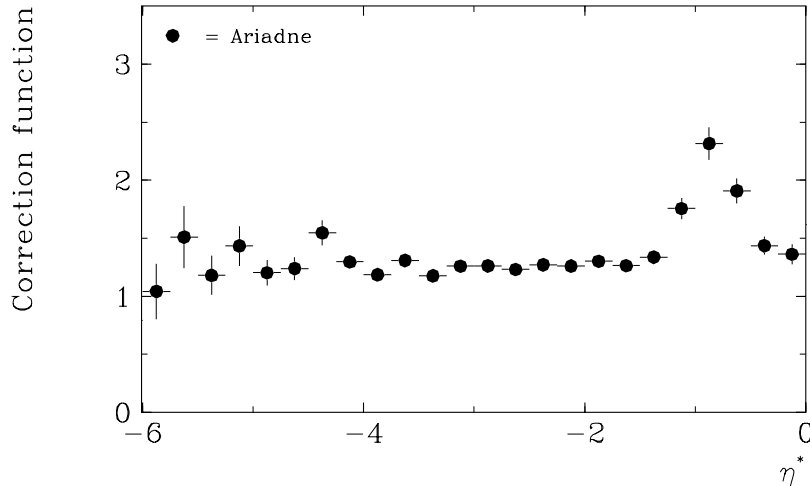


Figure 5.7: The correction function ( $d_{generated}^{mc}/d_{reconstructed}^{mc}$ ) for the charged particle flow in the hadronic center of mass system for the  $Q^2, W$  range  $15-26 \text{ GeV}^2, > 162 \text{ GeV}$ .

## 5.8 Systematic errors

The estimated average systematic uncertainties in the transverse energy and charged particle flow measurements are summarized in table 5.5.

Two different shower models describing the hadronic cascade in the detector are GHEISHA and FLUKA. The difference between using GHEISHA or FLUKA in the detector simulation is less than 5% [24].

The parton density function used in this study is *MRS H* [29]. This parameterization is based on measurements made at HERA during 1992, in addition to other experimental measurements, and assumes that the gluon density increases as  $x^{-0.5}$  in the unmeasured low  $x$ -region. The parton density function *MRS D<sup>-</sup>*, being an older parameterization than *MRS H*, does not include the 1992 HERA results. However, it is based on the same assumptions regarding the gluon density at small  $x$  as *MRS H*. The *MRS D<sup>0</sup>* parameterization assumes a constant gluon density in the low  $x$ -region and gives therefore a parton density function that is flatter than *MRS D<sup>-</sup>*. The difference between using the steeper density function *MRS D<sup>-</sup>* or the flatter *MRS D<sup>0</sup>* compared to using the *MRS H* function was found to be less than 3% [24].

Source	Contribution [%]	
	Energy flow	Particle flow
Cascade model GHEISHA/FLUKA:	5 (5)	-
Parton density function:	3 (3)	3 (3)
Diffractive events:	5 (3)	5 (3)
QED Radiative corrections:	5 (2)	6 (5)
Correction function Ariadne/MEPS:	9 (5)	10 (6)
Total systematic error:	12.8 (8.5)	13.0 (8.9)

Table 5.5: *The systematic uncertainties of the energy and particle flow measurements. The values within parenthesis are used for the mean particle and mean transverse energy flow.*

The effects of the QED radiative events was studied using the Monte Carlo generator Django and was found to be less than 5% (6%) in the transverse energy (charged particle) flow analysis.

The uncertainties from diffractive events were estimated by comparing the correction functions obtained using Ariadne and Rapgap and was found to be less than 5%.

In the previous section it was shown that the correction functions only weakly depends on the choice of the QCD model (Ariadne or MEPS) and that it was less than 10%. The systematic error in the correction values applied in the transverse energy flow measurement is therefore put at 9%. For the charged particle flow it is put at 10%.

The uncertainty in the hadronic energy scale is 6% and is not included in the error bars shown in any of the transverse energy flow distributions. The reason for this is that the scale uncertainty just moves the whole curve up or down. With a perfect calibration, only the errors mentioned would remain.



# Chapter 6

## Results

In this chapter the results of the transverse energy studies showing transverse energy flows and mean transverse energy as a function of  $W^2$  and  $Q^2$  are presented together with charged particle flows and mean multiplicity as a function of  $W^2$  and  $Q^2$ .

### 6.1 Energy Flow

#### 6.1.1 The Transverse Energy Flow

In the hadronic center of mass system the QPM 'current quark' direction coincides with the direction of the exchanged boson ( $-z^*$ ). Investigating the transverse energies in the hadronic *cms* allows a more direct observation of the QCD radiation since the transverse energies are not obscured by a boost to the laboratory system.

The corrected transverse energy flow,  $E_T^*$ , in the hadronic *cms* as a function of pseudorapidity,  $\eta^* = -\ln \tan \frac{\theta^*}{2}$  is presented in figure 6.1, 6.2 and 6.3 for different  $Q^2$ ,  $W$  ranges. The distributions are normalized to the number of events  $N$ . The values of the distributions are listed in appendix A table A.1 - A.3.

A comparison with the QPM suggests that the large fraction of the transverse energy is generated by the QCD radiation. The transverse energy in the forward region measured in data is clearly larger than what is generated in both the MEPS or PSWQ models. This is less evident for Ariadne. In the analysis of the H1 1992 data [24] one can see, although the error bars are large, that the data points in the forward region lie above any of the tested Monte Carlo models except possibly for Ariadne. This is consistent with the observation reported here.

In the lowest ( $W, Q^2$ ) bin ( $85 < W < 123$ ,  $10 < Q^2 < 15$ ) data exhibits a plateau (see figure 6.4) in the current hemisphere,  $\eta^* < 0$ , which is more or less flat at  $E_T^* \approx 2 \text{ GeV}$  per unit of rapidity and extends from about  $\eta^* = 0$  to  $\eta^* = -3$ . The plateau becomes wider as  $W$  increases (most clearly seen in the  $Q^2$  range  $26 - 110 \text{ GeV}^2$ ) and moves upwards as  $Q^2$  increases to  $\approx 3 \text{ GeV}$  for  $Q^2 > 110 \text{ GeV}^2$ . The sharp drop in the transverse energy in the forward direction is due to acceptance effect.

In figure 6.1.a we see that at low  $Q^2$  the PSWQ model around  $\eta^* = -2$  produces slightly more transverse energy than the data, but less for  $\eta^* > -1$ . As  $Q^2$  increases more  $E_T^*$  is produced, and in the highest  $Q^2$  bin ( $Q^2 > 110 \text{ GeV}^2$ , see figure 6.1.d as an example) the PSWQ model generates in the central region about 50% more  $E_T^*$  than the data.

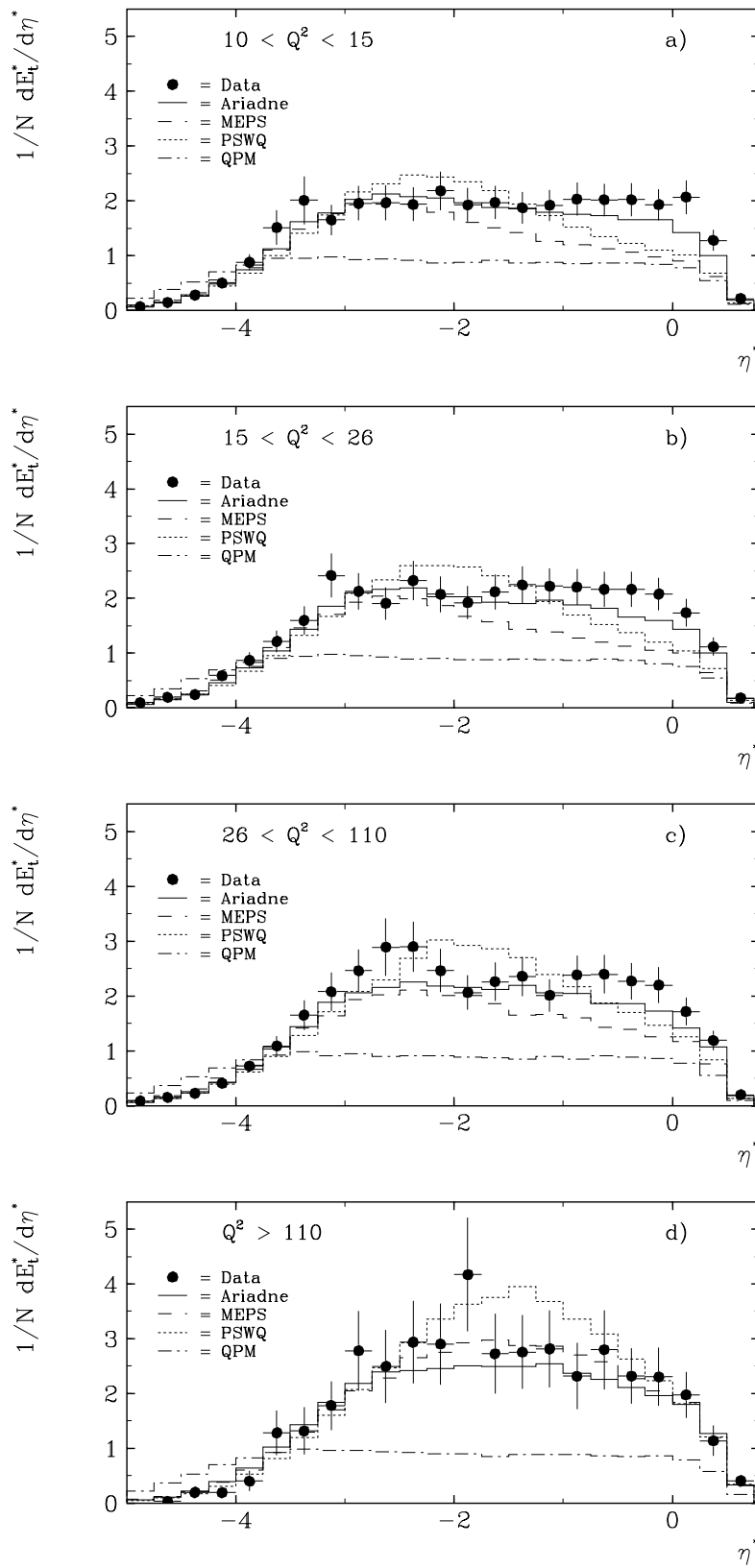


Figure 6.1: The corrected transverse energy flow  $E_T^*$  in the hadronic center of mass system as a function of pseudorapidity  $\eta^*$  for events in the  $W$  range 85 - 123 GeV in four different  $Q^2$  ranges. The proton direction is to the right. The error bars contain the statistical and systematic errors added in quadrature, except for an overall 6% energy scale uncertainty.

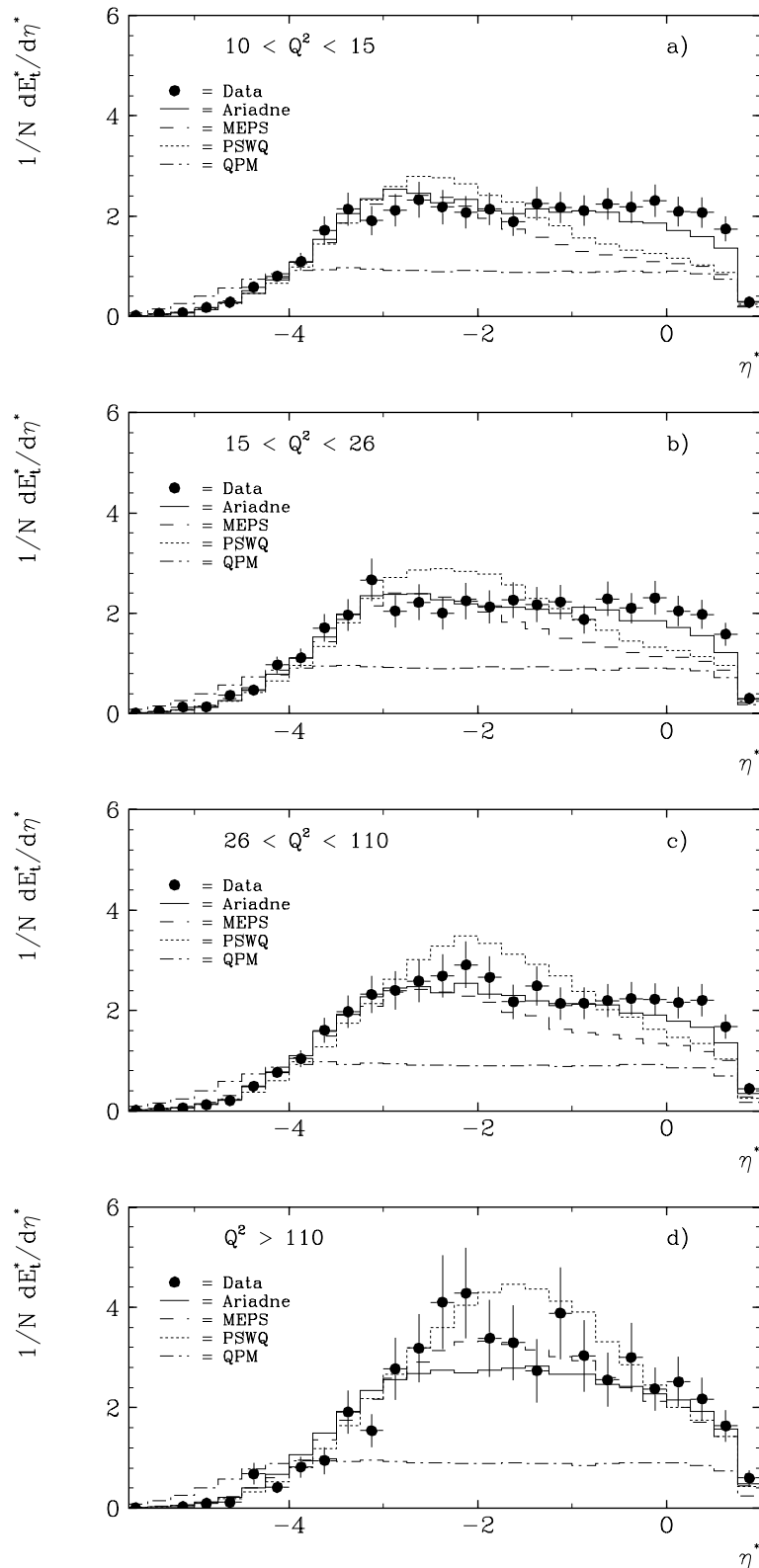


Figure 6.2: The corrected transverse energy flow  $E_T^*$  in the hadronic center of mass system as a function of pseudorapidity  $\eta^*$  for events in the  $W$  range 123 - 162 GeV in four different  $Q^2$  ranges. The proton direction is to the right. The error bars contain the statistical and systematic errors added in quadrature, except for an overall 6% energy scale uncertainty.

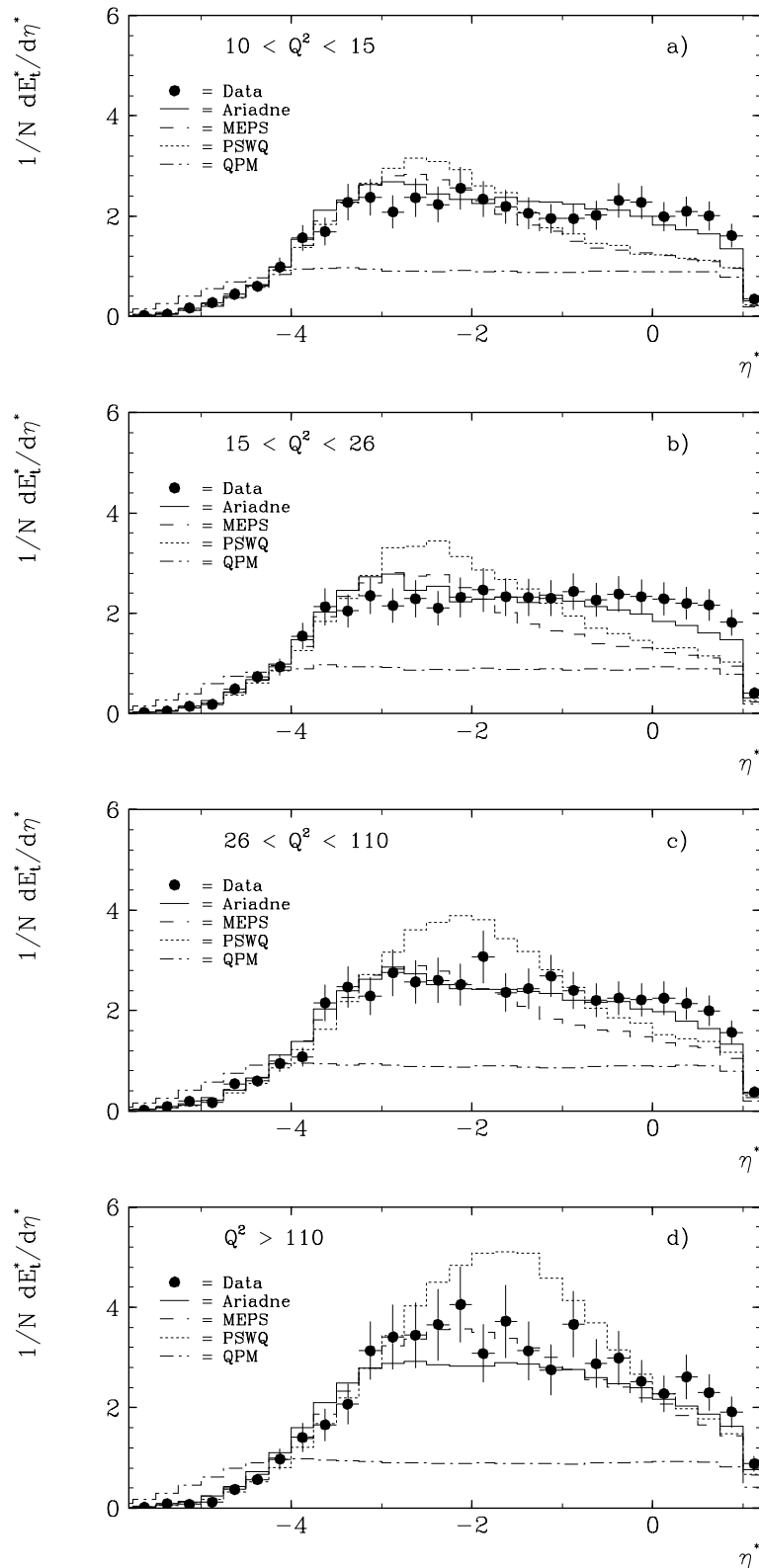


Figure 6.3: The corrected transverse energy flow  $E_T^*$  in the hadronic center of mass system as a function of pseudorapidity  $\eta^*$  for events with  $W > 162$  GeV in four different  $Q^2$  ranges. The proton direction is to the right. The error bars contain the statistical and systematic errors added in quadrature, except for an overall 6% energy scale uncertainty.

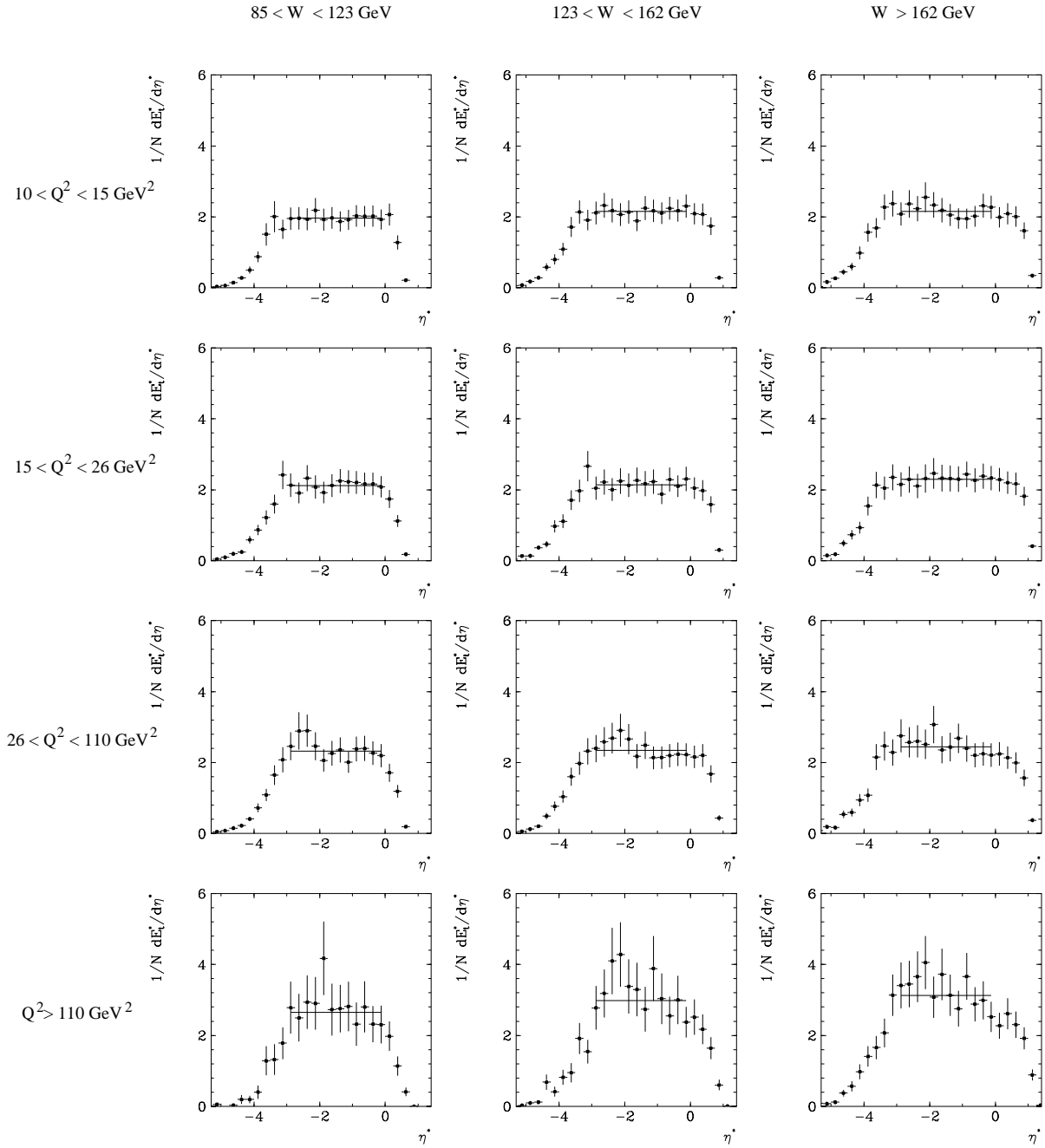


Figure 6.4: The corrected transverse energy flow  $E_T^*$  in the hadronic center of mass system as a function of pseudorapidity  $\eta^*$ . This figure contains the figure 6.1, 6.2 and 6.3 but now ordered in rows of  $Q^2$  and columns of  $W$  in order to illustrate how the plateau develops with  $Q^2$  and  $W$ . The dots are the data and the full line is a straight line fitted to the data in the pseudorapidity interval  $-3 \leq \eta^* \leq 0$  and gives the approximate height of the plateau.

However, in the forward region the PSWQ model follows the data. This behavior can be seen in all three  $W$  regions.

In all  $(W^2, Q^2)$  regions the MEPS model follows the data in the backward region up to about  $\eta^* = -2$ . For larger  $\eta^*$  the MEPS model produces about 30% less  $E_T^*$  than the data, except in the highest  $Q^2$  bin (figure 6.1.d, 6.2.d and 6.3.d) where it is very close to the data point and is actually the Monte Carlo model that reproduces the data best.

The Ariadne Monte Carlo program gives a reasonable description of data over the full  $\eta^*$  range for all  $(W^2, Q^2)$  bins.

## 6.1.2 Mean Transverse Energy

By measuring the mean transverse energy in the hadronic *cms*, an overall measure of the parton radiation activity is obtained. To find out if this parton radiation exhibits any dependence on  $W^2$  and/or  $Q^2$ , the mean transverse energy is measured in twelve  $(W^2, Q^2)$  intervals. Only energy deposited within the pseudorapidity range  $-5 < \eta^* < 0$  is used in the determination of the  $\langle E_T^* \rangle$ . Below  $\eta^* = -5$  the correction values have large errors and therefore become unreliable. Above  $\eta^* = 0$  detector acceptances become important.

In figure 6.5.a - 6.5.d the corrected mean transverse energy  $\langle E_T^* \rangle$  in the hadronic *cms* is shown as a function of  $W^2$  for the  $Q^2$  ranges 10-15, 15-26, 26-110 and  $Q^2 > 110$   $GeV^2$  respectively. The corrected  $\langle E_T^* \rangle$  as a function of  $Q^2$  is depicted in figure 6.6.a - 6.6.c for the  $W$  ranges 85 - 123, 123 - 162 and  $W > 162$   $GeV$  respectively. The corrected values of the  $\langle E_T^* \rangle$  are listed in table 6.4.

In figure 6.5 it can be seen that the mean transverse energy rises with increasing  $W^2$ , as expected from the increase of the phase space available for QCD radiation. A similar investigation of the  $\langle E_T^* \rangle$  dependence on  $W^2$  was performed using 1992 data [24]. The mean  $Q^2$  of the events used in this study was 25  $GeV^2$  and the  $\langle E_T^* \rangle$  was calculated based on the full available  $\eta^*$  range. However, limiting the pseudorapidity range for accepting clusters to  $-5 < \eta^* < 0$ , as was done in the present study, results in an  $\langle E_T^* \rangle$  which is about 11% less than an  $\langle E_T^* \rangle$  calculated without any cuts in the pseudorapidity range. This means that to be able to compare the absolute values of the data points presented in this thesis with the one obtained in 1992, the results in figure 6.5.b should be used (as the mean  $Q^2$  in this figure is the one closest to the mean  $Q^2$  of the 1992 data) and in addition the data points should be increased by about 11%. If this is done, one can see that the absolute values of the data point reported in [24] are compatible with those presented here.

Turning now to the Monte Carlo models it can be seen that the PSWQ model and Ariadne describe the data fairly well within error. The MEPS model systematically underestimates the  $\langle E_T^* \rangle$  for all  $Q^2$  values, which is a reflection of the underestimation of the  $E_T^*$  for  $\eta^*$  larger than -2.5 (see figure 6.1 - 6.3). A slight rise is also seen for the QPM.

In order to investigate the dependence of the  $\langle E_T^* \rangle$  on  $W^2$  (at fixed  $Q^2$ ) a  $\chi^2$  fit under the assumption of a constant energy flow, independent of  $W^2$ , is performed together with a fit using the function  $\langle E_T^* \rangle = a + b \cdot \ln W^2$ . The results, presented in table 6.1 show that a function with a logarithmic dependence on  $W^2$  gives a much better  $\chi^2/\text{NDF}$  than a constant function, independent of  $W^2$ . From this we can conclude that, at fixed  $Q^2$ , the observed  $W^2$  dependence of the  $\langle E_T^* \rangle$  is statistically significant and a  $\langle E_T^* \rangle$

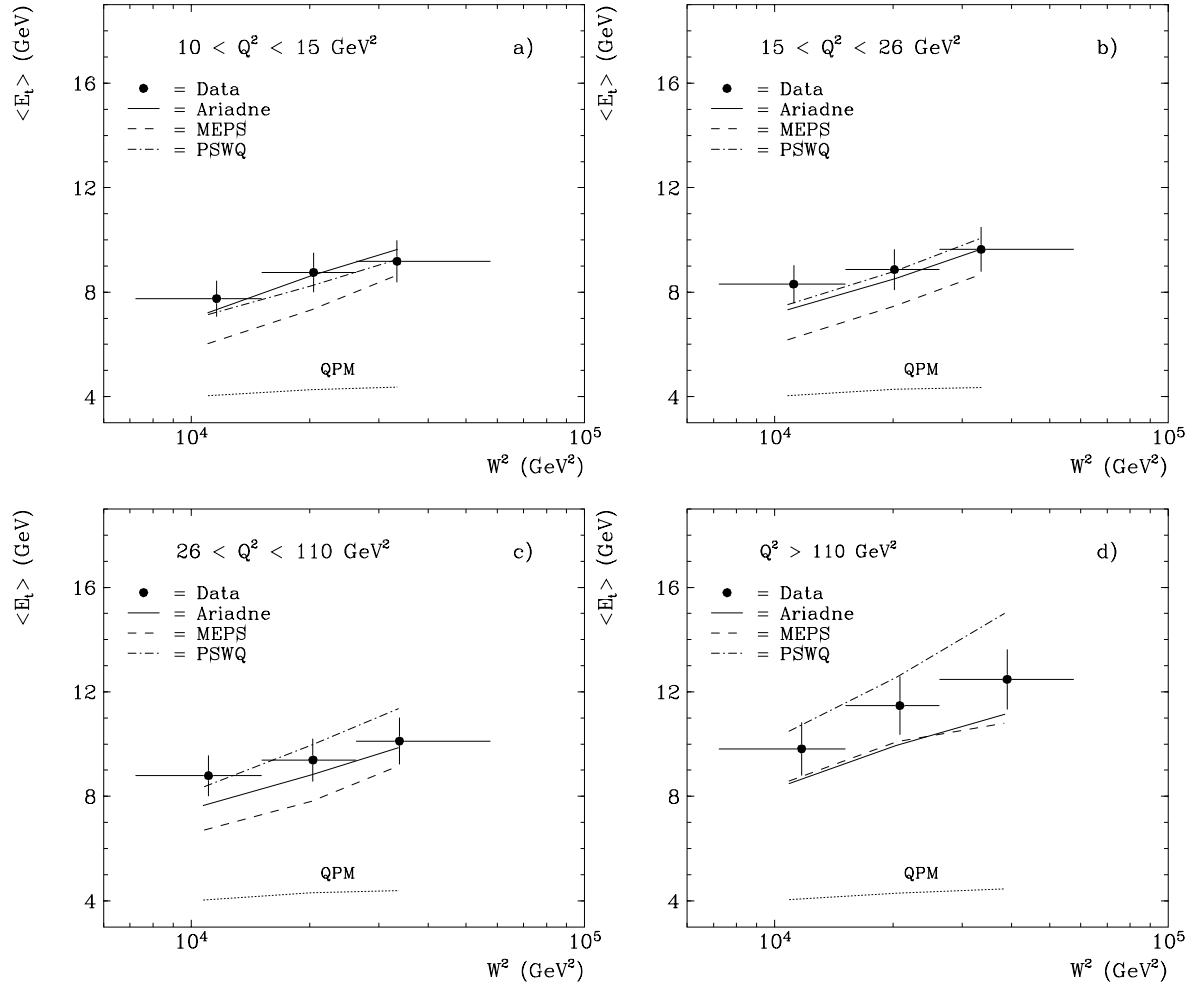


Figure 6.5: Mean transverse energy  $\langle E_T^* \rangle$  in the hadronic cms measured in the pseudorapidity range  $-5 \leq \eta^* \leq 0$  as a function of  $W^2$  in three different  $Q^2$  intervals. The error bars contain the statistical and systematic errors added in quadrature, except for an overall 6% energy scale uncertainty.

Fit based on data points in figure	Fitted function $\langle E_T^* \rangle = a$		Fitted function $\langle E_T^* \rangle = a + b \cdot \ln W^2$		
	$a$	$\chi^2/NDF$	$a$	$b$	$\chi^2/NDF$
6.5a	$8.61 \pm 0.11$	24.1/2	$-4.87 \pm 2.81$	$1.36 \pm .28$	1.1/1
6.5b	$8.80 \pm 0.12$	18.9/2	$-2.71 \pm 2.67$	$1.18 \pm .27$	0.37/1
6.5c	$9.39 \pm 0.13$	15.0/2	$-2.09 \pm 2.98$	$1.16 \pm .30$	0.22/1
6.5d	$11.49 \pm 0.30$	12.9/2	$-10.20 \pm 6.12$	$2.15 \pm .61$	0.32/1

Table 6.1: Results of fitting two different functions to the data points in figure 6.5.

independent of  $W^2$  is very unlikely.

In figure 6.6.a - 6.6.c a slight increase in  $\langle E_T^* \rangle$  with increasing  $Q^2$  can be observed. The PSWQ curve follows the data within errors for the low and medium  $W^2$  ranges, but

as  $W^2$  increases further, and especially for higher  $Q^2$ , the PSWQ model gives about 10% - 20% more  $\langle E_T^* \rangle$  than data. The slope of the PSWQ model is steeper than the slope of the data and this becomes more pronounced as  $W^2$  increases. Ariadne on the other hand has a slope for low  $W^2$  that is about the same as the data. At high  $W^2$ , however, the slope of Ariadne is slightly less than the slope of the data. The absolute values given by Ariadne are below data. The MEPS model is constantly below the data but moves closer as  $W^2$  increases. The QPM shows no  $Q^2$  dependence.

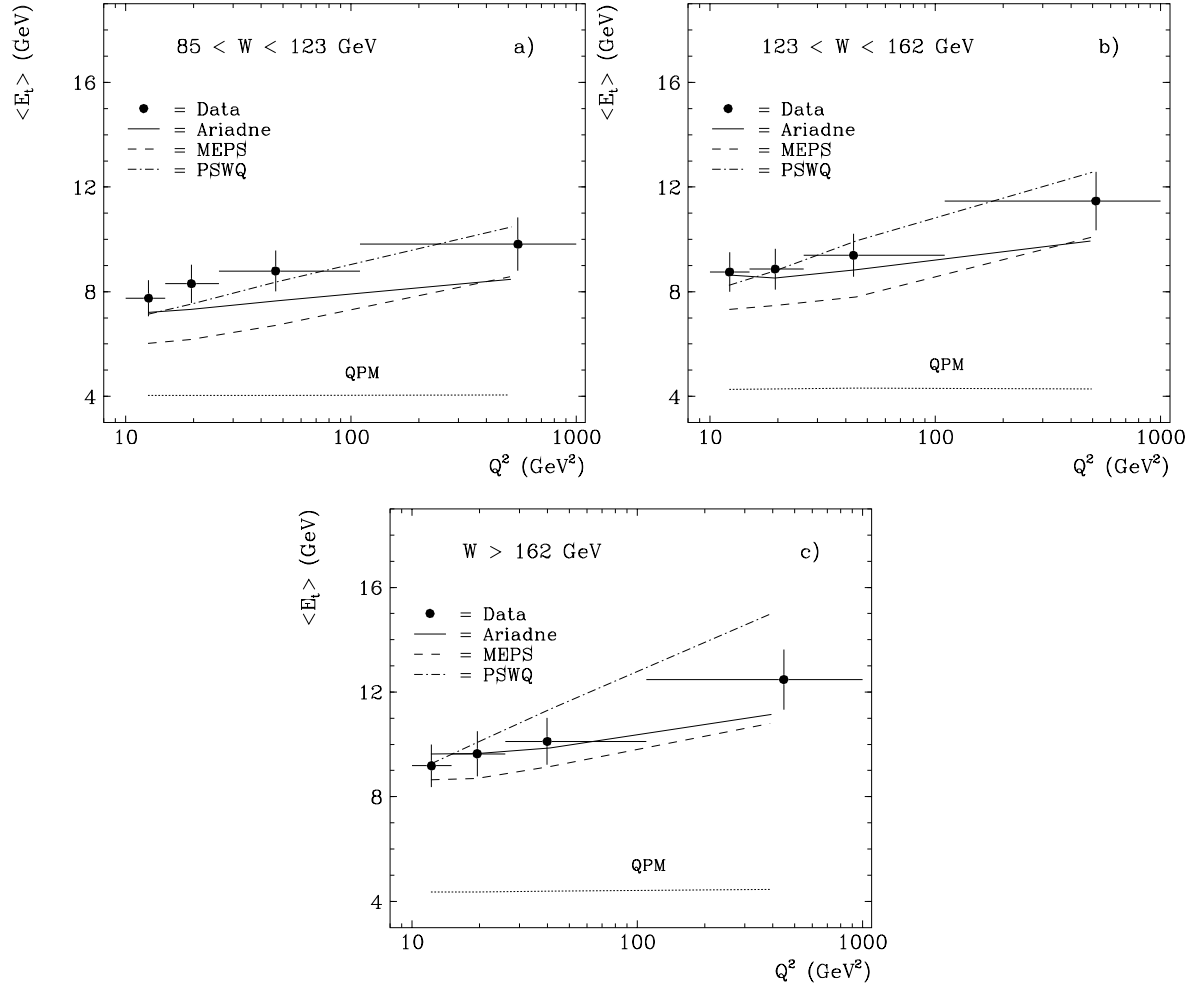


Figure 6.6: Mean transverse energy  $\langle E_T^* \rangle$  in the hadronic cms measured in the pseudorapidity range  $-5 \leq \eta^* \leq 0$  as a function of  $Q^2$  in three different  $W$  intervals. The error bars contain the statistical and systematic errors added in quadrature, except for an overall 6% energy scale uncertainty.

In order to determine if the observed increase in  $\langle E_T^* \rangle$  (at fixed  $W$ ) with increasing  $Q^2$  in figure 6.6.a - 6.6.c is a significant effect, a  $\chi^2$  fit of a function assuming no dependence on  $Q^2$  was compared to a fit with an logarithmic  $Q^2$  dependence. The results of the fits are given in table 6.2. From this we find that the  $\langle E_T^* \rangle$  depends to some extent on  $Q^2$  and that a logarithmic behavior with  $Q^2$  (at fixed  $W$ ) results in the best fit.

Fit based on data points in figure	Fitted function $\langle E_T^* \rangle = a$		Fitted function $\langle E_T^* \rangle = a + b \cdot \ln Q^2$		
	$a$	$\chi^2/NDF$	$a$	$b$	$\chi^2/NDF$
6.6a	$8.33 \pm 0.12$	17.6/3	$6.45 \pm 0.48$	$0.58 \pm .15$	1.6/2
6.6b	$9.06 \pm 0.11$	26.2/3	$6.99 \pm 0.43$	$0.66 \pm .13$	1.2/2
6.6c	$9.82 \pm 0.13$	46.4/3	$6.93 \pm 0.44$	$0.89 \pm .13$	0.3/2

Table 6.2: Results of fitting a constant function, independent of  $Q^2$ , and the logarithmic function  $\langle E_T^* \rangle = a + b \cdot \ln Q^2$  to the data points in figure 6.6.

A global fit to the data points was also performed, using the function 6.1<sup>1</sup>. The result is listed in table 6.3. Since most dependences in QCD are of the logarithmic kind, like the multiplicity [2] [4], it is reasonable to assume that the  $\langle E_T^* \rangle$  also has a logarithmic behavior, which explains why the logarithmic function 6.1 was chosen for the fit.

$$\langle E_T^* \rangle = \left[ a + b \cdot \ln \left( \frac{W^2}{W_0^2} \right) + c \cdot \ln \left( \frac{Q^2}{Q_0^2} \right) \right] \cdot W_0, \text{ where } W_0^2 = Q_0^2 = 1 \text{ GeV}^2 \quad (6.1)$$

Both parameters  $b$  and  $c$  are positive, i.e.  $\langle E_T^* \rangle$  increases with  $W^2$  and  $Q^2$ , and by comparing  $b$  and  $c$  we see that the dependence on  $W^2$  is about twice as large as the dependence on  $Q^2$ . The data points are well described by the function 6.1. The low  $\chi^2/NDF$  value might partly be due to some remaining correlation, through equation 2.4, between  $W^2$  and  $Q^2$  that was not removed by the event binning.

$a$	$b$	$c$	$\chi^2/NDF$
$-5.93 \pm 0.07$	$1.28 \pm 0.06$	$0.69 \pm 0.02$	3.85/9

Table 6.3: Fitted parameters  $a$ ,  $b$ ,  $c$  in the function 6.1 for the average transverse energy in the hadronic cms in the pseudorapidity interval  $-5 < \eta^* < 0$ .

To test the whether the  $\langle E_T^* \rangle$  can be described assuming only a  $W^2$  dependence, the function 6.1 is fitted with the parameter  $c$  fixed at zero. This gives a  $\chi^2/NDF$  of 48/10. The function 6.1 is also fitted with the parameter  $b$  fixed at zero, which tests the hypothesis that the  $\langle E_T^* \rangle$  depends only on  $Q^2$ . The  $\chi^2/NDF$  for this fit is 41/10. With such high  $\chi^2$  values these hypotheses can safely be rejected and a dependence on both  $W^2$  and  $Q^2$  is strongly favored.

From the above we conclude that the  $\langle E_T^* \rangle$  can only be described by a function containing both a  $\ln W^2$  and a  $\ln Q^2$  term. A function containing only one of these terms does not describe data.

<sup>1</sup>A function  $\langle E_T^* \rangle = a + b \cdot \sqrt{W^2} + c \cdot \sqrt{Q^2}$  was fitted as well but gave a factor two larger  $\chi^2$ .

$\langle W^2 \rangle [GeV^2]$	$\langle Q^2 \rangle [GeV^2]$	$\langle E_T^* \rangle [GeV]$
11605.67	12.64	$7.75 \pm .22 \pm .66$
11190.24	19.60	$8.30 \pm .18 \pm .71$
11071.30	46.31	$8.79 \pm .23 \pm .75$
11717.87	551.66	$9.81 \pm .59 \pm .83$
20468.56	12.21	$8.75 \pm .17 \pm .74$
20165.71	19.46	$8.86 \pm .20 \pm .75$
20403.33	43.32	$9.39 \pm .20 \pm .80$
20821.67	516.10	$11.47 \pm .55 \pm .97$
33364.10	12.22	$9.18 \pm .21 \pm .78$
33491.70	19.50	$9.64 \pm .25 \pm .82$
33835.36	39.88	$10.11 \pm .25 \pm .86$
38984.94	447.44	$12.48 \pm .45 \pm 1.06$

Table 6.4: Corrected values for the  $\langle E_T^* \rangle$  in the hadronic  $cms$  in the pseudorapidity range  $-5 \leq \eta^* \leq 0$  as a function of  $W^2$  and  $Q^2$ . The first error in the  $\langle E_T^* \rangle$  column is the statistical, the second the systematic; the overall error of 6% of the hadronic energy scale is not included.

## 6.2 Charged Multiplicity

### 6.2.1 Charged Particle Flow

The corrected charged multiplicity,  $n_{ch}$ , in the hadronic  $cms$  as a function of pseudorapidity  $\eta^*$  is presented in figure 6.7, 6.8 and 6.9 for different  $Q^2$ ,  $W$  ranges. The distributions are normalized to the number of events  $N$ . The values of the distributions are listed in appendix A table A.4 - A.6.

A comparison with the QPM shows that only about half of the multiplicity is accounted for in a model without QCD radiation.

In the current hemisphere,  $\eta^* < 0$ , a plateau which is more or less flat at  $n_{ch} \approx 2$  charged particles per unit can be observed. In the lowest ( $W, Q^2$ ) bin it extends from about  $\eta^* = -1$  to  $\eta^* = -3$ , becoming somewhat wider as  $W$  increases. The plateau does not exhibit any dependence on  $Q^2$ , in contrast to the transverse energy flow. The sharp drop in multiplicity in the forward direction is due to the detector acceptance.

In figure 6.7.b we see that at medium  $Q^2$  around  $\eta^* = -2$ , the PSWQ model produces slightly more particles than are observed in data. As  $Q^2$  increases more particles are produced, and in the highest  $Q^2$  bin ( $Q^2 > 110 GeV^2$ , see for example figure 6.7.d) the PSWQ model generates about 20-30% more charged particles in the central region than the data. This behavior can be seen in all three  $W$  regions, although it is most distinct for  $W > 164 GeV$ .

In all twelve ( $W^2, Q^2$ ) regions the MEPS model follows the data in the backward region up to about  $\eta^* = -2$ . For larger  $\eta^*$ , in the low and medium  $Q^2$  regions, the MEPS model produces about 20-30% less particles than observed in the data, which probably is related to the observed excess of  $E_T$  in data.

The Ariadne Monte Carlo program gives a reasonable description of data over the full  $\eta^*$  range for all ( $W^2, Q^2$ ) bins.

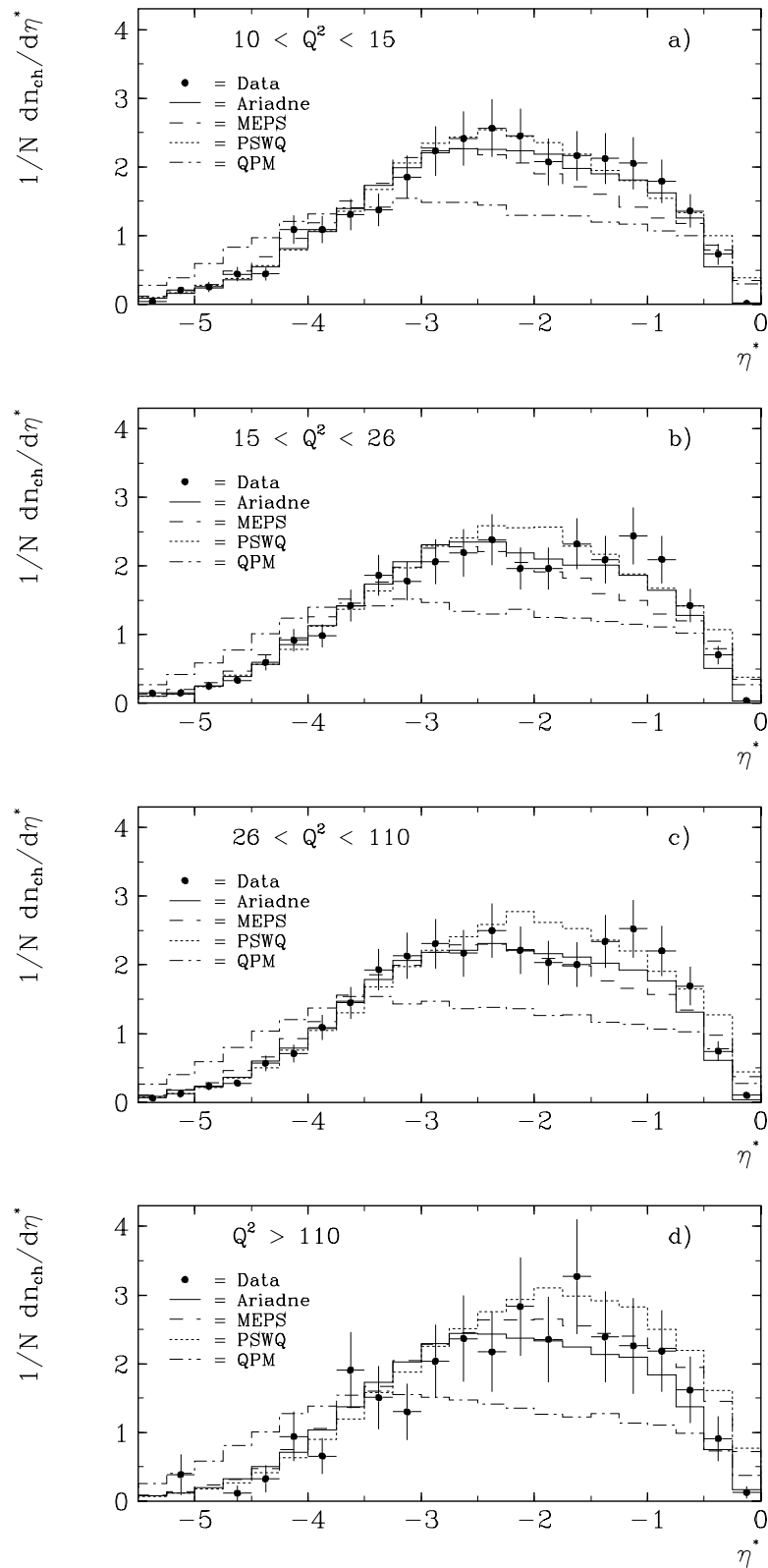


Figure 6.7: The corrected charged particle flow  $n_{ch}$  in the hadronic center of mass system as a function of pseudorapidity  $\eta^*$  for events in the  $W$  range 85 - 123 GeV in four different  $Q^2$  ranges. The proton direction is to the right. The error bars contain the statistical and systematic errors added in quadrature.

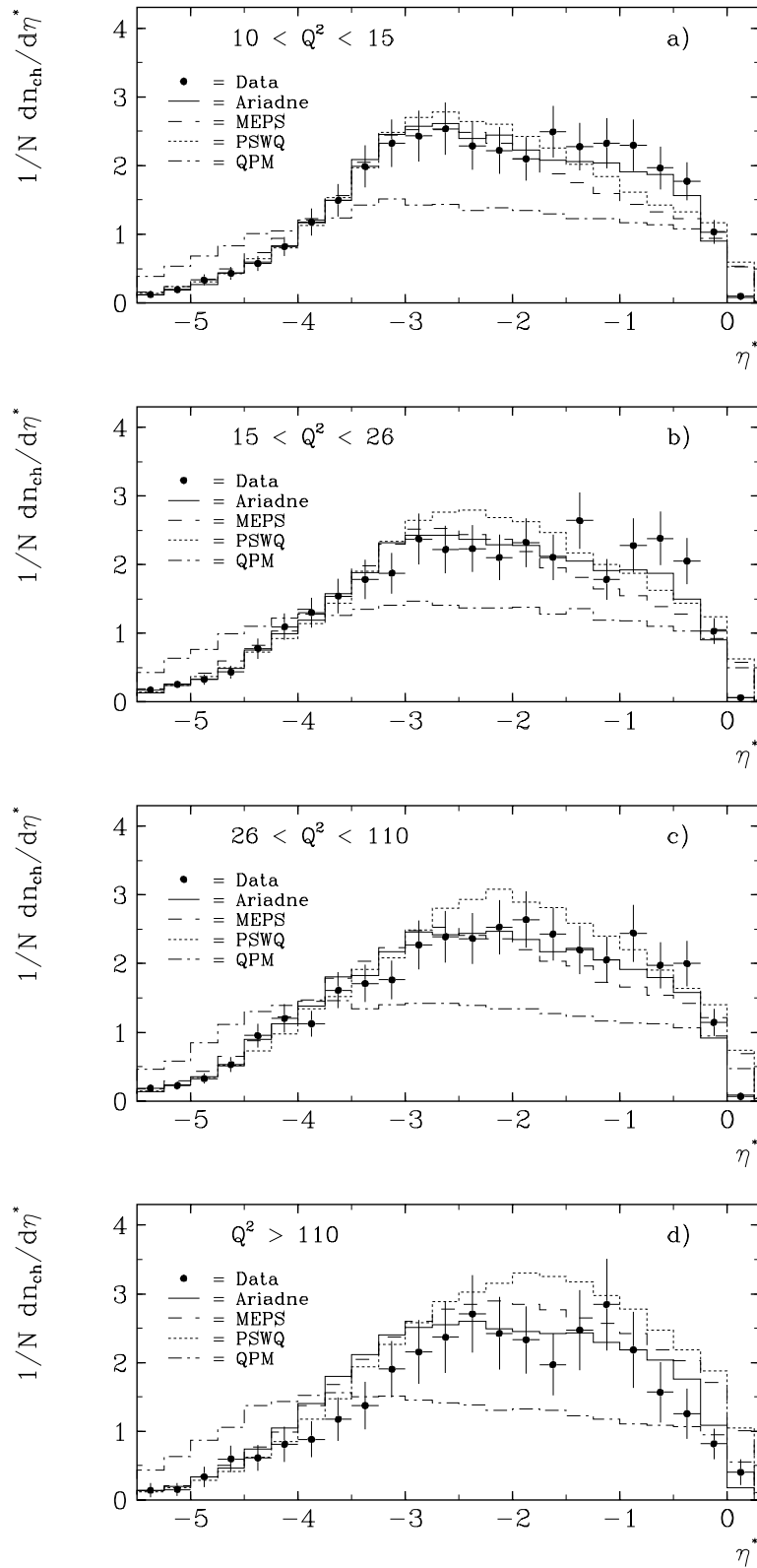


Figure 6.8: The corrected charged particle flow  $n_{ch}$  in the hadronic center of mass system as a function of pseudorapidity  $\eta^*$  for events in the  $W$  range 123 - 162 GeV in four different  $Q^2$  ranges. The proton direction is to the right. The error bars contain the statistical and systematic errors added in quadrature.

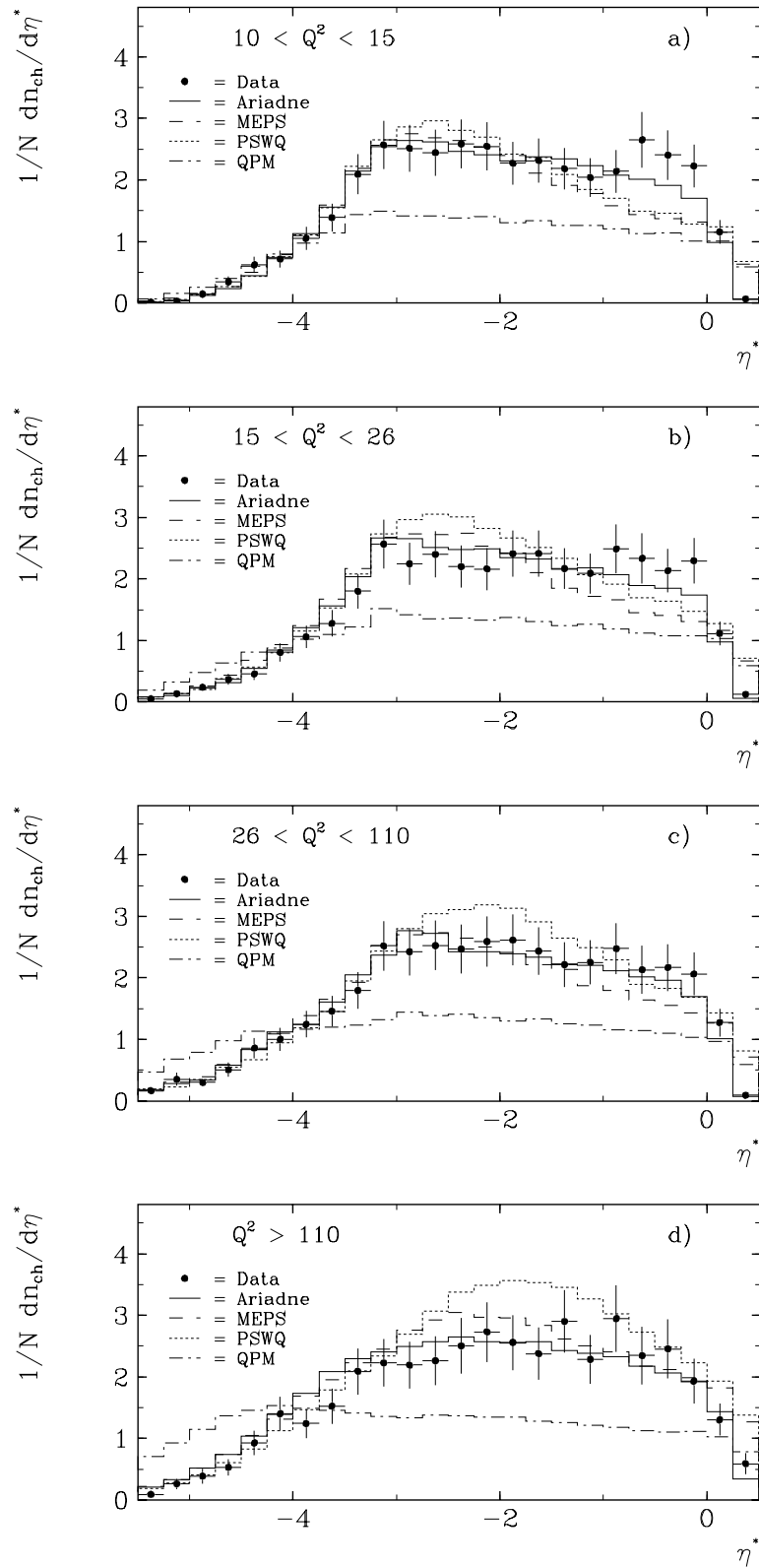


Figure 6.9: The corrected charged particle flow  $n_{ch}$  in the hadronic center of mass system as a function of pseudorapidity  $\eta^*$  for events with  $W > 162 \text{ GeV}$  in four different  $Q^2$  ranges. The proton direction is to the right. The error bars contain the statistical and systematic errors added in quadrature.

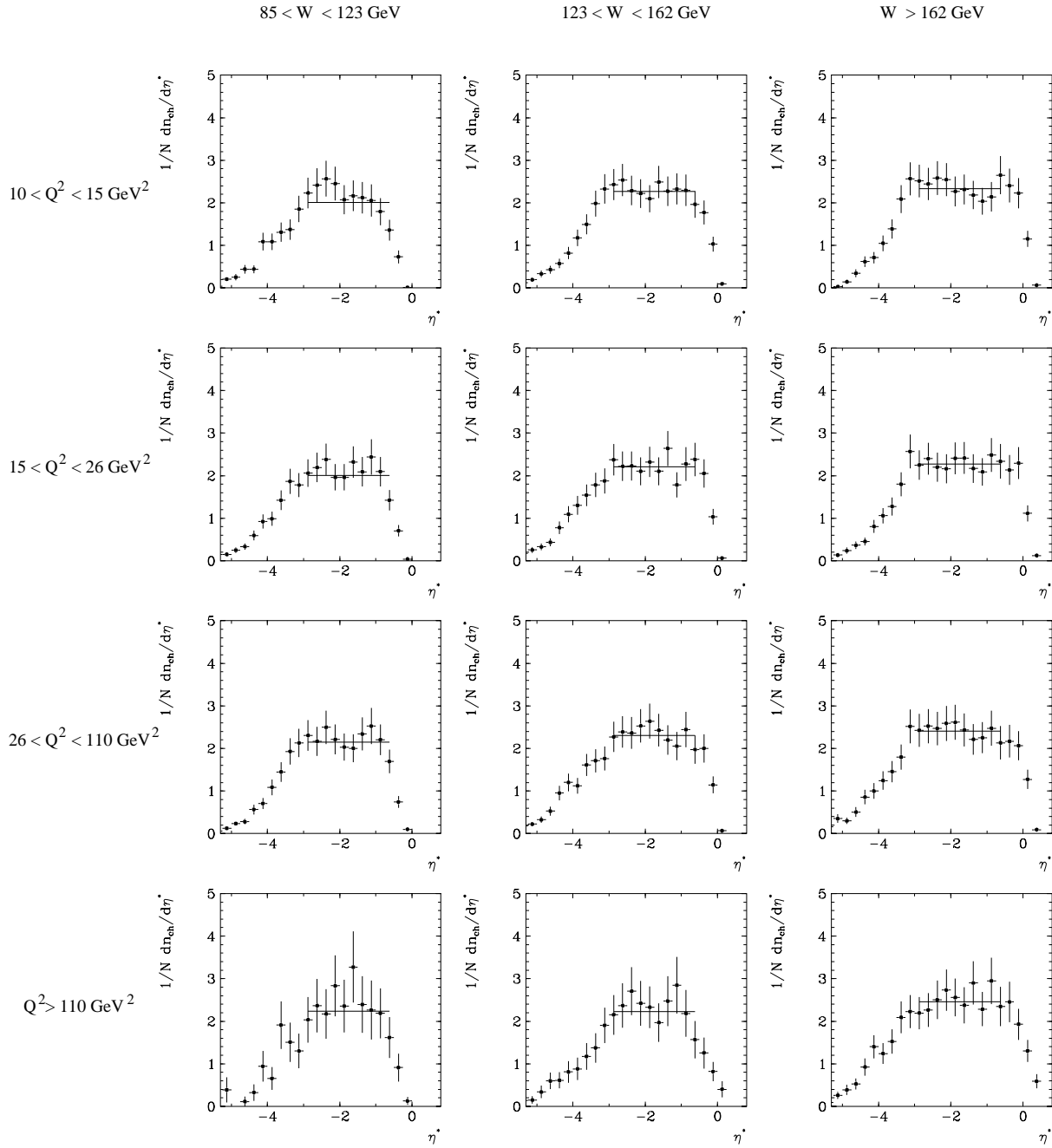


Figure 6.10: The corrected charged particle flow  $n_{ch}$  in the hadronic center of mass system as a function of pseudorapidity  $\eta^*$ . This figure contains the figure 6.7, 6.8 and 6.9 but now ordered in rows of  $Q^2$  and columns of  $W$ . This makes it possible to study development of the plateau with  $Q^2$  and  $W$ . The dots are the data and the full line is a straight line fitted to the data in the pseudorapidity interval  $-3 \leq \eta^* \leq -0.5$  and gives the approximate height of the plateau.

## 6.2.2 Mean Charged Particle Multiplicity

In this section the mean charged multiplicity,  $\langle n_{ch} \rangle$ , dependence on the total invariant mass squared of the hadronic system,  $W^2$ , is investigated as well as the dependence on the momentum transfer square between the electron and the proton,  $Q^2$ .

Only charged particles within the pseudorapidity range  $-5 < \eta^* < -0.5$  are used in the determination of the  $\langle n_{ch} \rangle$ . Below  $\eta^* = -5$  the correction values have large errors and therefore become unreliable. Above  $\eta^* = -0.5$  the detector acceptances become important.

In figure 6.11.a - 6.11.d the corrected mean multiplicity  $\langle n_{ch} \rangle$  in the hadronic  $cms$  is shown as a function of  $W^2$  for the  $Q^2$  ranges 10-15, 15-26, 26-110 and  $Q^2 > 110 GeV^2$  respectively. The corrected  $\langle n_{ch} \rangle$  as a function of  $Q^2$  is depicted in figure 6.12.a - 6.12.c for the  $W$  ranges 85 - 123, 123 - 162 and  $W > 162 GeV$  respectively. The corrected values of the mean charged multiplicity are listed in table 6.8.

In figure 6.11 it can be seen that the mean multiplicity rises with increasing  $W^2$ , as expected from the increase of the phase space available for QCD radiation.

Three of the Monte Carlo models used in this study (Ariadne, MEPS and PSWQ) describe the data fairly well within error. It is only in the highest  $Q^2$  bin, that there is some discrepancy between data and the MEPS and PSWQ models.

In order to investigate the dependence of  $\langle n_{ch} \rangle$  on  $W^2$  (at fixed  $Q^2$ ) a  $\chi^2$  fit was performed both under the assumption of a constant multiplicity, independent of  $W^2$  and using the function  $\langle n_{ch} \rangle = a + b \cdot \ln W^2$ . The results are presented in table 6.5. The  $\chi^2/NDF$  value for the constant multiplicity fit is of the order of 10/2 while it is 1/1 for the logarithmic function. Furthermore, the value of  $b$  in the fit of the logarithmic function is, within a 95% confidence interval, different from zero. From this we conclude that, at fixed  $Q^2$ , the observed  $W^2$  dependence of the  $\langle n_{ch} \rangle$  is statistically significant and a  $\langle n_{ch} \rangle$  independent of  $W^2$  is unlikely.

Fit based on data points in figure	Fitted function $\langle n_{ch} \rangle = a$		Fitted function $\langle n_{ch} \rangle = a + b \cdot \ln W^2$		
	$a$	$\chi^2/NDF$	$a$	$b$	$\chi^2/NDF$
6.11a	$7.76 \pm 0.12$	7.7/2	$0.77 \pm 2.9$	$0.70 \pm 0.29$	1.9/1
6.11b	$7.61 \pm 0.12$	10.1/2	$0.73 \pm 2.60$	$0.70 \pm 0.26$	3.12/1
6.11c	$7.95 \pm 0.13$	16.5/2	$-3.18 \pm 2.75$	$1.11 \pm 0.28$	0.18/1
6.11d	$8.23 \pm 0.19$	12.2/2	$-4.76 \pm 3.90$	$1.28 \pm 0.38$	1.1/1

Table 6.5: Results of fitting two different functions to the data points in figure 6.11.

In figure 6.12.a - 6.12.c we see that the mean multiplicity, taken errors into account, is more or less independent of  $Q^2$ . The PSWQ curve follows the data within errors for the low and medium  $W^2$  ranges, but as  $W^2$  increases further, and especially for higher  $Q^2$ , the PSWQ model gives an average multiplicity that is about 10% - 20% larger than data. Both Ariadne and the MEPS model reproduce the data fairly well although the MEPS model has a slightly steeper slope than the data. The QPM, which does not contain any QCD radiation, accounts only for 75% of the measured multiplicity.

In order to determine if the mean charged multiplicity depends on  $Q^2$ , a  $\chi^2$  fit of a function assuming no dependence on  $Q^2$  was compared to a fit with a logarithmic  $Q^2$

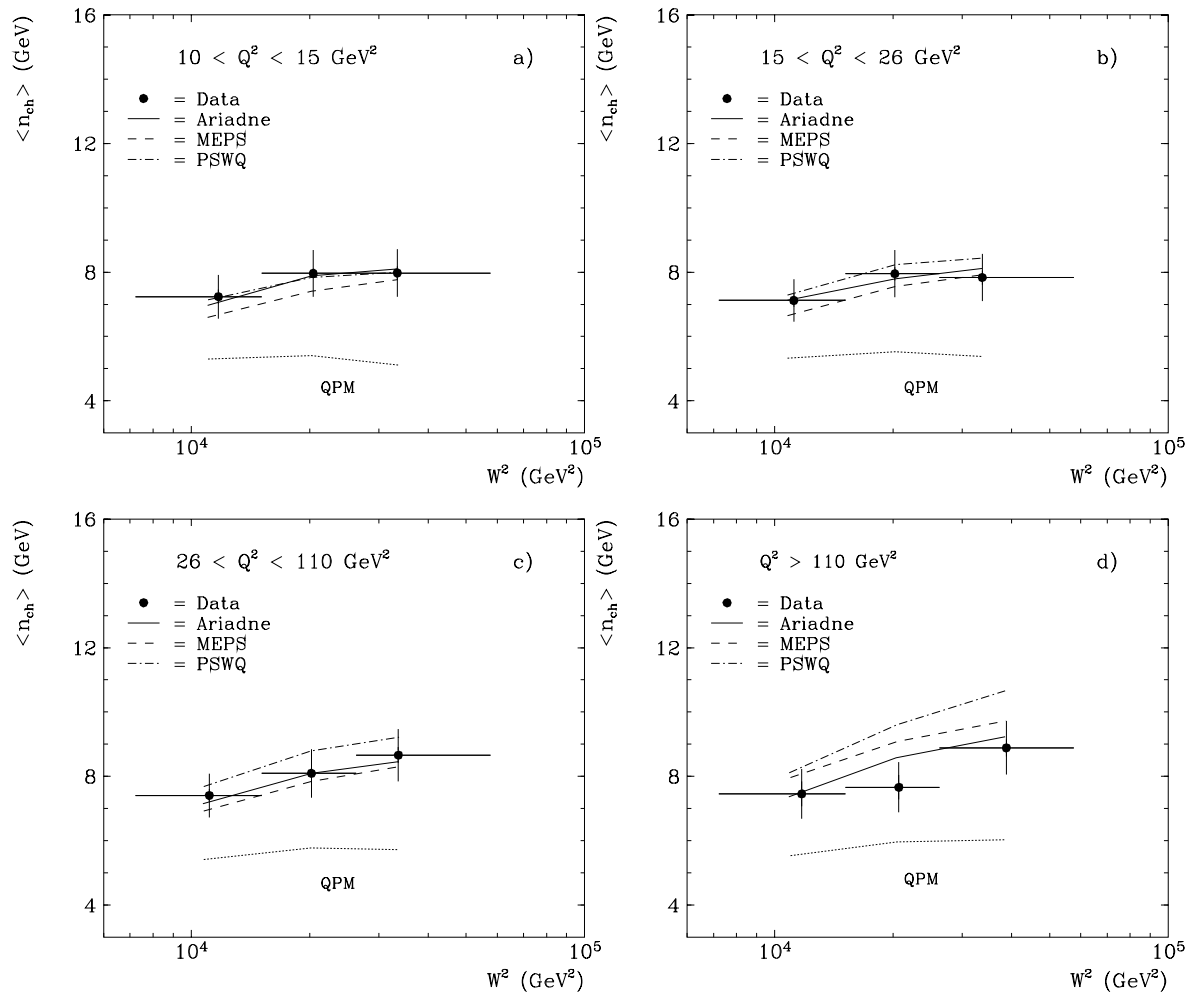


Figure 6.11: Mean charged multiplicity  $\langle n_{ch} \rangle$  measured in the pseudorapidity range  $-5 \leq \eta^* \leq -0.5$  as a function of  $W^2$  in three different  $Q^2$  intervals. The error bars contain the statistical and systematic errors added in quadrature.

dependence. The results of the fits are given in table 6.6. The logarithmic function gives in all  $W$  intervals a lower  $\chi^2/NDF$  value than the function assuming no  $Q^2$  dependence. Even so, in the two lowest  $W$  bins the parameter  $b$  is less than one sigma from zero,

Fit based on data points in figure	Fitted function $\langle n_{ch} \rangle = a$		Fitted function $\langle n_{ch} \rangle = a + b \cdot \ln Q^2$		
	$a$	$\chi^2/NDF$	$a$	$b$	$\chi^2/NDF$
6.12a	$7.27 \pm 0.11$	1.3/3	$6.96 \pm 0.39$	$0.09 \pm 0.11$	0.64/2
6.12b	$7.97 \pm 0.11$	1.0/3	$8.15 \pm 0.37$	$-0.06 \pm 0.10$	0.73/2
6.12c	$8.25 \pm 0.12$	13.6/3	$7.23 \pm 0.34$	$0.28 \pm 0.09$	3.63/2

Table 6.6: Results of fitting a constant function, independent of  $Q^2$ , and the logarithmic function  $\langle n_{ch} \rangle = a + b \cdot \ln Q^2$  to the data points in figure 6.12.

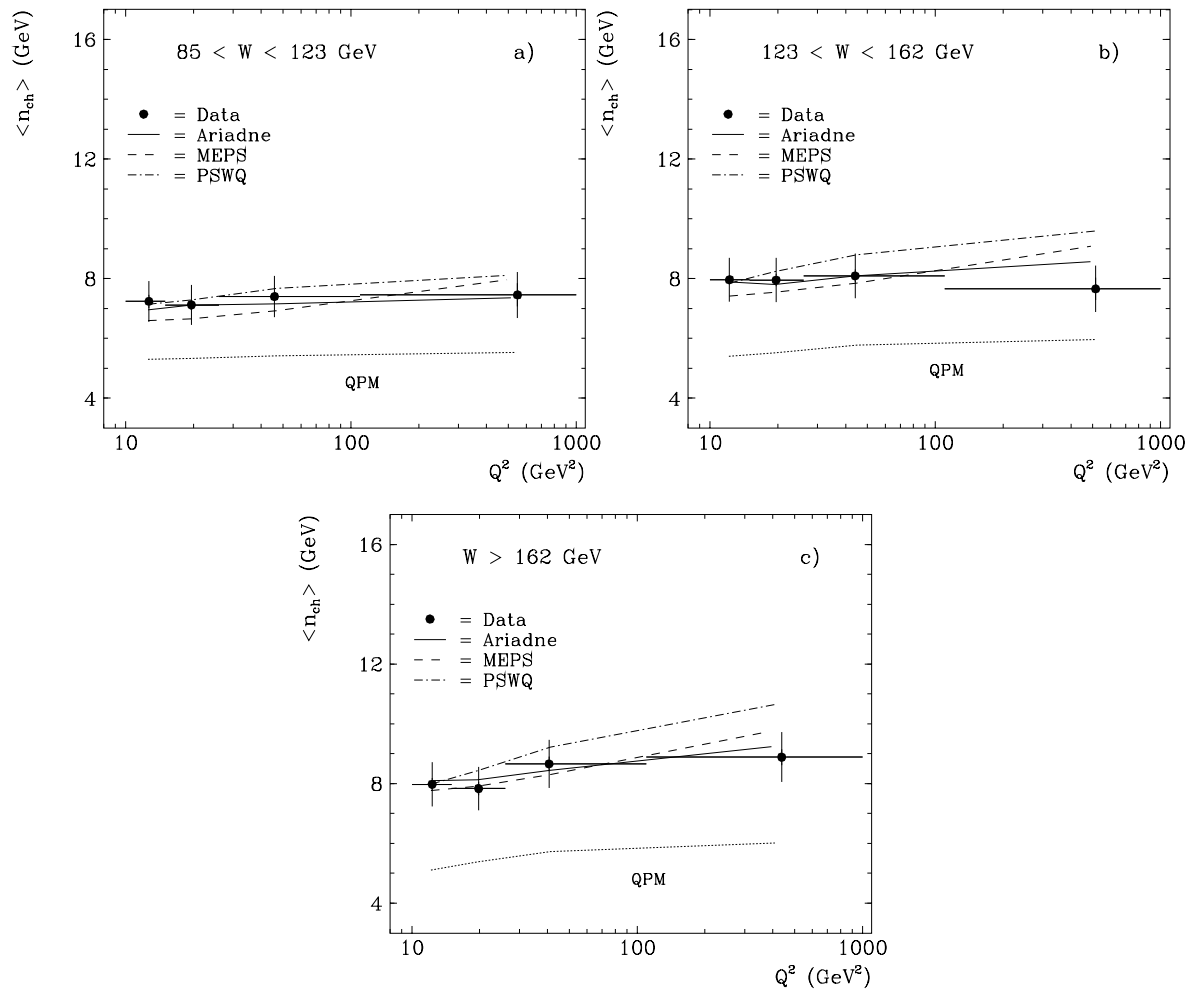


Figure 6.12: Mean charged multiplicity  $\langle n_{ch} \rangle$  measured in the pseudorapidity range  $-5 \leq \eta^* \leq -0.5$  as a function of  $Q^2$  in three different  $W$  intervals. The error bars contain the statistical and systematic errors added in quadrature.

which means that a logarithmic  $Q^2$  dependence in these  $W$  intervals cannot be established. However, for high  $W$  the value of  $b$  parameter is more than three sigma from zero, indicating some  $Q^2$  dependence, especially if one considers the high  $\chi^2/NDF$  value (13.6/3) of the fit of the alternative function  $\langle n_{ch} \rangle = a$ .

To investigate a possible dependence on both  $W^2$  and  $Q^2$  more thoroughly, three global fits were performed. In all fits the function 6.2<sup>2</sup> was used but in the first fit the  $c$  parameter was fixed at zero (testing a plain  $\ln W^2$  dependence), in the second the  $b$  and  $c$  parameters were both free and in the third the  $b$  parameter was fixed at zero (testing a plain  $\ln Q^2$  dependence). The results are shown in table 6.7. The parameter  $a$  gives the mean multiplicity at values of  $W^2$  and  $Q^2$  equal to  $1 \text{ GeV}^2$ . The obtained multiplicities in this region have, however, large uncertainties due to the extrapolations.

<sup>2</sup>The double log function 6.2 was chosen since it has been used in previous experiments [2], [4] and gave good results.

$$\langle n_{ch} \rangle = a + b \cdot \ln \left( \frac{W^2}{W_0^2} \right) + c \cdot \ln \left( \frac{Q^2}{Q_0^2} \right), \quad \text{where } W_0^2 = Q_0^2 = 1 \text{ GeV}^2 \quad (6.2)$$

With a  $\chi^2/NDF$  of 9.6/10 the first fit, containing only a  $W^2$  dependence, gives a good description of the data. Adding a  $\ln Q^2$  term improves the  $\chi^2/NDF$  slightly to 7.5/9. However, since the value of  $c$  is less than two sigmas from zero it cannot be concluded that the mean multiplicity also depends on  $Q^2$ . The third fit tests a plain  $Q^2$  dependence and gives a  $\chi^2/NDF$  of 43.9/10. This is a very large value which makes this hypothesis very unlikely.

$a$	$b$	$c$	$\chi^2/NDF$
$-1.38 \pm 0.07$	$0.93 \pm 0.05$	[0]	9.6/10
$-1.18 \pm 1.29$	$0.87 \pm 0.13$	$0.10 \pm 0.06$	7.5/9
$6.99 \pm 0.21$	[0]	$0.23 \pm 0.05$	43.9/10

Table 6.7: Fitted parameters  $a$ ,  $b$  and  $c$  in the function 6.2 as well as  $\chi^2/NDF$  for the average charged multiplicity in the hadronic cms in the pseudorapidity interval  $-5 < \eta^* < -0.5$ . In the first fit the parameter  $b$  was kept fixed at zero, in the second both parameter  $b$  and  $c$  were free and in the third the parameter  $c$  was fixed at zero.

To conclude: We see clear evidence for a dependence of the charged multiplicity on  $W^2$  whereas an additional dependence on  $Q^2$  is not verified. On the other hand the hypothesis that the charged multiplicity depends only on  $Q^2$  can be rejected.

$\langle W^2 \rangle [\text{GeV}^2]$	$\langle Q^2 \rangle [\text{GeV}^2]$	$\langle n_{ch} \rangle$
11605.67	12.64	$7.24 \pm .22 \pm .61$
11190.24	19.60	$7.12 \pm .19 \pm .60$
11071.30	46.31	$7.40 \pm .20 \pm .63$
11717.87	551.66	$7.45 \pm .39 \pm .63$
20468.56	12.21	$7.96 \pm .19 \pm .68$
20165.71	19.46	$7.95 \pm .21 \pm .67$
20403.33	43.32	$8.09 \pm .22 \pm .69$
20821.67	516.10	$7.66 \pm .38 \pm .65$
33364.10	12.22	$7.97 \pm .21 \pm .68$
33491.70	19.50	$7.83 \pm .22 \pm .66$
33835.36	39.88	$8.66 \pm .25 \pm .73$
38984.94	447.44	$8.88 \pm .27 \pm .75$

Table 6.8: Corrected values of  $\langle n_{ch} \rangle$  in the hadronic cms in the pseudorapidity range  $-5 \leq \eta^* \leq -0.5$  as a function of  $W^2$  and  $Q^2$ . The first error in the  $\langle n_{ch} \rangle$  column is the statistical, the second the systematic.

# Chapter 7

## Conclusions

Transverse energy  $E_T^*$  flow and charged particle  $n_{ch}$  flow have been investigated in the hadronic center of mass system as a function of pseudorapidity  $\eta^*$  in different  $W^2$  and  $Q^2$  intervals. Further, the variation of the mean transverse energy  $\langle E_T^* \rangle$ , in the pseudorapidity range  $-5.0 < \eta^* < 0.0$ , with  $W^2$  at fixed  $Q^2$  and with  $Q^2$  at fixed  $W^2$  has been studied. The variation of the mean charged particle multiplicity  $\langle n_{ch} \rangle$  has been investigated in the pseudorapidity range  $-5.0 < \eta^* < -0.5$ , as a function of  $W^2$  at fixed  $Q^2$  and as a function of  $Q^2$  at fixed  $W^2$ .

At low  $Q^2$  the *transverse energy*  $E_T^*$  as a function of pseudorapidity  $\eta^*$  exhibits a plateau in the current hemisphere,  $\eta^* < 0$ , with a  $E_T^* \approx 2 \text{ GeV}$  per unit of rapidity. The plateau rises as  $Q^2$  increases and, in the highest  $Q^2$  range measured, is  $\approx 3 \text{ GeV}$  per unit of rapidity. The plateau extends from about  $\eta^* \approx 0$  to  $\eta^* \approx -3$  for low  $W$  and becomes wider as  $W$  increases covering the range  $0 < \eta^* < -3.5$  in the highest  $W$  range.

The mean transverse energy  $\langle E_T^* \rangle$  depends both on the total invariant mass squared of the hadronic system  $W^2$  and the square of the momentum transfer between the electron and the proton  $Q^2$ .  $\chi^2$  fits show that neither a  $\ln W^2$  nor a  $\ln Q^2$  function alone is able to describe the data but only a combination of the two. The data is well described by

$$\langle E_T^* \rangle = \left[ a + b \cdot \ln \left( \frac{W^2}{W_0^2} \right) + c \cdot \ln \left( \frac{Q^2}{Q_0^2} \right) \right] \cdot W_0, \quad \text{where } W_0^2 = Q_0^2 = 1 \text{ GeV}^2 \quad (7.1)$$

with  $a = -5.93 \pm 0.07$ ,  $b = 1.28 \pm 0.06$  and  $c = 0.69 \pm 0.02$

The *charged multiplicity* flow as a function of pseudorapidity  $\eta^*$  exhibits, like the transverse energy flow, a plateau in the current hemisphere with a multiplicity of  $\approx 2$  particles per unit of rapidity. The height of the plateau is more or less independent of  $Q^2$ . The plateau extends from about  $\eta^* \approx -0.5$  to  $\eta^* \approx -3$  for low  $W$  and becomes wider as  $W$  increases covering approximately the range  $-0.3 < \eta^* < -3.2$  in the highest  $W$  range.

The mean charged multiplicity  $\langle n_{ch} \rangle$  depends clearly on  $\ln W^2$  but its dependence on  $Q^2$  cannot be verified. To be able to make a more definite statement on the  $Q^2$  dependence, a narrower binning in both  $Q^2$  and  $W^2$  is necessary, as well as an extension of the measurement to higher  $Q^2$  for which more data is needed. A satisfactory description of data is given by

$$\langle n_{ch} \rangle = a + b \cdot \ln \left( \frac{W^2}{W_0^2} \right), \quad \text{where } W_0 = 1 \text{ GeV}^2 \quad (7.2)$$

with  $a = -1.38 \pm 0.07$  and  $b = 0.93 \pm 0.05$

The observation that the mean transverse energy increases with  $Q^2$  but the mean charged multiplicity does not, could be explained if, instead of more particles being produced as  $Q^2$  increases, each particle obtains more energy.

Comparing the result of the mean charged multiplicity obtained in this study with results of previous fixed target experiments (see table 1.2 in chapter 1) we see that EMC, the experiment 'closest' to H1 in kinematic terms, reported a steeper growth of the mean multiplicity with  $\ln W^2$  (parameter  $b = 1.22$ ) than that observed here (parameter  $b = 0.93$ ). This difference may be due to different angular coverage of the two experiments. EMC has essentially a  $4\pi$  coverage which is not the case in H1. In future multiplicity studies with the H1 detector it may be possible to extend the measurements down to maybe  $6^\circ$ , making the difference in angular acceptance between the two experiments smaller.

The data sample used in the analysis presented here contains processes to all orders in  $\alpha_s$ , and therefore provides an inclusive measurement. With more data available it would be of interest to measure the  $n_{ch}$  and  $E_T^*$  dependence on  $Q^2$  and  $W^2$  for zeroth and higher order processes separately, since the composition of processes of different orders changes with  $Q^2$  and  $W^2$ .

Predictions produced by the Monte Carlo models Ariadne and Lepto (with the options MEPS, PSWQ and QPM) have been compared to the data. The best overall description of the data is provided by the Monte Carlo program Ariadne. The discrepancies between Ariadne and the data are largest in the forward direction, i.e. in the proton direction, where more  $E_T^*$  is produced in the data than by Ariadne. This tendency can also be seen in the charged particle flow although it is not as clear as in the  $E_T$  case. The  $\langle E_T^* \rangle$  in the data exhibits also a more pronounced dependence on  $Q^2$  than in Ariadne while the dependence on  $W^2$  is about the same in Ariadne and data. The mean charged multiplicity is well described by the Ariadne Monte Carlo.

# Bibliography

- [1] B. Gibbard et al., Phys. Rev. D 11 (1975) 2367.
- [2] M. Arneodo et al., EMC Collaboration, Phys. Lett. 165B (1985) 222.
- [3] M. Derrick et al., Phys. Rev. D 25 (1982) 624.
- [4] G.T. Jones et al., Z. Phys. C - Particles and Fields 46 (1990) 25.
- [5] F. Jacquet, A. Blondel, Proceedings of the study of an  $ep$  facility for Europe 79/48, (1979) 391, Ed. U Amaldi.
- [6] S. Bentvelsen, J. Engelen, P Kooijman, Reconstruction of  $(x, Q^2)$  and extraction of structure functions in neural current scattering at HERA. Physics at HERA, Proceedings of the workshop, Eds. W. Buchmüller and G. Ingelman, Hamburg (1991) Vol. 1, 23.
- [7] A.H. Mueller, Phys. Lett. 104B (1981) 161.
- [8] B. Andersson et al., Phys. Rep. 97 (1983) 31.
- [9] G. Ingelman, "LEPTO 6.1", Physics at HERA, Proceedings of the workshop, Eds. W. Buchmüller and G. Ingelman, Hamburg (1991) Vol. 3, 1366, and references therein.
- [10] L. Lönnblad, Comp. Phys. Commun. 71 (1992) 15, and references therein.
- [11] G. Gustafson, Phys. Lett. B175 (1986) 453,  
G. Gustafson, U. Petterson, Nucl. Phys. B306 (1988) 746,  
B. Andersson, G. Gustafson, L. Lönnblad, Nucl. Phys. B336 (1990) 393.  
T. Brodorb, J. G. Körner, Z. Phys. C54 (1992) 519
- [12] T. Sjöstrand, JETSET 7.3 program and manual see e.g. B. Bambah et. al., QCD Generators for LEP, CERN-TH.5466/89,  
T. Sjöstrand, Computer Phys. comm. 39 (1986) 347,  
T. Sjöstrand and M. Bengtsson, Z. Phys. C37 (1988) 465.
- [13] Physics at HERA, Proceedings of the workshop, Eds. W. Buchmüller and G. Ingelman, Hamburg (1991) Vol. 1, 275.
- [14] I. Abt et al., H1 collaboration, Phys. Lett. B298 (1993) 469.
- [15] M. Derrick et. al., ZEUS collaboration, Z. Phys. C59 (1993) 231.

- [16] H1 collaboration, I. Abt et al., The H1 detector at HERA, DESY preprint, DESY 93-103, July 1993.
- [17] Physics at HERA, Proceedings of the workshop, Eds. W. Buchmüller and G. Ingelman, Hamburg (1991) vol. 1, p. 1
- [18] H1 collaboration, March 1986, Technical Progress Report
- [19] D. Handshuh, PhD Thesis, Universität Hamburg, 1993. Studien zum Protoninduzierten Untergrund am H1 Detector und Entwicklung von Filteralgorithmen zu dessen Unterdrückung
- [20] Ed. J. Meyer, Guide for H1 simulation program H1SIM, H1 Software note 3, DESY, Hamburg (October 1989), unpublished.
- [21] The official reconstruction program used at the H1-experiment.
- [22] K. C. Hoeger, Measurement of  $x, y, Q^2$  in Neutral Current Events. Physics at HERA, Proceedings of the workshop, Eds. W. Buchmüller and G. Ingelman, Hamburg (1991) Vol. 1, 43.
- [23] I. Abt et al., H1 collaboration, Nucl Phys. B407 (1993) 515.
- [24] I. Abt et al., H1 collaboration, Energy Flow and Charged Particle Spectra in Deep Inelastic Scattering at HERA., DESY preprint, DESY 94-033, March 1994.
- [25] I. Abt et al., H1 collaboration, Deep Inelastic Scattering Events with Large Rapidity Gap at HERA. DESY preprint, DESY 94-133, July 1994.
- [26] Physics at HERA, Proceedings of the workshop, Eds. W. Buchmüller and G. Ingelman, Hamburg (1991) Vol. 3, 1419.
- [27] H. Jung, "Hard diffractive scattering in high-energy  $ep$  collisions and the Monte Carlo generator RAPGAP", DESY preprint 93-182 (1983).
- [28] H. Kuester, On the Treatment of Calorimeter Cells and Clusters in H1REC and PHAN Physics Analysis, H1 Software note 45, DESY, Hamburg (March 1994), unpublished.
- [29] A.D. Martin, W.J. Stirling, R.G. Roberts, Phys. Lett. B306 (1993) 145, Phys. Lett. B309 (1993) 492.

# List of Figures

1.1	The kinematic region in $x$ and $Q^2$ covered by fixed target experiments and by HERA. . . . .	3
2.1	A schematic view of the DIS process in the laboratory system . . . . .	6
2.2	A schematic view of the DIS process according to the quark parton model depicted in the hadronic <i>cms</i> . . . . .	7
2.3	The different subprocesses in a DIS event . . . . .	8
2.4	The first order $\alpha_s$ processes, the QCD-Compton and photon-gluon-fusion processes. . . . .	10
2.5	Illustration of initial- and final-state parton showers . . . . .	11
2.6	The available phase-space for dipole radiation in the hadronic <i>cms</i> . . . . .	12
2.7	A schematic view of the fragmentation process . . . . .	14
3.1	The Feynman diagrams for the QCD-Compton process . . . . .	19
3.2	The Feynman diagrams for the photon-gluon fusion process . . . . .	20
3.3	Schematic view of the different steps in the generation of an event . . . . .	21
4.1	The accelerator complex at DESY . . . . .	24
4.2	The preaccelerator system at DESY . . . . .	25
4.3	Cross section of the H1 detector . . . . .	26
4.4	Layout of the tracking system in the H1 detector . . . . .	28
4.5	Cross section of the drift cells in the central tracking system . . . . .	29
4.6	Cross section of the central tracking system showing reconstructed tracks and mirror tracks . . . . .	30
4.7	Longitudinal view of the calorimeter system . . . . .	33
4.8	Cross section of the backward electromagnetic calorimeter (BEMC) . . . . .	34
4.9	A schematic view of the forward muon detector . . . . .	35
4.10	The scintillator system and its position relative to the nominal interaction point in the H1 detector . . . . .	36
4.11	Example of a typical low $Q^2$ DIS event . . . . .	38
4.12	Example of a typical high $Q^2$ DIS event . . . . .	38
5.1	Schematic view of the different steps in the analysis chain. . . . .	40
5.2	The relative error in the reconstruction of $Q^2$ , $y$ and $W$ . . . . .	41
5.3	The distribution of the event variables $Q^2$ and $W$ for data and Monte Carlo after event selection . . . . .	42
5.4	The kinematic region in $x$ and $Q^2$ covered in this study . . . . .	44
5.5	The effects of radiative events on the transverse energy flow shown in the hadronic <i>cms</i> . . . . .	45

5.6	An example of a correction function for the transverse energy flow in the hadronic <i>cms</i> . . . . .	49
5.7	An example of a correction function for the charged particle flow in the hadronic <i>cms</i> . . . . .	50
6.1	The transverse energy flow $E_T^*$ in the hadronic <i>cms</i> as a function of pseudorapidity $\eta^*$ for events in the $W$ range 85 - 123 <i>GeV</i> . . . . .	54
6.2	The transverse energy flow $E_T^*$ in the hadronic <i>cms</i> as a function of pseudorapidity $\eta^*$ for events in the $W$ range 123 - 162 <i>GeV</i> . . . . .	55
6.3	The transverse energy flow $E_T^*$ in the hadronic <i>cms</i> as a function of pseudorapidity $\eta^*$ for events with $W > 162$ <i>GeV</i> . . . . .	56
6.4	The transverse energy flow $E_T^*$ ordered in $Q^2$ and $W$ bins. . . . .	57
6.5	Mean transverse energy $\langle E_T^* \rangle$ in the hadronic <i>cms</i> as a function of $W^2$ .	59
6.6	Mean transverse energy $\langle E_T^* \rangle$ in the hadronic <i>cms</i> as a function of $Q^2$ .	60
6.7	The charged particle flow $n_{ch}$ in the hadronic <i>cms</i> as a function of pseudorapidity $\eta^*$ for events in the $W$ range 85 - 123 <i>GeV</i> . . . . .	63
6.8	The charged particle flow $n_{ch}$ in the hadronic <i>cms</i> as a function of pseudorapidity $\eta^*$ for events in the $W$ range 123 - 162 <i>GeV</i> . . . . .	64
6.9	The charged particle flow $n_{ch}$ in the hadronic <i>cms</i> as a function of pseudorapidity $\eta^*$ for events with $W > 162$ <i>GeV</i> . . . . .	65
6.10	The charged particle flow $n_{ch}$ ordered in $Q^2$ and $W$ bins. . . . .	66
6.11	Mean charged multiplicity $\langle n_{ch} \rangle$ in the hadronic <i>cms</i> as a function of $W^2$	68
6.12	Mean charged multiplicity $\langle n_{ch} \rangle$ in the hadronic <i>cms</i> as a function of $Q^2$	69

# List of Tables

1.1	The elementary particles, their masses and the type of interaction that affects them . . . . .	1
1.2	Fitted parameters for charged hadrons from different experiments. . . . .	3
4.1	Summary of some HERA parameters . . . . .	23
5.1	Number of events in each $(Q^2, W)$ bin for the final data sample . . . . .	47
5.2	Fraction of the events reconstructed in the $i$ :th $Q^2$ interval which were generated in the $j$ :th interval. . . . .	47
5.3	Fraction of the events reconstructed in the $i$ :th $W$ interval which were generated in the $j$ :th interval. . . . .	48
5.4	The average value of the kinematic variables $Q^2$ and $W$ in each $(Q^2, W)$ bin	48
5.5	The systematic uncertainties of the energy and particle flow measurements	51
6.1	Results of investigating the $W^2$ dependence in the mean transverse energy flow . . . . .	59
6.2	Results of investigating the $Q^2$ dependence in the mean transverse energy flow . . . . .	61
6.3	Fitted parameters $a, b, c$ and $\chi^2/\text{NDF}$ for the average transverse energy $\langle E_T^* \rangle$ . . . . .	61
6.4	Corrected values for the $\langle E_T^* \rangle$ in the hadronic $cms$ as a function of $W^2$ and $Q^2$ . . . . .	62
6.5	Results of investigating the $W^2$ dependence in the mean charged particle flow . . . . .	67
6.6	Results of investigating the $Q^2$ dependence in the mean charged particle flow	68
6.7	Fitted parameters $a, b, c$ and $\chi^2/\text{NDF}$ for the average charged multiplicity $\langle n_{ch} \rangle$ . . . . .	70
6.8	Corrected values of $\langle n_{ch} \rangle$ in the hadronic $cms$ as a function of $W^2$ and $Q^2$ . . . . .	70
A.1	Corrected transverse energy flow $E_T^*$ as a function the pseudorapidity $\eta$ in the range $85 < W < 123 \text{ GeV}$ . . . . .	79
A.2	Corrected transverse energy flow $E_T^*$ as a function the pseudorapidity $\eta$ in the range $123 < W < 162 \text{ GeV}$ . . . . .	80
A.3	Corrected transverse energy flow $E_T^*$ as a function the pseudorapidity $\eta$ for $W > 162 \text{ GeV}$ . . . . .	81
A.4	Corrected charged particle flow in the range $85 < W < 123 \text{ GeV}$ . . . . .	82
A.5	Corrected charged particle spectra in the range $123 < W < 162 \text{ GeV}$ . . .	83
A.6	Corrected charged particle spectra for $W > 162 \text{ GeV}$ . . . . .	84



# Appendix A

## List of data values

$\eta^*$	$1/NdE_T^*/d\eta^*$			
	$85 < W < 123$ $10 < Q^2 < 15$	$85 < W < 123$ $15 < Q^2 < 26$	$85 < W < 123$ $26 < Q^2 < 110$	$85 < W < 123$ $Q^2 > 110$
-5.50 - -5.25	0.02 ± .01 ± .00	0.02 ± .01 ± .00	0.01 ± .01 ± .00	0.01 ± .01 ± .00
-5.25 - -5.00	0.03 ± .01 ± .00	0.04 ± .01 ± .00	0.05 ± .01 ± .01	0.05 ± .05 ± .01
-5.00 - -4.75	0.07 ± .02 ± .01	0.10 ± .02 ± .01	0.06 ± .01 ± .01	0.01 ± .01 ± .00
-4.75 - -4.50	0.15 ± .03 ± .02	0.20 ± .03 ± .02	0.14 ± .02 ± .02	0.03 ± .02 ± .01
-4.50 - -4.25	0.28 ± .05 ± .04	0.24 ± .03 ± .03	0.23 ± .03 ± .03	0.20 ± .12 ± .02
-4.25 - -4.00	0.50 ± .07 ± .06	0.59 ± .07 ± .07	0.47 ± .06 ± .06	0.20 ± .10 ± .02
-4.00 - -3.75	0.88 ± .10 ± .11	0.87 ± .09 ± .11	0.76 ± .08 ± .10	0.40 ± .19 ± .05
-3.75 - -3.50	1.51 ± .25 ± .19	1.22 ± .13 ± .15	0.95 ± .09 ± .12	1.28 ± .37 ± .16
-3.50 - -3.25	2.01 ± .35 ± .26	1.60 ± .16 ± .20	1.56 ± .16 ± .20	1.32 ± .40 ± .17
-3.25 - -3.00	1.65 ± .17 ± .20	2.42 ± .25 ± .31	2.03 ± .21 ± .26	1.78 ± .38 ± .23
-3.00 - -2.75	1.95 ± .19 ± .25	2.13 ± .19 ± .27	2.41 ± .22 ± .31	2.78 ± .64 ± .35
-2.75 - -2.50	1.97 ± .19 ± .25	1.91 ± .17 ± .24	3.05 ± .39 ± .39	2.50 ± .59 ± .32
-2.50 - -2.25	1.94 ± .18 ± .25	2.33 ± .21 ± .29	2.85 ± .25 ± .36	2.94 ± .66 ± .38
-2.25 - -2.00	2.18 ± .21 ± .26	2.08 ± .19 ± .27	2.73 ± .25 ± .35	2.90 ± .64 ± .37
-2.00 - -1.75	1.92 ± .19 ± .23	1.92 ± .17 ± .24	2.31 ± .19 ± .30	4.17 ± .89 ± .53
-1.75 - -1.50	1.97 ± .17 ± .24	2.12 ± .17 ± .27	2.48 ± .20 ± .32	2.73 ± .64 ± .35
-1.50 - -1.25	1.87 ± .15 ± .24	2.25 ± .18 ± .29	2.42 ± .19 ± .28	2.75 ± .57 ± .35
-1.25 - -1.00	1.92 ± .15 ± .25	2.22 ± .17 ± .28	2.26 ± .16 ± .29	2.82 ± .60 ± .36
-1.00 - -0.75	2.03 ± .15 ± .26	2.21 ± .16 ± .28	2.47 ± .17 ± .32	2.32 ± .53 ± .30
-0.75 - -0.50	2.02 ± .14 ± .26	2.16 ± .16 ± .28	2.58 ± .19 ± .33	2.80 ± .63 ± .36
-0.50 - -0.25	2.02 ± .15 ± .26	2.17 ± .17 ± .28	2.25 ± .16 ± .29	2.32 ± .41 ± .30
-0.25 - 0.00	1.93 ± .14 ± .25	2.08 ± .13 ± .27	2.18 ± .16 ± .27	2.30 ± .44 ± .29
0.00 - 0.25	2.07 ± .16 ± .26	1.74 ± .12 ± .22	1.99 ± .15 ± .25	1.98 ± .33 ± .25
0.25 - 0.50	1.28 ± .11 ± .16	1.12 ± .08 ± .14	1.22 ± .10 ± .16	1.14 ± .23 ± .15
0.50 - 0.75	0.21 ± .03 ± .02	0.18 ± .02 ± .02	0.21 ± .03 ± .02	0.41 ± .11 ± .05

Table A.1: Corrected transverse energy flow  $E_T^*$  in the hadronic center of mass system as a function of the pseudorapidity  $\eta^*$  in the range  $85 < W < 123$  GeV for different  $Q^2$  intervals. The first error is the statistical, the second the systematic; the overall error of 6% of the hadronic energy scale is not included.

$\eta^*$	$1/NdE_T^*/d\eta^*$			
	$123 < W < 162$ $10 < Q^2 < 15$	$123 < W < 162$ $15 < Q^2 < 26$	$123 < W < 162$ $26 < Q^2 < 110$	$123 < W < 162$ $Q^2 > 110$
-5.50 - -5.25	0.06 ± .01 ± .00	0.05 ± .02 ± .01	0.04 ± .01 ± .01	0.01 ± .01 ± .00
-5.25 - -5.00	0.08 ± .02 ± .01	0.13 ± .03 ± .02	0.06 ± .02 ± .01	0.03 ± .01 ± .00
-5.00 - -4.75	0.18 ± .03 ± .02	0.14 ± .03 ± .02	0.12 ± .02 ± .02	0.09 ± .04 ± .01
-4.75 - -4.50	0.28 ± .04 ± .03	0.37 ± .06 ± .05	0.20 ± .03 ± .02	0.12 ± .05 ± .01
-4.50 - -4.25	0.59 ± .07 ± .08	0.47 ± .06 ± .06	0.49 ± .06 ± .06	0.68 ± .20 ± .09
-4.25 - -4.00	0.80 ± .10 ± .10	0.97 ± .11 ± .12	0.77 ± .09 ± .10	0.42 ± .13 ± .05
-4.00 - -3.75	1.10 ± .11 ± .14	1.11 ± .13 ± .14	1.04 ± .11 ± .13	0.82 ± .18 ± .10
-3.75 - -3.50	1.71 ± .17 ± .22	1.71 ± .17 ± .22	1.60 ± .15 ± .20	0.95 ± .24 ± .12
-3.50 - -3.25	2.14 ± .19 ± .27	1.97 ± .20 ± .25	1.98 ± .19 ± .25	1.91 ± .36 ± .24
-3.25 - -3.00	1.91 ± .16 ± .24	2.67 ± .25 ± .34	2.32 ± .22 ± .30	1.54 ± .27 ± .20
-3.00 - -2.75	2.11 ± .17 ± .27	2.04 ± .19 ± .26	2.40 ± .23 ± .31	2.77 ± .50 ± .35
-2.75 - -2.50	2.32 ± .19 ± .30	2.22 ± .21 ± .28	2.59 ± .25 ± .33	3.19 ± .54 ± .41
-2.50 - -2.25	2.18 ± .20 ± .28	2.00 ± .20 ± .26	2.69 ± .26 ± .34	4.10 ± .78 ± .52
-2.25 - -2.00	2.07 ± .18 ± .26	2.25 ± .22 ± .29	2.91 ± .28 ± .37	4.28 ± .72 ± .55
-2.00 - -1.75	2.14 ± .17 ± .27	2.13 ± .19 ± .27	2.66 ± .25 ± .34	3.38 ± .63 ± .43
-1.75 - -1.50	1.89 ± .15 ± .24	2.26 ± .24 ± .29	2.17 ± .20 ± .28	3.29 ± .62 ± .42
-1.50 - -1.25	2.25 ± .18 ± .29	2.17 ± .21 ± .28	2.49 ± .22 ± .32	2.74 ± .52 ± .35
-1.25 - -1.00	2.17 ± .15 ± .28	2.23 ± .19 ± .28	2.14 ± .17 ± .27	3.88 ± .77 ± .50
-1.00 - -0.75	2.11 ± .14 ± .27	1.88 ± .14 ± .24	2.14 ± .16 ± .27	3.03 ± .60 ± .39
-0.75 - -0.50	2.24 ± .14 ± .29	2.29 ± .17 ± .29	2.20 ± .16 ± .28	2.56 ± .43 ± .33
-0.50 - -0.25	2.18 ± .14 ± .28	2.10 ± .14 ± .27	2.24 ± .17 ± .29	3.00 ± .56 ± .38
-0.25 - 0.00	2.31 ± .14 ± .39	2.30 ± .17 ± .29	2.23 ± .15 ± .28	2.38 ± .30 ± .30
0.00 - 0.25	2.09 ± .13 ± .27	2.05 ± .15 ± .26	2.16 ± .15 ± .28	2.52 ± .38 ± .32
0.25 - 0.50	2.07 ± .14 ± .26	1.98 ± .15 ± .25	2.20 ± .16 ± .28	2.17 ± .32 ± .28
0.50 - 0.75	1.74 ± .11 ± .22	1.58 ± .11 ± .20	1.67 ± .12 ± .21	1.64 ± .23 ± .21
0.75 - 1.00	0.28 ± .03 ± .03	0.30 ± .03 ± .04	0.44 ± .05 ± .06	0.60 ± .13 ± .08

Table A.2: Corrected transverse energy flow  $E_T^*$  in the hadronic center of mass system as a function of the pseudorapidity  $\eta^*$  in the range  $123 < W < 162$  GeV for different  $Q^2$  intervals. The first error is the statistical, the second the systematic; the overall error of 6% of the hadronic energy scale is not included.

$\eta^*$	$1/NdE_T^*/d\eta^*$			
	$W > 162$ $10 < Q^2 < 15$	$W > 162$ $15 < Q^2 < 26$	$W > 162$ $26 < Q^2 < 110$	$W > 162$ $Q^2 > 110$
-5.50 - -5.25	0.04 ± .01 ± .01	0.05 ± .01 ± .01	0.09 ± .03 ± .01	0.08 ± .04 ± .01
-5.25 - -5.00	0.17 ± .03 ± .02	0.15 ± .03 ± .02	0.19 ± .06 ± .02	0.07 ± .03 ± .01
-5.00 - -4.75	0.27 ± .04 ± .03	0.18 ± .03 ± .02	0.17 ± .04 ± .02	0.19 ± .04 ± .02
-4.75 - -4.50	0.45 ± .06 ± .06	0.49 ± .07 ± .06	0.54 ± .09 ± .07	0.37 ± .08 ± .05
-4.50 - -4.25	0.60 ± .07 ± .08	0.73 ± .09 ± .09	0.60 ± .08 ± .08	0.57 ± .12 ± .07
-4.25 - -4.00	0.99 ± .13 ± .13	0.93 ± .12 ± .12	0.94 ± .12 ± .12	0.97 ± .17 ± .12
-4.00 - -3.75	1.57 ± .16 ± .20	1.55 ± .18 ± .20	1.08 ± .13 ± .14	1.41 ± .23 ± .14
-3.75 - -3.50	1.69 ± .17 ± .22	2.13 ± .25 ± .27	2.15 ± .23 ± .27	1.66 ± .24 ± .21
-3.50 - -3.25	2.28 ± .21 ± .29	2.05 ± .20 ± .26	2.47 ± .26 ± .32	2.07 ± .30 ± .26
-3.25 - -3.00	2.37 ± .20 ± .30	2.35 ± .21 ± .30	2.29 ± .23 ± .29	3.13 ± .42 ± .40
-3.00 - -2.75	2.08 ± .19 ± .26	2.15 ± .21 ± .27	2.75 ± .30 ± .35	3.41 ± .48 ± .43
-2.75 - -2.50	2.37 ± .24 ± .30	2.29 ± .23 ± .29	2.57 ± .27 ± .31	3.45 ± .48 ± .44
-2.50 - -2.25	2.23 ± .21 ± .28	2.10 ± .21 ± .27	2.60 ± .31 ± .33	3.65 ± .54 ± .47
-2.25 - -2.00	2.56 ± .26 ± .33	2.32 ± .27 ± .29	2.51 ± .26 ± .32	4.05 ± .54 ± .52
-2.00 - -1.75	2.34 ± .20 ± .30	2.46 ± .30 ± .31	3.07 ± .35 ± .39	3.08 ± .42 ± .39
-1.75 - -1.50	2.19 ± .19 ± .28	2.33 ± .23 ± .30	2.36 ± .23 ± .30	3.72 ± .55 ± .48
-1.50 - -1.25	2.06 ± .16 ± .26	2.32 ± .21 ± .30	2.43 ± .26 ± .31	3.13 ± .42 ± .40
-1.25 - -1.00	1.95 ± .15 ± .25	2.30 ± .20 ± .29	2.68 ± .24 ± .34	2.75 ± .36 ± .35
-1.00 - -0.75	1.95 ± .14 ± .25	2.43 ± .18 ± .31	2.40 ± .21 ± .31	3.66 ± .46 ± .47
-0.75 - -0.50	2.02 ± .13 ± .26	2.27 ± .16 ± .29	2.20 ± .19 ± .28	2.88 ± .31 ± .37
-0.50 - -0.25	2.31 ± .17 ± .29	2.38 ± .17 ± .30	2.25 ± .17 ± .29	2.99 ± .38 ± .38
-0.25 - 0.00	2.27 ± .15 ± .29	2.33 ± .17 ± .30	2.21 ± .17 ± .28	2.52 ± .28 ± .32
0.00 - 0.25	1.99 ± .13 ± .25	2.29 ± .16 ± .29	2.24 ± .16 ± .29	2.28 ± .22 ± .29
0.25 - 0.50	2.09 ± .13 ± .27	2.20 ± .15 ± .28	2.14 ± .16 ± .27	2.61 ± .28 ± .33
0.50 - 0.75	2.01 ± .13 ± .26	2.17 ± .15 ± .28	2.00 ± .15 ± .26	2.30 ± .22 ± .29
0.75 - 1.00	1.61 ± .11 ± .21	1.82 ± .12 ± .23	1.56 ± .12 ± .20	1.92 ± .19 ± .24
1.00 - 1.25	0.34 ± .03 ± .04	0.40 ± .04 ± .16	0.37 ± .04 ± .05	0.88 ± .10 ± .11

Table A.3: Corrected transverse energy flow  $E_T^*$  in the hadronic center of mass system as a function of the pseudorapidity  $\eta^*$  for  $W > 162$  GeV in different  $Q^2$  intervals. The first error is the statistical, the second the systematic; the overall error of 6% of the hadronic energy scale is not included.

$\eta^*$	$1/N dn_{ch}/d\eta^*$			
	$85 < W < 123$ $10 < Q^2 < 15$	$85 < W < 123$ $15 < Q^2 < 26$	$85 < W < 123$ $26 < Q^2 < 110$	$85 < W < 123$ $Q^2 > 110$
-5.25 - -5.00	0.20 ± .05 ± .03	0.15 ± .04 ± .02	0.12 ± .04 ± .02	0.38 ± .29 ± .05
-5.00 - -4.75	0.25 ± .06 ± .03	0.25 ± .06 ± .03	0.23 ± .05 ± .03	0.00 ± .00 ± .00
-4.75 - -4.50	0.44 ± .08 ± .06	0.33 ± .05 ± .04	0.28 ± .05 ± .04	0.11 ± .11 ± .01
-4.50 - -4.25	0.44 ± .07 ± .06	0.59 ± .08 ± .08	0.56 ± .09 ± .07	0.33 ± .19 ± .04
-4.25 - -4.00	1.09 ± .15 ± .14	0.92 ± .11 ± .12	0.71 ± .09 ± .09	0.94 ± .34 ± .12
-4.00 - -3.75	1.09 ± .13 ± .14	0.99 ± .11 ± .13	1.09 ± .12 ± .14	0.66 ± .25 ± .08
-3.75 - -3.50	1.31 ± .15 ± .17	1.42 ± .14 ± .18	1.45 ± .14 ± .24	1.91 ± .50 ± .25
-3.50 - -3.25	1.38 ± .16 ± .18	1.86 ± .18 ± .24	1.93 ± .18 ± .25	1.51 ± .42 ± .19
-3.25 - -3.00	1.85 ± .20 ± .24	1.78 ± .17 ± .23	2.13 ± .19 ± .27	1.30 ± .37 ± .17
-3.00 - -2.75	2.23 ± .22 ± .29	2.06 ± .18 ± .27	2.31 ± .21 ± .30	2.04 ± .47 ± .26
-2.75 - -2.50	2.41 ± .25 ± .31	2.19 ± .20 ± .28	2.17 ± .20 ± .28	2.37 ± .55 ± .31
-2.50 - -2.25	2.56 ± .26 ± .33	2.38 ± .21 ± .31	2.50 ± .23 ± .32	2.17 ± .51 ± .28
-2.25 - -2.00	2.45 ± .24 ± .32	1.96 ± .18 ± .25	2.21 ± .20 ± .29	2.83 ± .62 ± .37
-2.00 - -1.75	2.07 ± .21 ± .27	1.96 ± .18 ± .25	2.03 ± .20 ± .26	2.35 ± .54 ± .30
-1.75 - -1.50	2.16 ± .23 ± .28	2.32 ± .22 ± .30	2.00 ± .20 ± .26	3.27 ± .72 ± .42
-1.50 - -1.25	2.12 ± .25 ± .27	2.09 ± .22 ± .27	2.34 ± .25 ± .30	2.39 ± .59 ± .31
-1.25 - -1.00	2.05 ± .27 ± .27	2.44 ± .28 ± .32	2.52 ± .27 ± .33	2.26 ± .63 ± .29
-1.00 - -0.75	1.79 ± .22 ± .23	2.09 ± .22 ± .27	2.20 ± .23 ± .29	2.18 ± .52 ± .28
-0.75 - -0.50	1.36 ± .17 ± .18	1.42 ± .16 ± .18	1.69 ± .17 ± .22	1.62 ± .43 ± .21
-0.50 - -0.25	0.74 ± .12 ± .10	0.70 ± .10 ± .09	0.74 ± .10 ± .09	0.91 ± .31 ± .12
-0.25 - 0.00	0.01 ± .01 ± .00	0.04 ± .02 ± .01	0.10 ± .04 ± .01	0.12 ± .09 ± .01

Table A.4: Corrected charged particle spectra in the hadronic center of mass system as a function of the pseudorapidity  $\eta^*$  in the range  $85 < W < 123$  GeV for different  $Q^2$  intervals. The first error is the statistical, the second the systematic

$\eta^*$	$1/N dn_{ch}/d\eta^*$			
	$123 < W < 162$ $10 < Q^2 < 15$	$123 < W < 162$ $15 < Q^2 < 26$	$123 < W < 162$ $26 < Q^2 < 110$	$123 < W < 162$ $Q^2 > 110$
-5.50 - -5.25	0.12 ± .04 ± .02	0.17 ± .05 ± .02	0.18 ± .05 ± .02	0.14 ± .10 ± .02
-5.25 - -5.00	0.20 ± .05 ± .03	0.25 ± .06 ± .03	0.22 ± .05 ± .03	0.15 ± .08 ± .02
-5.00 - -4.75	0.33 ± .07 ± .04	0.33 ± .06 ± .04	0.32 ± .06 ± .04	0.34 ± .14 ± .04
-4.75 - -4.50	0.43 ± .08 ± .06	0.44 ± .07 ± .06	0.53 ± .08 ± .07	0.59 ± .18 ± .08
-4.50 - -4.25	0.57 ± .08 ± .07	0.78 ± .11 ± .10	0.95 ± .12 ± .12	0.61 ± .17 ± .08
-4.25 - -4.00	0.82 ± .09 ± .11	1.09 ± .13 ± .14	1.20 ± .14 ± .16	0.81 ± .23 ± .10
-4.00 - -3.75	1.18 ± .12 ± .15	1.30 ± .14 ± .17	1.12 ± .12 ± .14	0.88 ± .24 ± .11
-3.75 - -3.50	1.49 ± .14 ± .19	1.54 ± .16 ± .20	1.61 ± .14 ± .21	1.17 ± .28 ± .15
-3.50 - -3.25	2.00 ± .17 ± .26	1.78 ± .18 ± .23	1.71 ± .15 ± .22	1.37 ± .30 ± .18
-3.25 - -3.00	2.33 ± .18 ± .30	1.88 ± .17 ± .24	1.76 ± .17 ± .23	1.90 ± .33 ± .25
-3.00 - -2.75	2.43 ± .20 ± .33	2.37 ± .21 ± .31	2.27 ± .20 ± .29	2.15 ± .37 ± .28
-2.75 - -2.50	2.54 ± .19 ± .32	2.22 ± .20 ± .29	2.38 ± .21 ± .31	2.37 ± .42 ± .31
-2.50 - -2.25	2.29 ± .18 ± .30	2.23 ± .19 ± .29	2.36 ± .21 ± .31	2.71 ± .44 ± .35
-2.25 - -2.00	2.22 ± .18 ± .29	2.10 ± .19 ± .28	2.53 ± .23 ± .33	2.42 ± .42 ± .31
-2.00 - -1.75	2.09 ± .17 ± .27	2.32 ± .20 ± .30	2.64 ± .23 ± .34	2.33 ± .39 ± .30
-1.75 - -1.50	2.49 ± .20 ± .32	2.10 ± .19 ± .27	2.43 ± .23 ± .32	1.97 ± .37 ± .25
-1.50 - -1.25	2.28 ± .19 ± .30	2.64 ± .23 ± .34	2.20 ± .21 ± .29	2.47 ± .49 ± .32
-1.25 - -1.00	2.32 ± .21 ± .30	1.78 ± .19 ± .23	2.05 ± .21 ± .27	2.84 ± .55 ± .37
-1.00 - -0.75	2.29 ± .23 ± .29	2.28 ± .27 ± .30	2.44 ± .27 ± .32	2.18 ± .47 ± .28
-0.75 - -0.50	1.96 ± .19 ± .25	2.38 ± .25 ± .31	1.97 ± .22 ± .25	1.57 ± .39 ± .20
-0.50 - -0.25	1.77 ± .16 ± .23	2.05 ± .21 ± .27	2.00 ± .21 ± .26	1.26 ± .33 ± .16
-0.25 - 0.00	1.03 ± .14 ± .14	1.03 ± .13 ± .14	1.14 ± .14 ± .15	0.82 ± .20 ± .11
0.00 - 0.25	0.10 ± .04 ± .01	0.06 ± .02 ± .01	0.06 ± .03 ± .01	0.40 ± .18 ± .05

Table A.5: Corrected charged particle spectra in the hadronic center of mass system as a function of the pseudorapidity  $\eta^*$  in the range  $123 < W < 162$  GeV for different  $Q^2$  intervals. The first error is the statistical, the second the systematic

$\eta^*$	$1/N dn_{ch}/d\eta^*$			
	$W > 162$ $10 < Q^2 < 15$	$W > 162$ $15 < Q^2 < 26$	$W > 162$ $26 < Q^2 < 110$	$W > 162$ $Q^2 > 110$
-5.50 - -5.25	0.01 ± .01 ± .00	0.05 ± .03 ± .01	0.16 ± .05 ± .02	0.09 ± .04 ± .01
-5.25 - -5.00	0.03 ± .01 ± .00	0.13 ± .04 ± .02	0.35 ± .09 ± .04	0.26 ± .08 ± .03
-5.00 - -4.75	0.15 ± .01 ± .02	0.24 ± .07 ± .03	0.30 ± .06 ± .04	0.39 ± .11 ± .05
-4.75 - -4.50	0.34 ± .08 ± .04	0.36 ± .07 ± .05	0.51 ± .09 ± .07	0.53 ± .11 ± .07
-4.50 - -4.25	0.62 ± .10 ± .08	0.45 ± .07 ± .06	0.86 ± .13 ± .11	0.92 ± .16 ± .12
-4.25 - -4.00	0.71 ± .10 ± .09	0.80 ± .11 ± .10	0.99 ± .13 ± .13	1.40 ± .21 ± .18
-4.00 - -3.75	1.05 ± .12 ± .14	1.06 ± .12 ± .14	1.24 ± .15 ± .16	1.24 ± .18 ± .16
-3.75 - -3.50	1.39 ± .14 ± .18	1.28 ± .14 ± .17	1.46 ± .17 ± .19	1.52 ± .21 ± .20
-3.50 - -3.25	2.09 ± .19 ± .27	1.80 ± .16 ± .23	1.80 ± .19 ± .23	2.09 ± .26 ± .27
-3.25 - -3.00	2.57 ± .21 ± .33	2.57 ± .22 ± .33	2.51 ± .23 ± .33	2.23 ± .26 ± .29
-3.00 - -2.75	2.51 ± .20 ± .33	2.25 ± .19 ± .29	2.42 ± .23 ± .31	2.19 ± .25 ± .28
-2.75 - -2.50	2.44 ± .21 ± .32	2.40 ± .21 ± .31	2.52 ± .24 ± .33	2.26 ± .27 ± .29
-2.50 - -2.25	2.58 ± .22 ± .33	2.20 ± .19 ± .29	2.47 ± .24 ± .32	2.50 ± .32 ± .32
-2.25 - -2.00	2.54 ± .21 ± .33	2.16 ± .20 ± .28	2.59 ± .24 ± .34	2.73 ± .34 ± .35
-2.00 - -1.75	2.27 ± .19 ± .29	2.41 ± .21 ± .31	2.61 ± .24 ± .34	2.56 ± .30 ± .33
-1.75 - -1.50	2.32 ± .19 ± .30	2.41 ± .21 ± .31	2.43 ± .23 ± .31	2.38 ± .29 ± .31
-1.50 - -1.25	2.18 ± .18 ± .28	2.17 ± .19 ± .28	2.21 ± .22 ± .29	2.90 ± .34 ± .38
-1.25 - -1.00	2.04 ± .18 ± .26	2.09 ± .18 ± .28	2.25 ± .22 ± .29	2.28 ± .27 ± .29
-1.00 - -0.75	2.14 ± .18 ± .28	2.49 ± .24 ± .32	2.47 ± .26 ± .32	2.95 ± .39 ± .38
-0.75 - -0.50	2.65 ± .30 ± .34	2.33 ± .28 ± .30	2.13 ± .28 ± .28	2.35 ± .35 ± .30
-0.50 - -0.25	2.40 ± .25 ± .31	2.13 ± .22 ± .28	2.17 ± .26 ± .28	2.45 ± .36 ± .32
-0.25 - 0.00	2.23 ± .20 ± .29	2.29 ± .23 ± .30	2.06 ± .22 ± .27	1.93 ± .27 ± .25
0.00 - 0.25	1.15 ± .12 ± .15	1.11 ± .13 ± .14	1.27 ± .15 ± .16	1.30 ± .20 ± .17
0.25 - 0.50	0.06 ± .03 ± .01	0.12 ± .05 ± .01	0.09 ± .04 ± .01	0.59 ± .15 ± .08

Table A.6: Corrected charged particle spectra in hadronic center of mass system as a function of the pseudorapidity  $\eta^*$  for  $W > 162$  GeV for different  $Q^2$  intervals. The first error is the statistical, the second the systematic

# Appendix B

## Generators

The version number and the non-default parameters of the Monte Carlo generators Lepto (PSWQ, MEPS, QPM) and Ariadne used in this study is listed below. Common to both Lepto and Ariadne is the structure function used (MRS H (DIS) [29]), the number of quark flavors in the sea (5) and the  $\Lambda_{QCD}$  (190 MeV).

- **PSWQ**

**Generator:** Lepto 6.1 + Jetset 7.3

**Parameter settings:** The default values were used except for the parameters listed below.

Parameter	Meaning	Default value	Value used
LST(8)	Simulation of QCD radiation	12	2
LST(9)	Scale of parton shower	5	3

- **QPM**

**Generator:** Lepto 6.1 + Jetset 7.3

**Parameter settings:** The default values were used except as listed below.

Parameter	Meaning	Default value	Value used
LST(8)	Simulation of QCD radiation	12	0

- **MEPS**

**Generator:** Lepto 6.1 + Jetset 7.3

**Parameter settings:** All parameters at there default values.

- **Ariadne**

**Generator:** Lepto 6.1 + Ariadne 4.04 + Jetset 7.3

**Parameter settings:** Default values according to the EMC/DELPHI tuning.



# Appendix C

## Formulae

In this section a more detailed derivation is presented of some of the equations discussed in section 2.1. In the following  $p$  denote four-vectors, i.e. the four-vector of particle  $a$  with an energy  $E_a$  and a momentum  $\bar{p}_a$  is  $p_a = (E_a, \bar{p}_a)$ . A four-vector of a particle multiplied by it self gives the mass of the particle according to;  $p_a^2 = (E_a, \bar{p}_a)^2 = E_a^2 - \bar{p}_a^2 = m_a^2$ . The notations are the same as in figure 2.1. The opening angle between two vectors is denoted by  $\alpha$ .

The momentum transfer square  $Q^2$  is defined as  $Q^2 \equiv -q^2 = -(p_e - p'_e)^2$ . Evaluating this gives

$$Q^2 \equiv -q^2 = -(p_e - p'_e)^2 = -(p_e^2 + p_e'^2 - 2p_e \cdot p'_e) = -p_e^2 - p_e'^2 + (2E_e E'_e - 2|\bar{p}_e||\bar{p}'_e| \cos \alpha) \quad (\text{C.1})$$

However, the angle to be used here is  $\theta_e$ , which is equal to  $180 - \alpha$ . Using this, recalling that  $\cos(180 - \theta_e) = -\cos \theta_e$  and rewriting  $p_e'^2$  as  $m_e^2$  gives

$$Q^2 = -m_e^2 - m_e'^2 + (2E_e E'_e + 2|\bar{p}_e||\bar{p}'_e| \cos \theta_e) \approx 2E_e E'_e (1 + \cos \theta_e) \quad (\text{C.2})$$

where in the last step the electron mass has been neglected. Recalling that  $(1 + \cos \theta_e) = 2\cos^2(\theta_e/2)$  yields finally

$$Q^2 \approx 4E_e E'_e \cos^2(\theta_e/2) \quad (\text{C.3})$$

The scaling variable  $y$  defined as  $y \equiv (p_p \cdot q)/(p_p \cdot p_e)$  may be rewritten as

$$y \equiv \frac{p_p \cdot q}{p_p \cdot p_e} = \frac{p_p \cdot (p_e - p'_e)}{E_p E_e - |\bar{p}_p||\bar{p}_e| \cos \alpha} = \frac{p_p \cdot p_e - p_p \cdot p'_e}{E_p E_e + |\bar{p}_p||\bar{p}_e|} \quad (\text{C.4})$$

where in the last step we have used the fact that the incoming electron and the incoming proton collide head on ( $\cos \alpha = -1$ ). Continuing by performing the dot products we get

$$y = \frac{E_p E_e + |\bar{p}_p||\bar{p}_e| - (E_p E'_e - |\bar{p}_p||\bar{p}'_e| \cos \alpha)}{E_p E_e + |\bar{p}_p||\bar{p}_e|} \quad (\text{C.5})$$

Neglecting the electron and proton mass gives

$$y \approx \frac{2E_p E_e - (E_p E'_e + E_p E'_e \cos \theta_e)}{2E_p E_e} = \frac{2E_p E_e - E_p E'_e (1 - \cos \theta_e)}{2E_p E_e} \quad (\text{C.6})$$

Replacing  $(1 - \cos \theta_e)$  with  $2 \sin^2(\theta_e/2)$  gives us finally

$$y \approx \frac{2E_p E_e - 2E_p E'_e \sin^2(\theta_e/2)}{2E_p E_e} = \frac{E_e - E'_e \sin^2(\theta_e/2)}{E_e} \quad (\text{C.7})$$

The scaling variable  $x$  is defined as  $x \equiv Q^2/(2p_p \cdot q)$ . Using the above we find that

$$x \equiv \frac{Q^2}{2p_p \cdot q} = \frac{Q^2}{2yp_p \cdot p_e} = \frac{Q^2}{2y(E_p E_e + |\vec{p}_p||\vec{p}_e|)} \quad (\text{C.8})$$

Neglecting the electron and proton masses gives

$$x \approx \frac{Q^2}{4yE_p E_e} \quad (\text{C.9})$$

Evaluating the expression for the total invariant mass squared in the hadronic system  $W^2$ , gives

$$W^2 \equiv (p_p + q)^2 = p_p^2 + q^2 + 2p_p \cdot q = m_p^2 - Q^2 + \frac{Q^2}{x} \quad (\text{C.10})$$

Neglecting the proton mass we finally obtain

$$W^2 \approx Q^2 \left( \frac{1-x}{x} \right) \quad (\text{C.11})$$

The total invariant mass squared  $s$  is defined as  $s \equiv (p_e + p_p)^2$ . Using the results above gives

$$s \equiv (p_e + p_p)^2 = p_e^2 + p_p^2 + 2p_e \cdot p_p = p_e^2 + p_p^2 + 2E_e E_p + 2|\vec{p}_e||\vec{p}_p| \quad (\text{C.12})$$

Neglecting the proton and electron masses yields

$$s \approx 4E_e E_p \quad (\text{C.13})$$

The product of the scaling variables  $x$  and  $y$  and the total invariant mass squared  $s$  is

$$xys = \frac{Q^2}{2p_p \cdot q} \cdot \frac{p_p \cdot q}{p_p \cdot p_e} \cdot [p_e^2 + p_p^2 + 2p_p \cdot p_e] \quad (\text{C.14})$$

which reduces to  $xys \approx Q^2$  if the proton and the electron masses are neglected.

# Appendix D

## Glossary

**The final data sample:** The sample of data events remaining after applying all event selection cuts described in section 5.3.

**Generated event:** Same as a Monte Carlo event.

**Generator level:** Just ordinary Monte Carlo events that has neither been simulated nor reconstructed.

**Monte Carlo event:** An event generated with a Monte Carlo program. Note that the event has not been detector simulated.

**Parton level:** Same as Generator level.

**Reconstructed Monte Carlo event:** A simulated event that has been reconstructed.

**Selected data event:** A data event that have passed the selection cuts described in section 5.3.

**Selected Monte Carlo event:** A reconstructed Monte Carlo event that have passed the section cuts described in section 5.3.

**Simulated event:** A Monte Carlo event that has been detector simulated.



# Appendix E

## The H1 collaboration

The H1 collaboration is an international group of about 300 physicists representing more than 10 countries. This is the list of the present members.

T. Ahmed<sup>3</sup>, S. Aid<sup>13</sup>, V. Andreev<sup>24</sup>, B. Andrieu<sup>28</sup>, R.-D. Appuhn<sup>11</sup>, M. Arpagaus<sup>36</sup>, A. Babaev<sup>26</sup>, J. Baehr<sup>35</sup>, J. Bán<sup>17</sup>, P. Baranov<sup>24</sup>, E. Barrelet<sup>29</sup>, W. Bartel<sup>11</sup>, M. Barth<sup>4</sup>, U. Bassler<sup>29</sup>, H.P. Beck<sup>37</sup>, H.-J. Behrend<sup>11</sup>, A. Belousov<sup>24</sup>, Ch. Berger<sup>1</sup>, H. Bergstein<sup>1</sup>, G. Bernardi<sup>29</sup>, R. Bernet<sup>36</sup>, G. Bertrand-Coremans<sup>4</sup>, M. Besançon<sup>9</sup>, R. Beyer<sup>11</sup>, P. Biddulph<sup>22</sup>, J.C. Bizot<sup>27</sup>, V. Blobel<sup>13</sup>, K. Borras<sup>8</sup>, F. Botterweck<sup>4</sup>, V. Boudry<sup>28</sup>, A. Braemer<sup>14</sup>, F. Brasse<sup>11</sup>, W. Braunschweig<sup>1</sup>, V. Brisson<sup>27</sup>, D. Bruncko<sup>17</sup>, C. Brune<sup>15</sup>, R. Buchholz<sup>11</sup>, L. Büngener<sup>13</sup>, J. Bürger<sup>11</sup>, F.W. Büsler<sup>13</sup>, A. Buniatian<sup>11,39</sup>, S. Burke<sup>18</sup>, G. Buschhorn<sup>26</sup>, A.J. Campbell<sup>11</sup>, T. Carli<sup>26</sup>, F. Charles<sup>11</sup>, D. Clarke<sup>5</sup>, A.B. Clegg<sup>18</sup>, B. Clerbaux<sup>4</sup>, M. Colombo<sup>8</sup>, J.G. Contreras<sup>8</sup>, C. Cormack<sup>19</sup>, J.A. Coughlan<sup>5</sup>, A. Courau<sup>27</sup>, Ch. Coutures<sup>9</sup>, G. Cozzika<sup>9</sup>, L. Criegee<sup>11</sup>, D.G. Cussans<sup>5</sup>, J. Cvach<sup>30</sup>, S. Dagoret<sup>29</sup>, J.B. Dainton<sup>19</sup>, M. Danilov<sup>23</sup>, W.D. Dau<sup>16</sup>, K. Daum<sup>34</sup>, M. David<sup>9</sup>, E. Deffur<sup>11</sup>, B. Delcourt<sup>27</sup>, L. Del Buono<sup>29</sup>, A. De Roeck<sup>11</sup>, E.A. De Wolf<sup>4</sup>, P. Di Nezza<sup>32</sup>, C. Dolfus<sup>37</sup>, J.D. Dowell<sup>3</sup>, H.B. Dreis<sup>2</sup>, V. Droutskoi<sup>23</sup>, J. Duboc<sup>29</sup>, D. Düllmann<sup>13</sup>, O. Dünker<sup>13</sup>, H. Duhm<sup>12</sup>, J. Ebert<sup>34</sup>, T.R. Ebert<sup>19</sup>, G. Eckerlin<sup>11</sup>, V. Efremenko<sup>23</sup>, S. Egli<sup>37</sup>, H. Ehrlichmann<sup>35</sup>, S. Eichenberger<sup>37</sup>, R. Eichler<sup>36</sup>, F. Eisele<sup>14</sup>, E. Eisenhandler<sup>20</sup>, R.J. Ellison<sup>22</sup>, E. Elsen<sup>11</sup>, M. Erdmann<sup>14</sup>, W. Erdmann<sup>36</sup>, E. Evrard<sup>4</sup>, L. Favart<sup>4</sup>, A. Fedotov<sup>23</sup>, D. Feecken<sup>13</sup>, R. Felst<sup>11</sup>, J. Feltse<sup>9</sup>, J. Ferencei<sup>15</sup>, F. Ferrarotto<sup>32</sup>, K. Flamm<sup>11</sup>, M. Fleischer<sup>11</sup>, M. Flieser<sup>26</sup>, G. Flügge<sup>2</sup>, A. Fomenko<sup>24</sup>, B. Fominykh<sup>23</sup>, M. Forbush<sup>7</sup>, J. Formánek<sup>31</sup>, J.M. Foster<sup>22</sup>, G. Franke<sup>11</sup>, E. Fretwurst<sup>12</sup>, E. Gabathuler<sup>19</sup>, K. Gabathuler<sup>33</sup>, K. Gamerding<sup>26</sup>, J. Garvey<sup>3</sup>, J. Gayler<sup>11</sup>, M. Gebauer<sup>8</sup>, A. Gellrich<sup>11</sup>, H. Genzel<sup>1</sup>, R. Gerhards<sup>11</sup>, U. Goerlach<sup>11</sup>, L. Goerlich<sup>6</sup>, N. Gogitidze<sup>24</sup>, M. Goldberg<sup>29</sup>, D. Goldner<sup>8</sup>, B. Gonzalez-Pineiro<sup>29</sup>, I. Gorelov<sup>23</sup>, P. Goritchev<sup>23</sup>, C. Grab<sup>36</sup>, H. Grässler<sup>2</sup>, R. Grässler<sup>2</sup>, T. Greenshaw<sup>19</sup>, G. Grindhammer<sup>26</sup>, A. Gruber<sup>26</sup>, C. Gruber<sup>16</sup>, J. Haack<sup>35</sup>, D. Haidt<sup>11</sup>, L. Hajduk<sup>6</sup>, O. Hamon<sup>29</sup>, M. Hampel<sup>1</sup>, E.M. Hanlon<sup>18</sup>, M. Hapke<sup>11</sup>, W.J. Haynes<sup>5</sup>, J. Heatherington<sup>20</sup>, G. Heinzelmann<sup>13</sup>, R.C.W. Henderson<sup>18</sup>, H. Henschel<sup>35</sup>, R. Herma<sup>1</sup>, I. Herynek<sup>30</sup>, M.F. Hess<sup>26</sup>, W. Hildesheim<sup>11</sup>, P. Hill<sup>5</sup>, K.H. Hiller<sup>35</sup>, C.D. Hilton<sup>22</sup>, J. Hladký<sup>30</sup>, K.C. Hoeger<sup>22</sup>, M. Höppner<sup>8</sup>, R. Horisberger<sup>33</sup>, V.L. Hudgson<sup>3</sup>, Ph. Huet<sup>4</sup>, M. Hütte<sup>8</sup>, H. Hufnagel<sup>14</sup>, M. Ibbotson<sup>22</sup>, H. Itterbeck<sup>1</sup>, M.-A. Jabiol<sup>9</sup>, A. Jacholkowska<sup>27</sup>, C. Jacobsson<sup>21</sup>, M. Jaffre<sup>27</sup>, J. Janoth<sup>15</sup>, T. Jansen<sup>11</sup>, L. Jönsson<sup>21</sup>, K. Johannsen<sup>13</sup>, D.P. Johnson<sup>4</sup>, L. Johnson<sup>18</sup>, H. Jung<sup>29</sup>, P.I.P. Kalmus<sup>20</sup>, D. Kant<sup>20</sup>, R. Kaschowitz<sup>2</sup>, P. Kasselmann<sup>12</sup>, U. Kathage<sup>16</sup>, J. Katzy<sup>14</sup>, H.H. Kaufmann<sup>35</sup>, S. Kazarian<sup>11</sup>, I.R. Kenyon<sup>3</sup>, S. Kermiche<sup>25</sup>, C. Keuker<sup>1</sup>, C. Kiesling<sup>26</sup>, M. Klein<sup>35</sup>, C. Kleinwort<sup>13</sup>, G. Knies<sup>11</sup>, W. Ko<sup>7</sup>, T. Köhler<sup>1</sup>,

J. Köhne<sup>26</sup>, H. Kolanoski<sup>8</sup>, F. Kole<sup>7</sup>, S.D. Kolya<sup>22</sup>, V. Korbel<sup>11</sup>, M. Korn<sup>8</sup>, P. Kostka<sup>35</sup>, S.K. Kotelnikov<sup>24</sup>, T. Krämerkämper<sup>8</sup>, M.W. Krasny<sup>6,29</sup>, H. Krehbiel<sup>11</sup>, D. Krücker<sup>2</sup>, U. Krüger<sup>11</sup>, U. Krüner-Marquis<sup>11</sup>, J.P. Kubenka<sup>26</sup>, H. Küster<sup>2</sup>, M. Kuhlen<sup>26</sup>, T. Kurča<sup>17</sup>, J. Kurzhöfer<sup>8</sup>, B. Kuznik<sup>34</sup>, D. Lacour<sup>29</sup>, F. Lamarche<sup>28</sup>, R. Lander<sup>7</sup>, M.P.J. Landon<sup>20</sup>, W. Lange<sup>35</sup>, P. Lanius<sup>26</sup>, J.-F. Laporte<sup>9</sup>, A. Lebedev<sup>24</sup>, C. Leverenz<sup>11</sup>, S. Levonian<sup>11,24</sup>, Ch. Ley<sup>2</sup>, A. Lindner<sup>8</sup>, G. Lindström<sup>12</sup>, F. Linsel<sup>11</sup>, J. Lipinski<sup>13</sup>, B. List<sup>11</sup>, P. Loch<sup>27</sup>, H. Lohmander<sup>21</sup>, G.C. Lopez<sup>20</sup>, V. Lubimov<sup>23</sup>, D. Lüke<sup>8,11</sup>, N. Magnussen<sup>34</sup>, E. Malinowski<sup>24</sup>, S. Mani<sup>7</sup>, R. Maraček<sup>17</sup>, P. Marage<sup>4</sup>, J. Marks<sup>25</sup>, R. Marshall<sup>22</sup>, J. Martens<sup>34</sup>, R. Martin<sup>11</sup>, H.-U. Martyn<sup>1</sup>, J. Martyniak<sup>6</sup>, S. Masson<sup>2</sup>, T. Mavroidis<sup>20</sup>, S.J. Maxfield<sup>19</sup>, S.J. McMahon<sup>19</sup>, A. Mehta<sup>22</sup>, K. Meier<sup>15</sup>, D. Mercer<sup>22</sup>, T. Merz<sup>11</sup>, C.A. Meyer<sup>37</sup>, H. Meyer<sup>34</sup>, J. Meyer<sup>11</sup>, S. Mikocki<sup>6</sup>, D. Milstead<sup>19</sup>, F. Moreau<sup>28</sup>, J.V. Morris<sup>5</sup>, G. Müller<sup>11</sup>, K. Müller<sup>37</sup>, P. Murín<sup>17</sup>, V. Nagovizin<sup>23</sup>, R. Nahnhauser<sup>35</sup>, B. Naroska<sup>13</sup>, Th. Naumann<sup>35</sup>, P.R. Newman<sup>3</sup>, D. Newton<sup>18</sup>, D. Neyret<sup>29</sup>, H.K. Nguyen<sup>29</sup>, T.C. Nicholls<sup>3</sup>, F. Niebergall<sup>13</sup>, C. Niebuhr<sup>11</sup>, R. Nisius<sup>1</sup>, G. Nowak<sup>6</sup>, G.W. Noyes<sup>5</sup>, M. Nyberg-Werther<sup>21</sup>, M. Oakden<sup>19</sup>, H. Oberlack<sup>26</sup>, U. Obrock<sup>8</sup>, J.E. Olsson<sup>11</sup>, E. Panaro<sup>12</sup>, A. Panitch<sup>4</sup>, C. Pascaud<sup>27</sup>, G.D. Patel<sup>19</sup>, E. Peppel<sup>35</sup>, E. Perez<sup>9</sup>, J.P. Phillips<sup>22</sup>, Ch. Pichler<sup>12</sup>, D. Pitzl<sup>36</sup>, G. Pope<sup>7</sup>, S. Prell<sup>11</sup>, R. Prosi<sup>11</sup>, G. Rädcl<sup>11</sup>, F. Raupach<sup>1</sup>, P. Reimer<sup>30</sup>, S. Reinshagen<sup>11</sup>, P. Ribarics<sup>26</sup>, H. Rick<sup>8</sup>, V. Riech<sup>12</sup>, J. Riedlberger<sup>36</sup>, S. Riess<sup>13</sup>, M. Rietz<sup>2</sup>, S.M. Robertson<sup>3</sup>, P. Robmann<sup>37</sup>, H.E. Roloff<sup>35</sup>, R. Roosen<sup>4</sup>, K. Rosenbauer<sup>1</sup>, A. Rostovtsev<sup>23</sup>, F. Rouse<sup>7</sup>, C. Royon<sup>9</sup>, K. Rüter<sup>26</sup>, S. Rusakov<sup>24</sup>, K. Rybicki<sup>6</sup>, R. Rylko<sup>20</sup>, N. Sahlmann<sup>2</sup>, E. Sanchez<sup>26</sup>, D.P.C. Sankey<sup>5</sup>, M. Savitsky<sup>23</sup>, P. Schacht<sup>26</sup>, S. Schiek<sup>11</sup>, P. Schleper<sup>14</sup>, W. von Schlippe<sup>20</sup>, C. Schmidt<sup>11</sup>, D. Schmidt<sup>34</sup>, G. Schmidt<sup>13</sup>, A. Schöning<sup>11</sup>, V. Schröder<sup>11</sup>, E. Schuhmann<sup>26</sup>, B. Schwab<sup>14</sup>, A. Schwind<sup>35</sup>, U. Seehausen<sup>13</sup>, F. Sefkow<sup>11</sup>, M. Seidel<sup>12</sup>, R. Sell<sup>11</sup>, A. Semenov<sup>23</sup>, V. Shekelyan<sup>23</sup>, I. Sheviakov<sup>24</sup>, H. Shooshtari<sup>26</sup>, L.N. Shtarkov<sup>24</sup>, G. Siegmon<sup>16</sup>, U. Siewert<sup>16</sup>, Y. Sirois<sup>28</sup>, I.O. Skillicorn<sup>10</sup>, P. Smirnov<sup>24</sup>, J.R. Smith<sup>7</sup>, Y. Soloviev<sup>24</sup>, J. Spiekermann<sup>8</sup>, H. Spitzer<sup>13</sup>, R. Starosta<sup>1</sup>, M. Steenbock<sup>13</sup>, P. Steffen<sup>11</sup>, R. Steinberg<sup>2</sup>, B. Stella<sup>32</sup>, K. Stephens<sup>22</sup>, J. Stier<sup>11</sup>, J. Stiewe<sup>15</sup>, U. Stösslein<sup>35</sup>, J. Strachota<sup>30</sup>, U. Straumann<sup>37</sup>, W. Struczinski<sup>2</sup>, J.P. Sutton<sup>3</sup>, S. Tapprogge<sup>15</sup>, R.E. Taylor<sup>38,27</sup>, V. Tchernyshov<sup>23</sup>, C. Thiebaut<sup>28</sup>, G. Thompson<sup>20</sup>, P. Truöl<sup>37</sup>, J. Turnau<sup>6</sup>, J. Tutas<sup>14</sup>, P. Uelkes<sup>2</sup>, A. Usik<sup>24</sup>, S. Valkár<sup>31</sup>, A. Valkárová<sup>31</sup>, C. Vallée<sup>25</sup>, P. Van Esch<sup>4</sup>, P. Van Mechelen<sup>4</sup>, A. Vartapetian<sup>11,39</sup>, Y. Vazdik<sup>24</sup>, M. Vecko<sup>30</sup>, P. Verrecchia<sup>9</sup>, G. Villet<sup>9</sup>, K. Wacker<sup>8</sup>, A. Wagener<sup>2</sup>, M. Wagener<sup>33</sup>, I.W. Walker<sup>18</sup>, A. Walther<sup>8</sup>, G. Weber<sup>13</sup>, M. Weber<sup>11</sup>, D. Wegener<sup>8</sup>, A. Wegner<sup>11</sup>, H.P. Wellisch<sup>26</sup>, L.R. West<sup>3</sup>, S. Willard<sup>7</sup>, M. Winde<sup>35</sup>, G.-G. Winter<sup>11</sup>, A.E. Wright<sup>22</sup>, E. Wunsch<sup>11</sup>, N. Wulff<sup>11</sup>, T.P. Yiou<sup>29</sup>, J. Žáček<sup>31</sup>, D. Zarbock<sup>12</sup>, Z. Zhang<sup>27</sup>, A. Zhokin<sup>23</sup>, M. Zimmer<sup>11</sup>, W. Zimmermann<sup>11</sup>, F. Zomer<sup>27</sup> and K. Zuber<sup>15</sup>,

<sup>1</sup> I. Physikalisches Institut der RWTH, Aachen, Germany<sup>a</sup>

<sup>2</sup> III. Physikalisches Institut der RWTH, Aachen, Germany<sup>a</sup>

<sup>3</sup> School of Physics and Space Research, University of Birmingham, Birmingham, UK<sup>b</sup>

<sup>4</sup> Inter-University Institute for High Energies ULB-VUB, Brussels; Universitaire Instelling Antwerpen, Wilrijk, Belgium<sup>c</sup>

<sup>5</sup> Rutherford Appleton Laboratory, Chilton, Didcot, UK<sup>b</sup>

<sup>6</sup> Institute for Nuclear Physics, Cracow, Poland<sup>d</sup>

<sup>7</sup> Physics Department and IIRPA, University of California, Davis, California, USA<sup>e</sup>

<sup>8</sup> Institut für Physik, Universität Dortmund, Dortmund, Germany<sup>a</sup>

- <sup>9</sup> CEA, DSM/DAPNIA, CE-Saclay, Gif-sur-Yvette, France
- <sup>10</sup> Department of Physics and Astronomy, University of Glasgow, Glasgow, UK<sup>b</sup>
- <sup>11</sup> DESY, Hamburg, Germany<sup>a</sup>
- <sup>12</sup> I. Institut für Experimentalphysik, Universität Hamburg, Hamburg, Germany<sup>a</sup>
- <sup>13</sup> II. Institut für Experimentalphysik, Universität Hamburg, Hamburg, Germany<sup>a</sup>
- <sup>14</sup> Physikalisches Institut, Universität Heidelberg, Heidelberg, Germany<sup>a</sup>
- <sup>15</sup> Institut für Hochenergiephysik, Universität Heidelberg, Heidelberg, Germany<sup>a</sup>
- <sup>16</sup> Institut für Reine und Angewandte Kernphysik, Universität Kiel, Kiel, Germany<sup>a</sup>
- <sup>17</sup> Institute of Experimental Physics, Slovak Academy of Sciences, Košice, Slovak Republic<sup>f</sup>
- <sup>18</sup> School of Physics and Materials, University of Lancaster, Lancaster, UK<sup>b</sup>
- <sup>19</sup> Department of Physics, University of Liverpool, Liverpool, UK<sup>b</sup>
- <sup>20</sup> Queen Mary and Westfield College, London, UK<sup>b</sup>
- <sup>21</sup> Physics Department, University of Lund, Lund, Sweden<sup>g</sup>
- <sup>22</sup> Physics Department, University of Manchester, Manchester, UK<sup>b</sup>
- <sup>23</sup> Institute for Theoretical and Experimental Physics, Moscow, Russia
- <sup>24</sup> Lebedev Physical Institute, Moscow, Russia<sup>f</sup>
- <sup>25</sup> CPPM, Université d'Aix-Marseille II, IN2P3-CNRS, Marseille, France
- <sup>26</sup> Max-Planck-Institut für Physik, München, Germany<sup>a</sup>
- <sup>27</sup> LAL, Université de Paris-Sud, IN2P3-CNRS, Orsay, France
- <sup>28</sup> LPNHE, Ecole Polytechnique, IN2P3-CNRS, Palaiseau, France
- <sup>29</sup> LPNHE, Universités Paris VI and VII, IN2P3-CNRS, Paris, France
- <sup>30</sup> Institute of Physics, Czech Academy of Sciences, Praha, Czech Republic<sup>f,h</sup>
- <sup>31</sup> Nuclear Center, Charles University, Praha, Czech Republic<sup>f,h</sup>
- <sup>32</sup> INFN Roma and Dipartimento di Fisica, Università "La Sapienza", Roma, Italy
- <sup>33</sup> Paul Scherrer Institut, Villigen, Switzerland
- <sup>34</sup> Fachbereich Physik, Bergische Universität Gesamthochschule Wuppertal, Wuppertal, Germany<sup>a</sup>
- <sup>35</sup> DESY, Institut für Hochenergiephysik, Zeuthen, Germany<sup>a</sup>
- <sup>36</sup> Institut für Teilchenphysik, ETH, Zürich, Switzerland<sup>i</sup>
- <sup>37</sup> Physik-Institut der Universität Zürich, Zürich, Switzerland<sup>i</sup>
- <sup>38</sup> Stanford Linear Accelerator Center, Stanford California, USA
- <sup>39</sup> Visitor from Yerevan Phys.Inst., Armenia

<sup>a</sup> Supported by the Bundesministerium für Forschung und Technologie, FRG under contract numbers 6AC17P, 6AC47P, 6DO57I, 6HH17P, 6HH27I, 6HD17I, 6HD27I, 6KI17P, 6MP17I, and 6WT87P

<sup>b</sup> Supported by the UK Particle Physics and Astronomy Research Council, and formerly by the UK Science and Engineering Research Council

<sup>c</sup> Supported by FNRS-NFWO, IISN-IKW

<sup>d</sup> Supported by the Polish State Committee for Scientific Research, grant No. 204209101

<sup>e</sup> Supported in part by USDOE grant DE F603 91ER40674

<sup>f</sup> Supported by the Deutsche Forschungsgemeinschaft

<sup>g</sup> Supported by the Swedish Natural Science Research Council

<sup>h</sup> Supported by GA ČR, grant no. 202/93/2423 and by GA AV ČR, grant no. 19095

<sup>i</sup> Supported by the Swiss National Science Foundation



# Appendix F

## The H1 Forward Muon Spectrometer



# Appendix G

## Selecting Forward Tracks in the H1-Detector